

DIFFUSE MOLECULAR GAS
IN CLOUD ENVELOPES AND THE GALAXY

by

DAVID L. COTTEN

(Under the direction of Loris Magnani)

ABSTRACT

Traditional measurements of molecular gas via rotational and hyperfine transitions of diatomic species such as CO, CH, and OH are only able to detect the cores and adjacent low-density molecular regions of interstellar molecular clouds. Longer than usual integration times of the CO($J = 1-0$) line at 115 GHz and the OH 1667 MHz ground state, hyperfine, main line transition have revealed the presence of low-density, diffuse gas surrounding the molecular core MBM40. Using the Schlegel, Finkbeiner and Davis (1998) dust maps in conjunction with new CO and OH observations, the amount of molecular gas in the diffuse outer regions of MBM40 has been determined to be equal if not greater than the mass in the core region. This much mass was not expected to be found in the outer most regions of the cloud. In addition, a re-analysis of high-latitude CO survey data reveals that this low-density molecular gas may be widespread in the Galaxy. The relationship between the low-density, diffuse molecular component studied in this thesis and the recently identified “dark” molecular gas is discussed.

INDEX WORDS: ISM: clouds, ISM: molecules, radio, MBM40, CO, OH, CH

DIFFUSE MOLECULAR GAS
IN CLOUD ENVELOPES AND THE GALAXY

by

DAVID L. COTTEN

B.S., Louisiana State University, 2005

A Dissertation Submitted to the Graduate Faculty
of The University of Georgia in Partial Fulfillment
of the
Requirements for the Degree

DOCTOR OF PHILOSOPHY

ATHENS, GEORGIA

2011

©2011

David L. Cotten

All Rights Reserved

DIFFUSE MOLECULAR GAS
IN CLOUD ENVELOPES AND THE GALAXY

by

DAVID L. COTTEN

Approved:

Major Professor: Loris Magnagni

Committee: Jean-Pierre Caillault
Inseok Song

Electronic Version Approved:

Maureen Grasso
Dean of the Graduate School
The University of Georgia
December 2011

**Diffuse Molecular Gas
in Cloud Envelopes and the Galaxy**

David L. Cotten

November 29, 2011

Acknowledgments

The National Radio Astronomy Observatory is a facility of the National Science Foundation operated under cooperative agreement by Associated Universities, Inc.. I would like to thank the Student Observing Support Program of NRAO for funding me for this research.

I would like to thank the members of my committee: Loris Magnani, J. P. Callault, and Inseok Song, for their input into my final dissertation.

I would especially like to thank Loris Magnani, without his help I would have never finished this dissertation, nor completed my degree.

I would like to thank Adam Schneider for helping me throughout the years. He was always willing to listen to my questions, and to discuss all the different problems that arose during my research.

I would like to thank Tara Hufford for giving me the drive to work hard everyday and for being such a positive influence in my life. Especially during the final weeks of my dissertation, she was there to help me when the stress was the greatest.

And I would like to thank my parents for believing in me through all of my life decisions, without you I would not be where I am today.

Contents

Acknowledgements	i
List of Figures	iv
List of Tables	vi
1 Introduction to the Gas Content of the Galaxy	1
1.1 The Interstellar Medium	1
1.2 Radiative Transfer Basics	8
1.3 Dynamics of the Cold ISM	10
1.4 The Transition from Atomic to Molecular Gas	13
1.5 The Possible Existence of “Dark” Molecular Gas	15
1.6 Outline for Thesis	17
2 Translucent Clouds and Their Molecules	19
2.1 Cloud Classification	19
2.2 Observing Translucent Clouds	22
2.3 Molecular Hydrogen	24
2.4 CO as a Tracer of Diffuse Molecular Gas	27
2.5 OH as a Tracer of Diffuse Molecular Gas	28

3	The E(B-V) Threshold: An Estimate of the Molecular Mass at High Galactic Latitudes	31
3.1	Introduction	31
3.2	CO vs. E(B-V) at High Latitudes	32
3.3	Discussion	45
3.4	Conclusion	48
4	A Brief Review of the X-Factor Calibration	49
4.1	Introduction	49
4.2	Techniques for Calibrating X_{CO}	51
4.3	Extinction Method	52
4.4	Virial Theorem Method	53
4.5	Far Infrared Method	54
4.6	Gamma Ray Method	55
4.7	CH Method	56
4.8	Conclusion	57
5	The X-Factor in MBM 40 at High Angular Resolution	58
5.1	Introduction	58
5.2	Astrochemistry of CO	59
5.3	Observations	61
5.4	Results	66
5.5	X_{CO} in MBM40	68
5.6	Conclusion	74
6	The Outer Envelope of MBM 40; CO Data	75
6.1	Introduction	75

6.2	Past Studies	76
6.3	Comparison of Our CO Observations with those of Chastain (2005)	78
6.4	Analysis and Conclusion	88
7	Hydroxyl in MBM 40	90
7.1	Introduction	90
7.2	Astrochemistry of Hydroxyl	91
7.3	Observations	94
7.4	Results	95
7.5	Analysis	108
7.6	Conclusion	109
8	Summary and Future Work	110
	Bibliography	114

List of Figures

1.1	Star-gas cycle	2
1.2	Color composite image from the Sloan Digital Sky Survey-II	5
1.3	A comparison of nomenclature from past molecular studies and this thesis	16
2.1	Ground state hydroxyl, and hyperfine splitting	30
3.1	Histogram of E(B-V) values up to 0.20	34
3.2	Histogram of E(B-V) values up to 1.20	37
3.3	Histogram of E(B-V) values from 0.20 to 1.20	38
3.4	Histogram of E(B-V) values from 0.20 to 1.20 with the y-axis magnified	39
3.5	Histogram of non CO detections to detections versus E(B-V)	41
3.6	Ratio of CO detections to observations versus E(B-V) in 0.05 bins	42
3.7	Ratio of CO detections to observations versus E(B-V) in 0.01 bins	43
5.1	Positions of the CO(1-0) observations of MBM40	62
5.2	Positions of the eight 5-point crosses in the envelope of MBM40	67
5.3	W(CO) versus E(B-V) for the eight 5-point crosses in the envelope of MBM40	69
5.4	X _{CO} versus W(CO) for the envelope and the core of MBM40	73
6.1	W(CO) contours obtained by Chastain (2005) for MBM40	77
6.2	Positions of CO(1-0) observations for MBM40	79

6.3	W(CO) versus E(B-V) for MBM40	87
7.1	The positions of OH observations in MBM40	97
7.2	W(OH) versus E(B-V) for MBM40	105

List of Tables

2.1	Different types of small molecular clouds based on visual extinction	20
2.2	Hydroxyl transitions of the lowest rotational state	29
3.1	Total molecular mass in the northern Galactic hemisphere	35
3.2	Total molecular mass in the southern Galactic hemisphere	36
3.3	Estimate for the lower limit of molecular hydrogen in the high latitudes . . .	47
4.1	X_{CO} calibration methods and typical values	52
5.1	Coordinates for the observed CO positions in MBM40.	63
5.2	Averaged values of $W(\text{CO})$ and $E(\text{B-V})$ for the eight 5-point crosses in the envelope of MBM40.	68
5.3	Determination of X_{CO} from CH in MBM40.	70
6.1	$N(\text{CO})$ for the observed CO positions in MBM40	81
6.2	Mass of CO in 89 of the observed 103 lines of sight in MBM40	85
6.3	Total mass of CO from $W(\text{CO})$ extrapolated over the entire cloud	85
6.4	$N(\text{H}_2)$ and total mass of H_2 in MBM40 from $W(\text{CO})$	86
6.5	Average $E(\text{B-V})$ values for MBM40 and $W(\text{CO})$ calculated from $E(\text{B-V})$. .	86
6.6	Total mass of CO calculated for MBM40 from $W(\text{CO})$ versus $E(\text{B-V})$	87
6.7	$N(\text{H}_2)$ and total mass of H_2 from the relationship of $E(\text{B-V})$ and $W(\text{CO})$. .	88

7.1	Coordinates and observed OH values in MBM40.	99
7.2	Coordinates and column densities for observed OH positions in MBM40 . . .	101
7.3	Mass of OH in 32 of the observed 51 lines of sight toward MBM40	103
7.4	Total mass of OH extrapolated over the entire MBM40 cloud	103
7.5	Total mass of H ₂ in MBM40 determined by OH 1667 MHz emission	104
7.6	Average E(B-V) values for MBM40 and W(OH) calculated from E(B-V) . . .	105
7.7	Average N(OH) values for MBM40 determined from W(OH)	106
7.8	Total M(OH) for MBM40	106
7.9	Total M(H ₂) (M _⊙) for MBM40 from W(OH)	106
7.10	Average E(B-V), N(HI + H ₂), total HI mass, and H ₂ mass	108
8.1	Total calculated molecular hydrogen mass in MBM40 for all five techniques .	113

Chapter 1

Introduction to the Gas Content of the Galaxy

1.1 The Interstellar Medium

The most abundant and important molecule in our Galaxy, the Milky Way, is molecular hydrogen, H_2 . To learn about the interstellar medium in our Galactic neighborhood and, by extension, in the Galaxy and other galaxies, we need to understand how molecular gas forms, how it interacts with its surroundings, and how it is destroyed. Stars form from molecular gas concentrations, whimsically called clouds, so to understand the life cycle of stars, one must thoroughly understand the gas content of the Galaxy. Galaxies, like the Milky Way, are bound by their own gravity causing their components to strongly interact. This large scale interaction between components is difficult to model, so one strategy is to assume the Galaxy is a system consisting of isolated sub-systems such as stars, star clusters, interstellar gas clouds, etc. By modeling these sub-systems individually we can get an accurate picture of how our Galaxy functions (Lequeux 2005). In our Galaxy, 10% of the baryonic matter

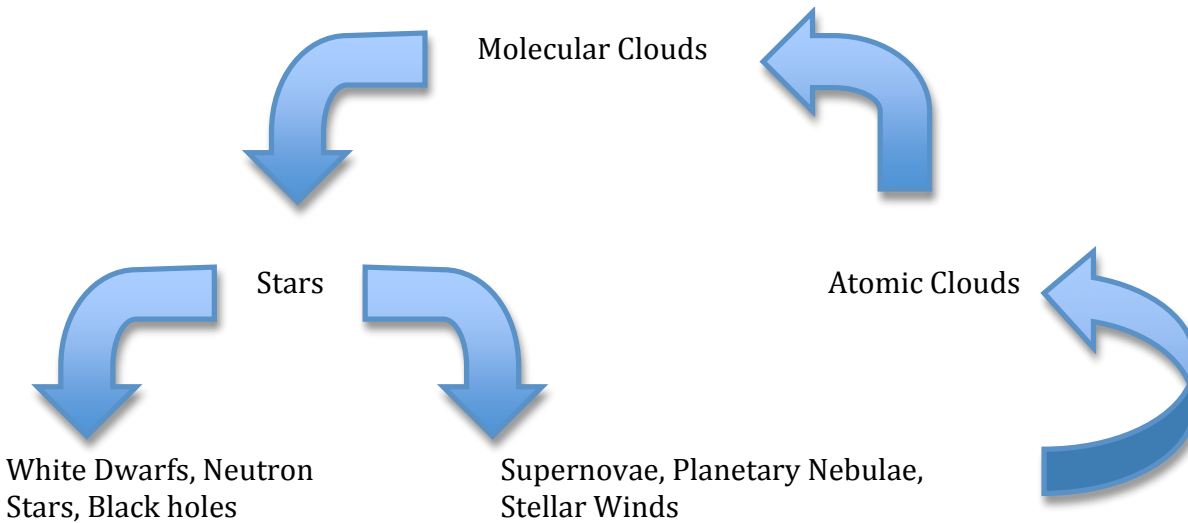


Figure 1.1: The star-gas cycle, where supernovae, planetary nebulae and stellar winds recycle gas from the later stages of a star’s lifetime into the hot ISM. A portion of that gas cools and forms atomic gas. From a portion of that atomic gas, molecular clouds form. Dense regions within molecular clouds give rise to stars and the cycle continues.

is found in the ISM with most of the dust and gas being confined to the disk¹. Within the disk most of the molecules are incorporated into molecular complexes which are large, up to 200 pc in size, and consist of groups of large molecular clouds that are gravitationally bound together. The thickness of the Galactic disk is about 500 pc and 90% of the molecular gas is contained within this disk (Shull and Beckwith 1982).

In our Galaxy the total gas mass consisting of molecular hydrogen, H_2 , is surpassed only by the mass in atomic hydrogen,² thus making the study of molecular hydrogen a vital subject for study. The gas within our Galaxy is cycled through different forms during the lifetime of the Galaxy, in a process called the star-gas cycle (see Figure 1.1). The star-gas cycle describes how a portion of the gas that makes up the interstellar medium (hereafter

¹In this thesis we will not discuss the non-baryonic component of the Galaxy, often referred to as “dark matter”.

²In astronomical terminology, atomic hydrogen is also known as HI.

the ISM) can cool from a mainly atomic state to form cold molecular clouds, and it is from clumps in these cold molecular clouds that protostars form. The protostars become stars once nuclear fusion begins at their cores and this fusion starts the process of creating heavier elements up to iron in atomic number. These elements can be recycled back into the galaxy throughout the star's lifetime (stellar winds) and also at a star's death (supernova explosions for high-mass stars, planetary nebulae for low-mass stars), which can create even heavier elements to add to the cycle (Bennett et al. 2010). The gas that is expelled through stellar life and, also, death forms a hot ISM because the high-speed gas ejected into space by stellar winds or supernovae sweep up surrounding interstellar material creating a bubble of hot (10^6 K), ionized gas. This hot bubble of ionized gas over time will cool, allowing ions to recombine with electrons, forming atoms, and, thus, the atomic ISM. Once a portion of the atomic ISM is compressed and cools further, some of the atoms can combine to form molecules, i.e., the molecular ISM, hence completing the cycle (see Figure 1.1). Throughout the Galaxy you can find gas in every stage of this cycle, and studying the various forms taken by the gas increases knowledge about the star-gas cycle, and therefore the evolution of the Galaxy. In this thesis we focus primarily on the molecular portion of the ISM.

Besides gas, the ISM consists of other components, such as dust and cosmic rays, just to name a few. The interstellar dust mixed with the gas consists of small solid particles, typically less than $1 \mu\text{m}$ in size, which play a large role in the formation of H_2 , as will be discussed later in this chapter. The majority of the stellar radiation field is absorbed by dust grains and reemitted in the infrared; for instance most of the $60 \mu\text{m}$ and $100 \mu\text{m}$ flux observed with the Infrared Astronomy Satellite (IRAS) is from interstellar dust (Jura 1987). Other particles that contribute to the shaping of the ISM through dissociation of molecules and ionization of atoms, are cosmic rays. Cosmic rays are high energy particles, ions and electrons, with extremely relativistic kinetic energies. Cosmic rays possessing energies as high as 10^{21} eV have been detected (Draine 2011). Although cosmic rays interact with

hydrogen nucleons to produce a distributed gamma-ray background (Bloemen 1991), in this thesis we focus mainly on the gas and dust phase of the ISM, and we will discuss these two components in more detail below.

1.1.1 Gas in the Galaxy

Interstellar gas is defined as a mixture of ions, atoms, and molecules in the gas phase, which, for the most part, have thermal velocity distributions, i.e., their velocity distribution is dependent on their temperature. The gas may be in a variety of phases depending on local heating, cooling, ionization, and in some cases its past history - for instance, the gas may contain more heavy elements if it came from a supernova remnant (Myers 1987). Molecular gas is kept in thermal balance by competing processes of heating and cooling. In dense clouds where $n > 10^3 \text{ cm}^{-3}$ (n is known as the number density of particles) most of the heating involves interactions of the gas with cosmic rays and collisions between gas particles. In lower density regions, the heating is primarily driven by photodissociation as starlight causes electrons to be ejected from small grains mixed with the gas. The electrons collide with the ambient hydrogen nucleons and, in this manner, share their kinetic energy, therefore raising the gas temperature. The cooling is done primarily by molecular line emission of CO, because it is the dominant cooling mechanism in this regime (Goldsmith 1987). The consequences of these processes will be discussed in more detail in Section 1.4.2.

Within the ISM the gas outnumbered the dust by roughly a factor of 100 in terms of mass, and its number density can vary from 10^{-3} cm^{-3} to 10^7 cm^{-3} with temperatures ranging from 10 K to 10^7 K. The coldest phase of the ISM is molecular, and most molecular clouds have temperatures between 10 and 20 K if they are not associated with high luminosity heating sources (such as early-type stars). These low temperature clouds include the classical dark clouds (see Figure 1.2), some of which show no evidence of star formation, but the majority of which are associated with low-mass star formation (Goldsmith 1987).

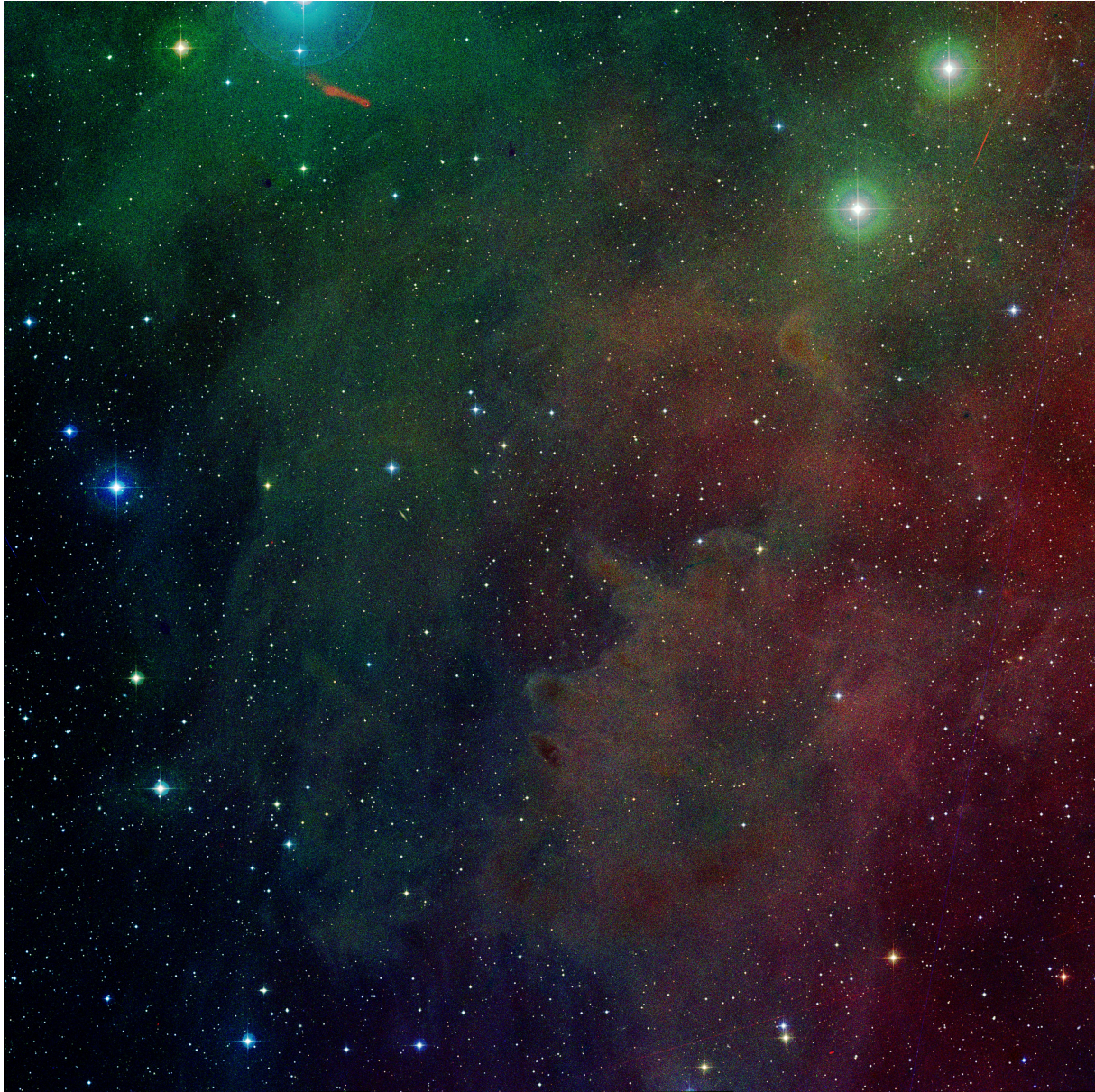


Figure 1.2: Color composite image from the Sloan Digital Sky Survey-II (g, r, i, z bands) of the high-latitude dark molecular cloud, MBM 12. The dark, obscuring clumps are evident, as is a general decrease in the stellar density in the direction of the cloud. Image credit: Adam Schneider, University of Georgia

Collisions are very important in the ISM and, within clouds, they can produce excitations, recombinations, and a range of energy distributions. The kinetic energy, and therefore the kinetic temperature, of the gas depends on the rates at which particles elastically collide with each other. Collisional time scales are short enough to ensure that the velocity for the particles maintains a Maxwellian distribution, thus allowing a measure of the kinetic temperature to be a measure of the actual temperature of the particles.

Knowing about the velocity of material throughout a molecular cloud is useful because these velocity fields can tell us how the gas is moving within the cloud and how it is moving relative to other gas particles. However, understanding the velocity field is highly problematic because thermal motions are not the dominant form of mass motion in molecular clouds. Some clouds have rotation but this rarely contributes systematic velocity gradients comparable to the characteristic line widths of the observed transitions and therefore cannot be the source of the line broadening. The velocity dispersion of the spectral lines from widespread molecular species such as CO, CH, OH, and H₂CO are supersonic compared to the thermal line width at the kinetic temperature of the gas. This implies that turbulent motion is present in the gas and probably provides one of the most important pressure support mechanisms against cloud collapse. However, the origin and maintenance of the turbulent flows in molecular clouds is the subject of much study and debate (Shore 2007).

Observations indicate that most clouds are in virial equilibrium and have lifetimes of 10^7 years (Goldsmith 1987). However, a subset of clouds located at high Galactic latitudes show very turbulent velocity fields and a, ragged, filamentary morphology. Their velocity dispersion is greater by an order of magnitude than that expected for a cloud of their size and mass and it is likely they are breaking up on the sound crossing time scale (10^6 years) (Magnani et al. 1985). We will discuss these clouds in greater detail in Chapter 2.

1.1.2 Dust in the Galaxy

Since the turn of the 20th century, light traveling through the Galaxy has been known to appear dimmer than expected as a function of the object’s distance alone. This phenomenon, known as interstellar extinction, is primarily caused by intervening dust, which “reddens” the light of observed objects. Higher frequency light is absorbed or scattered by dust more than lower frequency light causing the light from the object to appear more prominent in the red portion of the spectra than would be the case if there was no dust. Although this interstellar “reddening” has been known about for almost a hundred years there are still many qualities about interstellar dust that remain uncertain to this day including its chemical composition and exact size distribution. The same dust that scatters and/or absorbs light is also one of the main catalysts in the formation of molecular hydrogen, as will be discussed later in this chapter. The size of dust grains ranges from as small as 0.01 μm , based on long infrared emission observations, to as large as 0.2 μm or larger (Draine 2011).

The most direct way to study dust is by observing stars and/or other standard luminosity objects such as white dwarfs and supernovae. By comparing the spectra of the objects located behind the dust in question with spectra from stars or other standard objects much can be learned about the dust. Visually, the presence of dust is characterized by its extinction, A_λ , where λ signifies a wavelength dependence. The relationship between A_λ and the flux from a given object is quantified as

$$A_\lambda = 2.5 \log_{10} [F_\lambda^0/F_\lambda] \text{ (mag)} \quad (1.1)$$

where F_λ^0 is the flux that would have been observed without any dust along the line of sight, and F_λ is the observed flux. The difference between the extinction in the blue band, A_B (centered on 440.5 nm), and the extinction in the visible band, A_V (centered on 547 nm), is known as the color index, (B-V), where the quantities are measured in magnitudes.

The color excess, $E(B-V)$ is the difference in the obscured, $(B - V)$, color index from the unobscured, $(B - V)_o$, color index:

$$E(B - V) = (B - V) - (B - V)_o. \quad (1.2)$$

Extinction is dependent on the wavelength of light and at visible wavelengths a ratio has been empirically established to relate how the extinction varies with wavelength:

$$R_V = \frac{A_V}{E(B - V)} \quad (1.3)$$

where R_V has an average value ≈ 3.1 (Spitzer 1978). A_V and $E(B-V)$ can be used with simplifying assumptions, to obtain the column density of dust for a given line of sight, and, when coupled with observations of the gas content, to determine gas-to-dust ratios for various regions of the ISM. Other filter bands can be used to map ISM regions but the R_λ value differs for other filter bands.

1.2 Radiative Transfer Basics

The study of the ISM is done through modeling and observations, which are made primarily by studying the electromagnetic radiation that arrives at our telescopes. Since molecular clouds are cold, most of our observations are going to be made in the radio and infrared portion of the electromagnetic spectrum. To understand what is arriving at our telescopes we need to understand how that radiation is created and also how it interacts with matter in between the source and our instruments. Radiative transfer describes how electromagnetic radiation propagates and interacts through media; it describes both the emission and absorption of light produced by the media along the line of sight. Specific intensity, I_ν , is the electromagnetic power per unit area, per frequency interval $d\nu$, per steradian, and this

value is equal to the intensity of a blackbody, B_ν , if the material in question is in local thermodynamic equilibrium:

$$I_\nu = B_\nu = \frac{2h\nu^3}{c^2} \cdot \left(\exp\left(\frac{h\nu}{kT_{ex}}\right) - 1\right)^{-1} \quad (1.4)$$

here T_{ex} is the excitation temperature of the atom/molecule whose transition we are observing. T_{ex} is used to describe the difference in population for the two levels, n_u for upper, and n_l for lower, involved in the various transitions.

The definition of T_{ex} is given by:

$$T_{ex,ul} = \frac{E_{ul}}{k \cdot \ln\left[\frac{(n_l/g_l)}{(n_u/g_u)}\right]} \quad (1.5)$$

where E_{ul} is the difference in energy between the upper level and the lower level, and g refers to the degeneracy of the respective levels. The intensity of a radiating source is known as the brightness temperature of a gas, and in LTE:

$$T_B(\nu) = \frac{h\nu}{k \cdot \ln\left[1 + I_\nu \cdot \frac{2h\nu^3}{c^2}\right]} \quad (1.6)$$

is equal to the actual temperature of the emitting and absorbing gas. But in radio astronomy our observations are within the Rayleigh-Jeans limit, where $h\nu \ll kT_{ex}$. In the Rayleigh-Jeans limit Equation 1.4 can be written as:

$$I_\nu = \frac{2kT_B\nu^2}{c^2} \quad (1.7)$$

where, in this limit, I_ν is proportional to T_B .

One of the most useful measurements in observational radio astronomy is the antenna temperature, $T_A(\nu)$. The antenna temperature is related to the brightness temperature, the

physically relevant quantity, by a factor that measures primarily the quality of the reflecting surface of the telescope.

$$T_A(\nu) = T_B \cdot \eta_B \quad (1.8)$$

where η_B is a factor that ranges from $0 \rightarrow 1$ and is dependent on the telescope. Since the radiation from a source passes through a medium, attenuation and re-emission of the signal occurs.

The equation for how the intensity changes as it propagates through a medium can be rewritten as

$$T_A = T_A(0)e^{-\tau_\nu} + (T_{\text{ex}})(1 - e^{-\tau_\nu}) \quad (1.9)$$

where τ is the optical depth of the attenuating medium and $\frac{h\nu}{kT_{\text{ex}}}$ is $\ll 1$, which applies for the clouds that we observe in this work. Equation 1.9 describes the actual measurement that we receive at our detectors (Draine 2011). The column density of an atom/molecule can be calculated by integrating the optical depth over frequency. In cases where $\tau_\nu \ll 1$, Equation 1.9 goes to the background temperature, $T_A(0)$. The other extreme is where $\tau_\nu \gg 1$, in this case Equation 1.9 approaches the excitation temperature of the gas.

1.3 Dynamics of the Cold ISM

Interstellar gas pressures can vary by two orders of magnitude or more. These variations are a direct result of shock waves from supernovae explosions, large scale galactic flows (density waves), self gravitating clouds, and stellar winds or HII regions from an OB star (Myers 1987; Elmegreen 1987). The largest molecular clouds, the giant molecular clouds, are self gravitating with internal pressure an order of magnitude greater than other phases of the ISM (Jura 1987). Using the virial theorem to assess the equilibrium status of clouds, we can divide the clouds into gravitationally bound or unbound structures (however, see Section 1.4.1 for a

more detailed analysis). Gravitationally unbound clouds exist where $M \ll R\sigma^2G^{-1}$ where R is the cloud radius, σ is the velocity dispersion and G is the gravitational constant. Bound clouds exist where the previous relationship is near equal, i.e., $M \approx R\sigma^2G^{-1}$ (Myers 1987). Translucent clouds³ lack the mass of dark or giant molecular clouds and this insufficient binding mass, as deduced from cloud size and velocity dispersion of the cloud, may imply that a typical translucent cloud is breaking up on the sound-crossing timescale $\approx 10^6$ yr (Magnani et al. 1985).

The gas in our Galaxy has an energy density around 1 eV cm^{-3} , which is close to the energy density of other constituents within our Galaxy, probably from equipartition of energy considerations. In our Solar neighborhood the energy density of star light is in the realm of 1 eV cm^{-3} , with measurements between 0.2 and 1.4 eV cm^{-3} (Mathis et al. 1983). Mathis, Metzger, and Panagia (1983) found that between 912 \AA and $8 \mu\text{m}$, the energy density of star light had an average value of 0.5 eV cm^{-3} , where the lower limit of 912 \AA was chosen because here neutral hydrogen becomes optically thick, and the lower limit for effective contribution from the photospheres of stars led to the upper limit of $8 \mu\text{m}$. This is where the blackbody emission from even hot stars begins to drop to lower levels than the thermal dust emission from the ISM. The energy density of cosmic rays, based on cosmic ray fluxes from Earth and the indirect method of observing ionized molecules (many caused by cosmic ray interactions), has a value near 1.4 eV cm^{-3} (Jura 1987). Based on the characteristic magnetic field strength in the ISM of 2.5×10^{-6} gauss (Heiles 1976), $B^2/8\pi$ can be used to find a value of 0.9 eV cm^{-3} for the average energy density of the magnetic field. It is not strictly coincidence that all of these energy density values are very similar since gas in our Galaxy can be moved by magnetic fields and influenced by cosmic rays and stellar radiation fields (Draine 2011).

The ISM appears to be have a quasi-equipartition of energy densities and also appears

³Translucent clouds are fairly small objects, $\sim 1 \text{ pc}$, with $1 < A_V < 5 \text{ mag}$, and will be discussed extensively in Chapter 2.

to be locally chemically homogeneous. According to Knapp and Morris (1985) the regions that act as sinks of matter for the ISM are mainly star-forming regions. They are contained in the disk of the Milky Way which has a diameter of 30 kpc and has a total star formation rate of $\approx 9 M_{\odot} \text{ yr}^{-1}$ (Draine 2011). Sources for the ISM come from the mass loss of stars and infall of extra-galactic material, with red giants being the most important stars for mass being transferred back into the ISM. Since Salpeter (1976) found that red giants turn into white dwarfs at the rate of about 1 per year in our Galaxy, it can be hypothesized that about $1 M_{\odot} \text{ yr}^{-1}$ worth of mass is added to the ISM (Draine 2011).

The injection of energy into the ISM via supernova explosions and stellar winds allow the components of the ISM to be well-mixed. Observations of the ratio of $^{12}\text{C}/^{13}\text{C}$ does not vary by more than a factor of 2 within the solar galacto-centric radius of our Galaxy⁴, and the isotope ratio of weak CH^+ absorption lines, $^{12}\text{CH}^+ / ^{13}\text{CH}^+$, obtained by Hawkins and Jura (1987), does not deviate significantly from a value of $43 \pm$. These two independent observations help confirm that the ISM as a whole can be considered homogeneous (Jura 1987). Although the ISM as a whole is homogenous as far as elemental composition, inside of clouds, or within cloud complexes, there is great clumpiness and density inhomogeneity. The inhomogeneous nature of molecular clouds has been known since Kutner et al. (1977) observed the Orion Molecular Cloud Complex (OMCC) with the lowest rotational transition of CO, $^{12}\text{CO} \text{ J} = (1 - 0)$ at 115 GHz, using the GISS 1.2 m radio telescope with the equivalent of 1 pc resolution, compared to the size of the entire OMCC of ~ 30 pc. It is evident by the map seen in Figure 1(c) from Kutner et al. (1977) that this particular complex is very inhomogeneous, containing clumps of gas alongside of regions where there are very few detections (Goldsmith 1987). The structuring agents for clouds include gravitation, large-scale gas flows, and mechanical energy input via supernovae or stellar winds.

⁴The solar galactic centric radius is ≈ 8 kpc where $1 \text{ pc} = 3.1 \times 10^{18} \text{ cm}$.

1.4 The Transition from Atomic to Molecular Gas

The formation of molecular clouds results from the compression of atomic clouds by the mechanisms described in the previous section. This compression leads to the alteration of the interstellar radiation field by self-shielding (described below) and increased dust density. Once molecules form in quantity, their efficient cooling of the region leads to further compression and a molecular structure forms. Once the clouds have formed, there are regions where molecular clouds are strongly reacting with the interstellar radiation field and are being destroyed. Both the formation and destruction of molecular clouds are discussed below.

1.4.1 Gravitational State

Molecular clouds can be categorized by their gravitational state as self-gravitating, diffuse, or unbound. Self-gravitating clouds are held together by gravity as a result of having sufficient mass. Diffuse clouds are bound not by gravity, due to their insufficient mass, but rather by external pressures. The last group is unbound clouds where external pressures and gravity are unable to keep them bound (Elmegreen 1993b). These clouds are actively dispersing on time scales relative to the sound-crossing time across the cloud.

Using a dimensionless parameter, $\frac{P}{G\sigma_m^2}$, introduced by Elmegreen (1993a), the classification of clouds can be categorized in a more quantitative way. In this parameter, P represents pressure, G is the gravitational constant, and σ_m is the mass column density (i.e., the mass per unit area). If $\frac{P}{G\sigma_m^2} \gg 1$ then gravity is not a dominant factor in the dynamics of the cloud, and if $\frac{P}{G\sigma_m^2} \ll 1$ then the cloud is considered self-gravitating (Elmegreen 1993a).

Clouds in the ISM can be divided even further into two subgroups depending on their atomic and molecular abundances. Molecular hydrogen needs dust grains to form (this is discussed in detail in Section 2.3.1) but they also must be shielded from the ultraviolet

radiation field thus, the amount of H_2 is dependent on its formation rate and its shielding from the ISRF. A cloud with a large formation rate compared to the destruction rate resulting from the radiation field yields a mostly molecular cloud, while if the opposite is true, the result is a mostly atomic cloud.

1.4.2 The Photodissociation Region

The radiation field impinging on a cloud in the ISM is extremely important in the structure of the cloud. Photodissociation of molecules by the radiation field causes a transition zone to exist on the outer surface of the molecular cloud, and outside of this region, even further from the center of the molecular cloud, a region of mostly atomic particles exists. The interface between a molecular cloud and an ionization region is called a photodissociation region, or PDR (Draine 2011). The depth of the PDR region depends on the interstellar radiation field (ISRF) and inversely on the density of molecules.

Near the center of the cloud, further away from sources of the ISRF, the gas is mainly molecular with complex molecules located in the denser clumps. Molecular species such as CS and NH_3 are excellent tracers for this dense gas, but the CO rotational transitions can also suffice. Surrounding these dense clumps is an area that is somewhat more bathed in UV radiation. Within this region the main heating source is photodissociation, which was described above, and the primary cooling mechanism is the loss of energy from the CO rotational line radiation. This is the region that CO surveys, such as the Galactic plane survey by Dame, Hartmann, and Thaddeus (2001), primarily detect. Some past studies have referred to this region as a “molecular envelope” surrounding the denser core or clump regions traced by CS or NH_3 . It is very important to realize that in this thesis we will not refer to this region as an envelope region; instead, we will refer to it as the translucent molecular core. The adjacent outer regions to the core will be referred to as the “envelope” and “outermost” regions.

The outer portion of the PDR, sometimes called the “diffuse molecular” region is primarily cooled by CII⁵, but, CO is also present here and with sufficiently long integration times, detections of molecular gas by CO(1-0) can be made here. This conclusion is one of the main points of this thesis: if CO(1-0) observations can be made in “diffuse molecular” regions, then estimates of the H₂ content in this difficult to probe region can be made. Previously, observations of these regions have been made using CII emission at 157.7 μm by Ingalls, Reach, and Bania (2002), but in this wavelength range observations must be made by space based observatories. In this thesis we will refer to the inner portion of these diffuse molecular regions as the “envelope” and the outer portion as the “outermost” regions of translucent clouds. It is in the “outermost” region by our definition where the molecular cloud edge is and the transition to the surrounding ISM occurs. Figure 1.3 shows a schematic diagram of the structure of a PDR as a function of depth in the cloud. In later chapters we will describe these regions in terms of the dust column density in the form of color-excess.

1.5 The Possible Existence of “Dark” Molecular Gas

In modern astronomy, “dark matter” is the non-baryonic component of the Universe that does not interact via the electromagnetic force. The adjective “dark” evolved to the current astronomical definition in the last decade; before that, dark matter was any under-luminous matter that was difficult to detect spectroscopically. Since CO is the primary tracer of molecular hydrogen, a low CO/H₂ ratio ($< 10^{-6}$) could make large columns of H₂ difficult to detect (see Chapter 4 for more details on the CO/H₂ ratio). However, most researchers in this field are convinced that cold molecular gas in primarily molecular regions with low CO/H₂ ratio is not common (e.g. Dame, Hartmann, and Thaddeus 2001). In other words, CO surveys of the Galaxy are thought to detect the bulk of the molecular gas. Diffuse

⁵CII is the astronomical nomenclature for singly-ionized carbon, C⁺

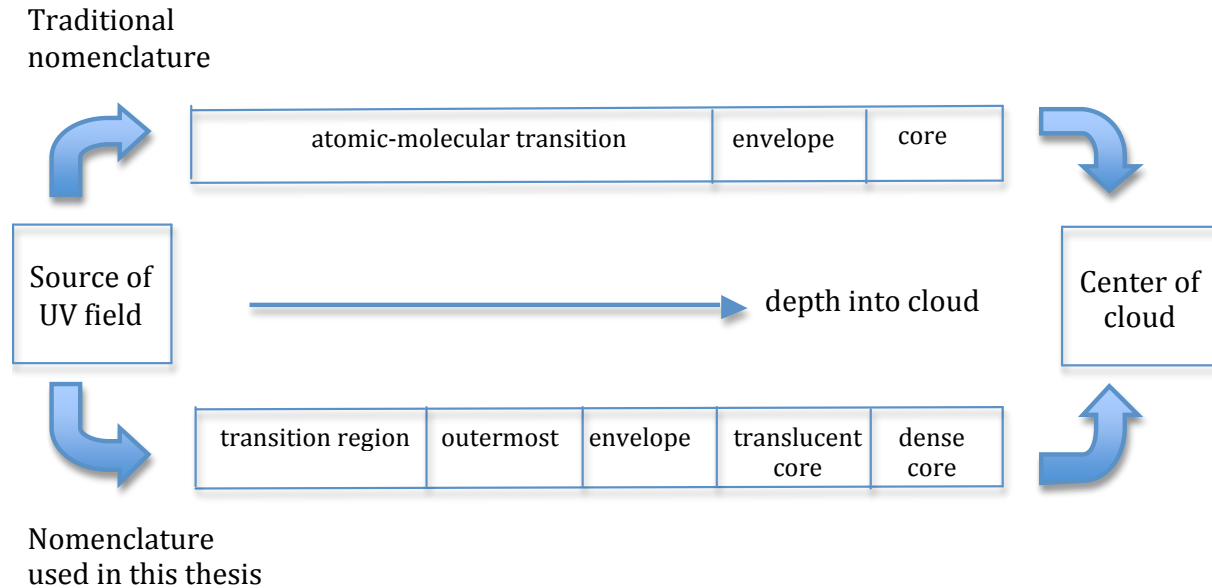


Figure 1.3: A comparison of nomenclature from past molecular studies of PDRs and the usage in this thesis.

molecular gas is thought to be but a minor constituent of the molecular component of the ISM.

This conclusion had been challenged recently by Grenier et. al (2005) who claim that substantial molecular gas in the Galaxy is “dark” in the sense that it is virtually invisible with conventional radio spectroscopic techniques. Grenier et. al used measured gamma-ray emission from the Energetic Gamma Ray Experiment Telescope (EGRET) in conjunction with estimated gamma ray emission to find areas of molecular gas surrounding known molecular gas. This gas was not detected by the conventional molecular surveys and thus Grenier et. al claimed to be tracing “dark” gas. They found this new “dark” gas to have gas-to-dust ratios comparable to that in local CO clouds, and determined that the mass of the “dark” regions should be comparable to the molecular mass. The idea that “dark” molecular gas exists in quantities comparable to the already known molecular gas from the large-scale

CO surveys is controversial. Most astronomers believe that widespread, cold, molecular gas is not present in the Milky Way. However, the question of whether the CO(1-0) surveys integrated long enough to probe the atomic-molecular region sufficiently to detect what is known as diffuse molecular gas is one of the central issues of this thesis. We will show in subsequent chapters that this diffuse region - undetected by the large scale surveys - and called the envelope and outermost regions in this thesis (see Figure 1.3) can be detected spectroscopically by both CO and OH observations.

1.6 Outline for Thesis

In this thesis we will analyze the molecular content of the envelope region of translucent clouds (using the definition of an envelope region described above). In the past, this region was thought to be virtually impossible to detect with traditional molecular radio spectroscopy techniques. We will study the molecular properties of this region using the CO(J=1-0) line at 2.6 mm and the 18 cm OH main line transitions. Although the translucent cloud MBM40 will be the focus of this thesis, we will also apply our analysis techniques to the entire high-latitude sky.

In Chapter 2, we will discuss in detail the molecular component of the Galaxy and examine the role of these clouds locally and throughout the entire Galaxy. We will re-examine the Georgia/Harvard CfA high-latitude survey data (Hartmann et al. 1998; Magnani et al. 2000) in Chapter 3. Using these past high-latitude CO surveys along with the Schlegel, Finkbeiner and Davis dust maps we will establish that sensitive CO(1-0) measurements can be used to estimate the H₂ content in diffuse molecular gas at high Galactic latitudes.

In Chapter 4, we review the techniques for calibrating the CO-H₂ conversion factor. This conversion factor is key in converting our CO observations to the molecular hydrogen column density which, in turn allows us to obtain a molecular mass estimate. Using CO(1-0) data

collected from the 12-m Arizona Radio Observatory radio telescope we determine the CO-H₂ conversion factor for MBM40 and compare it to previous work in Chapter 5.

In Chapter 6, we use the new CO-H₂ conversion factor for MBM40 along with sensitive CO(1-0) observations to calculate the mass contained in the envelope of the cloud. This mass estimate is compared with that obtained from previous, traditional CO mapping of the denser regions of the cloud. In addition to the CO(1-0) data, we also observe the OH 18 cm line in the envelope of MBM40 and compare the mass obtained from that low-density tracer to the CO derived mass. This mass comparison from the two different molecules is done in Chapter 7. In Chapter 8, we summarize our results and apply them to the Galaxy in general in an attempt to determine how important diffuse molecular gas is to the molecular content of the Galaxy. We also comment on whether diffuse molecular gas can contribute to the “dark” molecular gas inventory that has been recently proposed. We close by discussing future avenues of research into this issue.

Chapter 2

Translucent Clouds and Their Molecules

2.1 Cloud Classification

In Section 1.4.1 we discussed how to characterize clouds on the basis of their gravitational state and the effects of external pressure. A more observational prescription for the smaller clouds is to divide clouds into different categories based on their dust content which attenuates visible light. The opacity of the cloud in the visual part of the spectrum is directly related to the extinction, A_V . van Dishoeck and Black (1988) divided the smaller molecular clouds into three categories: diffuse, translucent, and dark. The diffuse clouds are considered to be those objects with $A_V \leq 1$ mag and, in the past, were primarily studied by optical and UV astronomers detecting interstellar absorption lines along lines of sight towards early-type stars. Dark clouds have $A_V \geq 5$ mag and were the traditional, smaller, molecular clouds studied by radio astronomers since the mid 1960's. A new category, the translucent cloud, was devised by van Dishoeck and Black, with intermediate extinction: $1 < A_V < 5$ mag (see Table 2.1). This organizational scheme is used primarily with the smaller molecular clouds,

Type of Cloud	Extinction (mag)
Dark	$A_V \geq 5$
Translucent	$1 < A_V < 5$
Diffuse	$A_V \leq 1$

Table 2.1: Different types of small molecular clouds based on visual extinction

but, even for giant molecular clouds (GMCs), their outer layers have lower extinction and may be considered to be translucent (Polk et al. 1988). Most dark clouds are self-gravitating due to their relatively large mass and can contain very dense clumps, with $A_V > 10$, within the deeper regions of the cloud. Although most of the molecular mass in our Galaxy is found in GMCs, with individual cloud masses ranging from $\sim 10^4$ to $\sim 2 \times 10^5 M_\odot$, the smaller clouds play an important role in that some of them form low mass stars and, because they can be found closer to us than GMCs, the smaller clouds allow us to study their physical and chemical processes in the greatest detail. In addition, translucent clouds lie in the realm between diffuse clouds and dark clouds. Thus, as transition objects, their study is important for understanding molecular clouds in general, and thus for understanding the structure of our Galaxy.

Most clouds have clumpy substructures, called cores, where the number density is higher ($10^4 - 10^7 \text{ cm}^{-3}$) and the most intense molecular line emission is found. Outside the cores, clouds have a lower-density molecular substrate ($10 - 10^3 \text{ cm}^{-3}$) where the extinction can be much less than within the cores. In the traditional nomenclature shown in Figure 1.3, this substrate would be called an envelope region. It is translucent in terms of extinction and it is readily detectable with the CO(1-0) line. As discussed in Section 1.4.2, a transition region surrounds the translucent substrate and gradually merges into the atomic ISM. Molecular hydrogen is present in this region, but it was thought that radio spectroscopic detection of

molecular species here was not possible. Recent work by Liszt, Pety, and Lucas (2010) has shown that even regions with $A_V < 1$ mag can show strong CO(1-0) emission. In this thesis we will report on CO and OH observations of this diffuse transition region of the translucent cloud, MBM40. Furthermore, we change the nomenclature as described in Section 1.4.2. What is normally called the envelope of a molecular cloud, we now call the translucent core. We then break up the atomic-molecular transition region into an envelope, outermost, and then the transition region (see Figure 1.3). The reason for this somewhat subjective change in nomenclature is that we are studying translucent clouds that have lower extinction and densities than traditional clouds. From this point on, we will use only our newly-defined nomenclature.

Studying the envelopes and outermost regions of a translucent cloud is important because they provide a transition region between the traditionally mapped CO regions and the surrounding atomic medium. The boundary between the envelope and the surrounding medium is not very sharp. It will be seen later in this work that the envelope regions of translucent clouds can contain a substantial amount of molecular mass, thus making observation of these regions intriguing given recent ideas about “dark” molecular mass in the Galaxy (see Section 1.5 and Chapters 6 and 7).

Cloud boundaries, for the most part, are difficult to observe, and these boundaries can vary depending on what molecules or atoms used to observe the cloud and the sensitivity of the observations. Theories for cloud formation and cloud destruction often focus on one particular type of cloud, whether it be diffuse, translucent, dark, or a giant molecular cloud. But this approach does not give us the correct picture because any one cloud could have diffuse, translucent, and dark molecular regions. Some diffuse clouds exist as local density substructures located on the periphery of giant molecular clouds and there are even giant molecular clouds that are surrounded by larger atomic clouds (Elmegreen 1993b).

The structure of clouds can be shaped by three basic processes: shocks that accumulate

the gas into shells and filaments, the buildup of large clouds from collisions of smaller clouds, and instabilities that may exist within the ambient interstellar medium or inside pre-existing clouds or shells. By observing the general magnetic field alignment, Spoelstra (1972) and Cleary, Haslam, and Heiles (1979) found evidence that shells, which can resemble IRAS cirrus structures (see below), could be formed by shock compression. Many of these cirrus filaments contain dense round globules that are more or less equally spaced. This near equal spacing suggests that the filaments collapsed by some regular instability after they were swept up by a shock wave (Elmegreen 1987).

Many of the clouds located at high latitudes, $|b| \geq 30^\circ$, are translucent to diffuse in nature based on their low visual extinction A_V . The structure of these clouds tends to resemble smoke, having a wispy “cirrus”- like appearance. In the early 1980s the IRAS satellite revealed numerous clouds of infrared cirrus at 60 and 100 μm . The clouds were found to have irregular and complex shapes and were distributed over the entire sky. Clouds similar in structure to the core of the infrared cirrus are also seen in the 2.6 mm emission line of CO (Weiland et al. 1986). In two studies done by examining candidate regions compiled from the Palomar Sky Survey Prints (POSS-I), Blitz, Magnani, and Mundy (1984) and Magnani, Blitz and Mundy (1985), identified 493 patches with $A_V \leq 1$ at locations above 20° and below -20° in galactic latitude. They surveyed 448 of the patches, and detected CO(1-0) emission in 35 complexes located at high galactic latitudes, $|b| \geq 25^\circ$. This new survey of “high-latitude” molecular clouds provided the largest sample of translucent clouds then known and opened up a new field of ISM study.

2.2 Observing Translucent Clouds

Molecular clouds have the obvious characteristic that they consist largely of molecular gas. However, molecular clouds may also have outer regions or boundaries with a rela-

tively large abundance of atomic species including hydrogen and carbon. To observe within the cloud and the boundaries of the cloud, we use molecular transitions, such as the 2.6 mm ($J = 1 - 0$) rotational transition of CO, to probe the various temperature and density regimes. Observed molecular transitions can have a wide variation in spontaneous decay from 10^{-8} s^{-1} to 10^{-4} s^{-1} (Jura 1987). This large difference in decay rates means that we must use caution in assuming an equilibrium population distribution of molecules. The lack of equilibrium population distribution can consequently mean that some of the transitions are not directly related to the kinetic temperature of the gas, but certain transitions of particular molecules can give information about the kinetic temperature in a relatively direct fashion, and therefore give us information on H_2 . The most important transitions for determining a kinetic temperature that relates directly to H_2 are the rotational transitions of CO. Despite the high opacity of the CO 2.6 mm line, it is an excellent tracer of the mass of the molecular gas. CO is the most useful tracer of H_2 , with its $J = 1 - 0$ emission line having a low spontaneous decay rate of $6 \times 10^{-8} \text{ s}^{-1}$, which requires a low density ($10^2 - 10^3 \text{ cm}^{-3}$) for thermalization. In most of the denser molecular environments, such as cloud cores, the 1-0 line is optically thick and the brightness temperature of the CO(1-0) transition is close to the kinetic temperature of the H_2 (Goldsmith 1987). A key problem in studies of molecular clouds is how to convert from observations of the CO(1-0) line to a column density of H_2 . The relationship between the velocity-integrated antenna temperature of CO to H_2 is empirically calibrated and is known as the X-factor or, X_{CO} . This key molecular parameter will be discussed in detail in Chapter 4. We now discuss some of the important molecular species for studying diffuse interstellar molecular clouds.

2.3 Molecular Hydrogen

2.3.1 Formation

The formation of molecular hydrogen can occur in many different ways, but only a few can actually occur on an astronomically realistic time scale. Hydrogen atoms interacting with each other have no electric dipole moment, and therefore cannot emit electric dipole radiation. The inability to emit this type of radiation equates to the system being unable to remove excess energy, therefore inhibiting the system from forming a molecule in the gas phase by collisional processes. Other pathways that lead to the formation of the hydrogen molecule in the gas phase are electric quadrupole transitions, three-body reactions between three hydrogen atoms, and the formation of H^- through radiative association of neutral hydrogen with a free electron. The quadrupole reaction and the three-body reaction have such low rate coefficients in the ISM that they can be completely ignored, but the formation of H_2 through H^- is possible but is dependent on the density on H^- , which can be very small in diffuse regions because the destruction rate of this ion is greater than its formation rate (Draine 2011).

In the gas phase the dominant formation pathway of H_2 is through associative detachment, where H^- combines with H to form H_2 and release an electron. Although associative detachment can form molecular hydrogen, overall grain catalysis is the main route for its formation in typical cloud environments. Grain catalysis requires a hydrogen atom to attach to a dust grain and if the attached H atom is not tightly bound to the grain surface, it wanders the surface of the dust grain until the bond between the hydrogen atom and the dust grain is strong enough to keep the hydrogen atom stationary. When another hydrogen atom attaches to the same dust grain surface it also wanders the surface and if this hydrogen atom encounters another H atom then they react to form H_2 . This reaction releases 4.5 eV worth of energy, allowing the newly formed molecule to be ejected from the grain surface.

2.3.2 Destruction

The destruction of H_2 in the ISM is mainly achieved through photodissociation:



The absorption of a photon leads to H_2 being excited to a higher electronic state and this leads to the molecule decaying to a vibrationally excited bound level of the electronic ground state. However, less frequently the excited H_2 molecule will decay to the vibrational continuum of the electronic ground state, where in approximately 10^{-14} s, the molecule will fly apart leaving two free H atoms (Draine 2011).

If the transitions that cause the photodissociation become optically thick due to a large number of absorbing particles, then the molecule is said to have self-shielded. The ability for a molecule such as H_2 to achieve self-shielding arises from it having a large enough density relative to the photon density such that all of the dissociating photons are absorbed before reaching molecules further within the cloud. In a sense, a sacrificial layer of H_2 molecules forms and absorbs the dissociating photons (by dissociating into atomic H) allowing interior H_2 molecules to survive. The sacrificial region, which consists of atomic and molecular hydrogen, is called the dissociation front and lies in the outer regions of a molecular cloud in the direction of an ultraviolet source. These regions form the outermost boundary of a molecular cloud. In the nomenclature of Chapter 1, this region is traditionally called the atomic-molecular transition region. In this thesis we break it up into a transition region, an outermost molecular cloud region and an envelope region, and study molecules in these regions.

2.3.3 Observing H₂ in the ISM Directly

It was clear even in the 1950's and 1960's that regions of high extinction were often accompanied by sharp decreases in HI. The speculation was that the gas must be present but was likely to be in molecular form. However, detecting H₂ is a difficult proposition. Molecular hydrogen contains two electrons, and in its electric ground state is a very symmetric molecule: it has zero electron spin, zero electronic orbital angular momentum and has no permanent electric dipole moment. This lack of an electric dipole moment causes the vibrational states and the rotational states to radiate very weakly and only through the quadrupole moment. This results in very weak, infrared, H₂ lines, which are difficult to observe from the ground and are not well suited to trace cold molecular gas, because most hydrogen in the ISM is in the ground state and the allowed rotational transitions have equivalent temperatures of thousands of degrees. Since we are interested primarily in relatively cold gas, the emission from the molecular species in the cloud must arise from rotational transitions.

The presence of molecular hydrogen in the ISM was not observed directly until it was done by Carruthers in 1970. He used a rocket-based ultraviolet (UV) spectrometer to observe the absorption of the electronic spectrum of molecular hydrogen toward the star ξ Persei. It is difficult to observe hydrogen in absorption because UV photons are needed to excite molecular hydrogen to its excited states and these transitions are blocked by the Earth's atmosphere. In addition, the hydrogen molecule needs to be along the line of sight to a strong background UV source. Thus, H₂ is difficult to observe in absorption, and even more difficult to detect in emission. In contrast, neutral atomic hydrogen in the ISM is easily detectable, within the radio part of the electromagnetic spectrum, by using the 21-cm line. This radio emission is produced by the "flipping" of the electron's spin. Although this process is very rare and takes on average a few million years to occur, the lines of sight in the ISM encompass so many H atoms that the HI 21 cm line is the strongest non-masing spectral line in the radio part of the spectrum (Carroll and Ostlie 1996). In summary, the most

abundant molecule in molecular clouds is difficult to detect. We thus turn to the second most abundant molecule, carbon monoxide or CO.

2.4 CO as a Tracer of Diffuse Molecular Gas

The lowest CO(1-0) transition was first detected in molecular clouds by Wilson, Jefferts, and Penzia in 1970. CO is symmetric, like H₂, but unlike H₂, it has an electric dipole moment, although it is a rather small one, only 0.110 Debye. The fundamental rotational frequency is 115.271 GHz which corresponds to a temperature of 5.5 K. CO has rotational levels that are more closely spaced than in H₂ and it also has many more allowed rotational and vibrational transitions than H₂. Both of these are a direct result of CO having a moment of inertia much greater than the one for H₂. Thus, CO's transitions are in the millimeter part of the radio spectrum and detectable from the Earth's surface, although the atmosphere is not completely transparent.

If the CO (1-0) transition is measured, a value for molecular mass can be determined using the ratio of the column density of molecular hydrogen to integrated antenna temperature of the CO (1-0) line, the so called X-factor, or X_{CO}. Draine (2011) predicts an X_{CO} value of $1.56 \times 10^{20} \text{ cm}^{-2} [\text{K km s}^{-1}]^{-1}$ using a density of total hydrogen, n_H, of 10^3 cm^{-3} and T_{ex} = 8 K. This correlates with recent observations from Dame et al. (2001) where X_{CO} was empirically determined to be $1.8 \pm 0.3 \times 10^{20} \text{ cm}^{-2} [\text{K km s}^{-1}]^{-1}$ for the local Galactic neighborhood. In Chapter 4 we will discuss in more detail the values we obtained and how they agree with calculations and past observations.

2.5 OH as a Tracer of Diffuse Molecular Gas

Since OH has nine electrons, the ground state has a non zero electronic orbital angular momentum, $L = 1$ and a non zero electronic spin, $S = \frac{1}{2}$. The spin and orbital angular momenta can couple, resulting in a splitting of two rotation energy ladders, called fine structure splitting. Each level in these two ladders is split two more times, first by Λ -doubling, into $+$ and $-$ states, then these are split into $F = 2$ and $F = 1$ states (hyperfine splitting). The ground state of OH is split into four hyperfine levels with four allowed transitions between them ranging from 1612 MHz to 1720 MHz, all in the 18 cm range (Draine 2011).

The hydroxyl (OH) molecule in the interstellar medium was first detected by Weinreb et al. (1963) through the measurement of the 18 cm absorption lines in the spectrum of the supernova remnant Cassiopeia A. The structure of hydroxyl is such that, in its ground state, four hyperfine transitions are produced at 1612, 1665, 1667, and 1720 MHz (see Table 2.2 and Figure 2.1). These transitions are the ones that are most commonly used to make spectroscopic observations of low and medium density gas in molecular clouds (see Wouterloot 1981). In order to obtain physically relevant parameters, observations must be made of the OH line as a function of its position in the cloud. The OH line parameters then can be readily converted to a column density, $N(\text{OH})$, because the 18 cm transitions are usually optically thin. If we can independently ascertain the OH abundance with respect to H_2 , then we can determine $N(\text{H}_2)$ from our OH observations and, from that, the mass of the cloud. By comparing the mass derived in this manner with that from other techniques, we can check whether our estimate of the OH abundance was reasonable.

Hydroxyl is a good candidate for probing low-density gas because it has rotational levels that are widely spaced and each are split by lambda doubling. This wide spacing and splitting of ground state rotational levels grants observers the ability to probe a wide variety

$F_j - F_i$	Frequency (MHz)	$A_{ji} (s^{-1})$
$1^+ \rightarrow 2^-$	1612.231	1.302E-11
$1^+ \rightarrow 1^-$	1665.401	7.177E-11
$2^+ \rightarrow 2^-$	1667.359	7.778E-11
$2^+ \rightarrow 1^-$	1720.529	9.496E-12

Table 2.2: Hydroxyl transitions of the lowest rotational state, with $^+$ and $^-$ corresponding to the spin of the electron.

of energy states and, thus, temperatures, from the ground state of hydroxyl. The $^2\Pi_{3/2}$ ground state of hydroxyl is composed of four hyperfine transitions at 18 cm (see Table 2.2), a portion of the electromagnetic spectrum that is very accessible from the ground. Since translucent molecular clouds are relatively cold (10 - 40 K) most of the OH will be in the ground state, making emission lines in this part of the spectrum likely to be fairly easily detectable (Magnani and Siskind 1990).

The ground state of hydroxyl is split into different levels because its electronic ground state is a $^2\Pi$ state, making it susceptible to Λ doubling, (see Figure 2.1). Since the two levels resulting from the Λ doubling are the result of the spin-orbit coupling of the nucleus and electron, the levels only differ in parity. These levels are split even further into hyperfine levels, denoted by the letter F, from the interaction between the nuclear magnetic dipole moment and the magnetic field induced by the orbiting electron. It is these four levels that allow hydroxyl to be observed through the use of low frequency radio techniques. The hyperfine, ground-state transitions are the basis of our investigation and should provide a robust estimate of N(OH) in translucent cloud envelopes. The rest frequencies and Einstein A coefficients of the four rotational lines that comprise the $^2\Pi_{3/2}$ electronic ground state of OH are listed in Table 2.2 (Destombes et al. 1977).

Thus, by using sensitive CO(1-0) observations at 115 GHz in conjunction with the OH

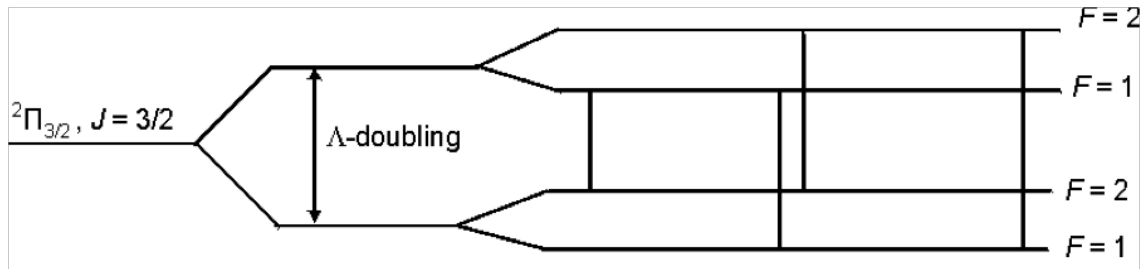


Figure 2.1: Ground state hydroxyl energy level $J=3/2$ with Λ doubling of the first electronic state. The splitting of the Λ doubled state results in the hyperfine lines, which are the rotational levels denoted by F numbers.

main line transitions at 1665 and 1667 MHz, in this thesis we attempt to trace the envelope and outermost regions of translucent clouds. These regions have been largely unexplored in molecular surveys because of the difficulty of detecting emission from any molecular species there. In the next chapter we begin by establishing a relationship between the CO(1-0) line and the dust column density at high-latitude.

Chapter 3

The E(B-V) Threshold: An Estimate of the Molecular Mass at High Galactic Latitudes

3.1 Introduction

The molecular clouds located above 30 degrees latitude in the northern Galactic hemisphere and below -30 degrees in the southern hemisphere are, somewhat arbitrarily, defined to be at “high Galactic latitudes”. Molecular gas found here is mostly associated with translucent ($1 < A_V < 5$ mag) and/or diffuse ($A_V \leq 1$) clouds, and, despite extensive work over the last two decades by Magnani, Blitz, and Mundy (1985), Magnani, Lada, and Blitz (1986), Hartmann, Magnani, and Thaddeus (1998), and Magnani et al. (2000) the precise amount of molecular gas at high latitudes is not well determined. Because the gas to dust ratio in the Galaxy is, on average, constant (Spitzer 1978), an estimate of the amount of gas at high latitudes can be made by knowing what fraction of the dust column density in a given direction is associated with H_2 . The dust column density can be measured by the Color Excess (E(B-

V)) - see below. If a relationship between $E(B-V)$ and H_2 (or its surrogate, CO) can be established, and if we can determine the distance of this gas, we can calculate a value for the total molecular mass at high Galactic latitudes. The distances to individual clouds can be measured using known distances of foreground and background stars projected on the clouds. In addition, a statistical measure of the average distances to the cloud ensemble can be determined if the velocity dispersion of the clouds and the local gravitational potential can be determined (Blitz et al. 1984). Following the distance estimates made by Blitz, Magnani, and Mundy (1984), Magnani, Blitz, and Mundy (1985) and Magnani, Hartmann, and Speck (1996), we determine, below, the amount of molecular gas at high Galactic latitudes using two estimates of the scale height of the clouds: 100 and 200 parsecs¹.

3.2 CO vs. $E(B-V)$ at High Latitudes

To get a better sense of the distribution of the molecular mass at high latitudes we divided our analysis into two sections, one for the northern Galactic hemisphere, $b \geq 30^\circ$, and the other for the southern Galactic hemisphere, $b \leq -30^\circ$. Taking advantage of publicly available data we used the dust survey done by Schlegel, Finkbeiner, and Davis in 1998 (hereafter known as SFD), which provides $E(B-V)$ values for the entire sky. $E(B-V)$ is also called Color Excess and is defined as the difference in magnitude between an unreddened and reddened line of sight of the B and V color bands, 442 nm and 540 nm, respectively. This Color Excess is proportional to the amount that an object is dimmed, its extinction, for a specific wavelength, A_λ . SFD combined the 100 μm maps of IRAS and the 100, 140, and 240 μm maps from the DIRBE instrument² to produce a database which had the calibration of DIRBE and nearly the resolution of IRAS (the resolution of the SFD database is $6.1'$). Using the ratio of the 100 μm to 240 μm emission from DIRBE, they were first able to deduce

¹The scale height here is the distance of the object above the Galactic plane.

²DIRBE was the IR imager on the COBE satellite.

a dust color temperature, which then allowed for the 100 μm emission to be converted to a column density of radiating dust. A map made in this fashion can be used to measure extinction and Color Excess because the column density of the interstellar dust is correlated with these quantities. The only assumption made by SFD concerns the distribution of dust grain sizes. They claim the distribution of dust is the same everywhere; basing this on the relationship between UV/optical extinction and far-IR emission which depend only on grain size distribution. Because the SFD survey is dealing with diffuse gas, they assume uniform dust properties, for the most part, including the traditional relationship between color excess (E(B-V)) and visual extinction A_V : $3.1 \text{ E(B-V)} = A_V$ (Schlegel et al. 1998).

In order to achieve a measure of the total molecular mass at high latitudes we eliminated any SFD E(B-V) data points with $|b| < 30^\circ$ then binned the remaining observations by E(B-V) values in increments of 0.01 mag. For the northern Galactic hemisphere, we used a cut-off point of 1.2 mag, because there was only one observation with an E(B-V) value greater than 1.2 mag. However, in the southern Galactic hemisphere there were 190 observations with an E(B-V) value greater than 1.2 mag, neither of the data sets over 1.2 mag were included. The larger number of observations with E(B-V) values greater than 1.2 mag in the southern hemisphere is primarily due to the Large and Small Magellanic Clouds, which lie at southern high latitudes. The results for the northern Galactic hemisphere are shown in Table 3.1, and the results for the southern Galactic hemisphere are shown in Table 3.2. For both tables column 1 represents the E(B-V) range and column 2 is the number of data points which lie in that specific E(B-V) range. Column 3 represents the total area, in steradians, that the observations cover in the sky and column 4 gives the average latitude where the specific E(B-V) range is found. Column 5 is the ratio of CO detections to observations, column 6 is the calculated column density of molecular hydrogen and columns 6 and 7 are the masses of molecular hydrogen for scale heights of 100 pc and 200 pc, respectively. The two hemispheres are over plotted with each other in the following four figures: Figure 3.1 is a zoomed-in plot

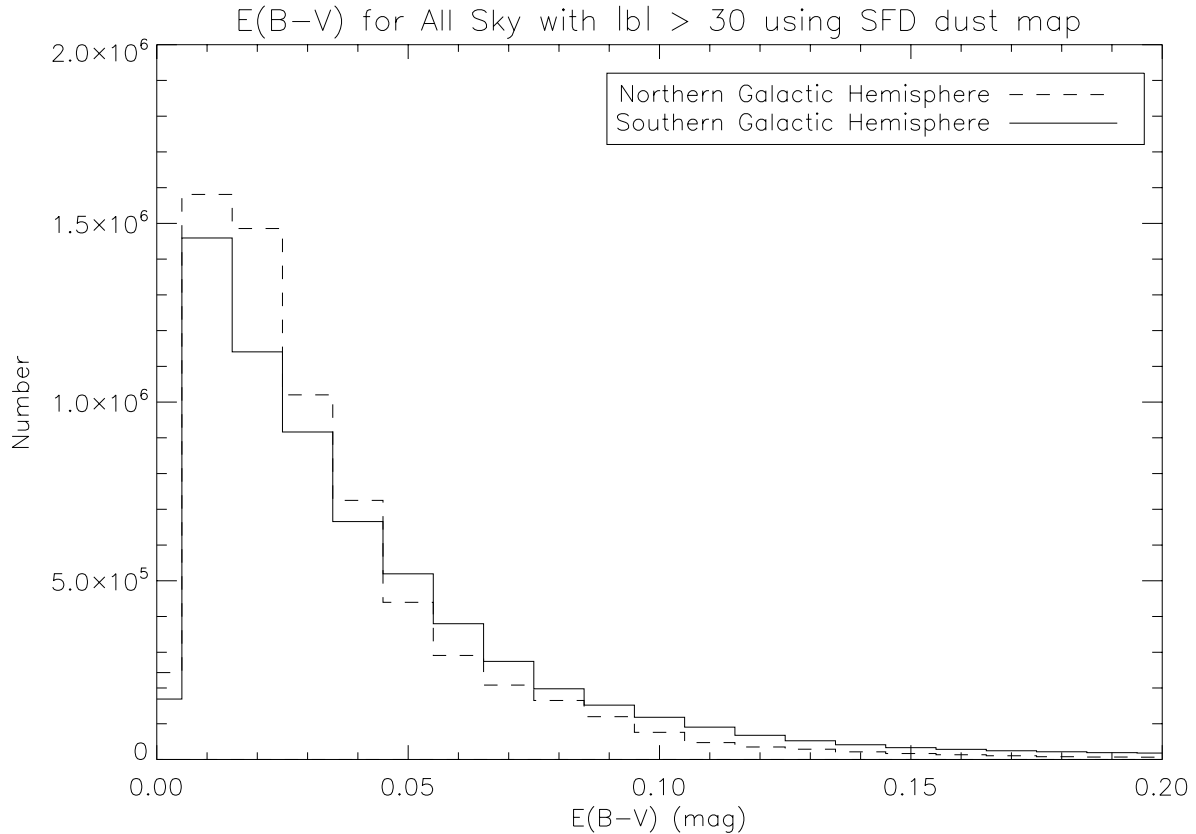


Figure 3.1: Histogram of $E(B-V)$ values from SFD for all positions with $|b| \geq 30^\circ$ up to $E(B-V)$ values of 0.20. Both the northern and southern Galactic hemispheres are shown, with the former designated by a dashed line and the latter by a solid line.

from 0 to 0.20 $E(B-V)$, Figure 3.2 shows the entire range from 0 to 1.20 $E(B-V)$, Figure 3.3 is a zoomed-in plot from 0.2 to 1.20 $E(B-V)$, and Figure 3.4 is similar to Figure 3.3, but with a zoomed-in y-axis. The asymmetry of the northern and southern Galactic hemispheres can be seen in these five plots.

To utilize this comprehensive data set of $E(B-V)$ measurements at high latitudes we compared the dust column density as measured by $E(B-V)$ to CO(1-0) observations for the same lines of sight. This was achieved by using two systematic CO surveys, where the high latitude sky at $|b| \geq 30^\circ$ was mapped in CO(1-0) at 1 degree intervals. Hartmann,

Table 3.1

Northern Galactic Hemisphere							
E(B-V) mag	Number of points	Area steradian	Average b deg	Ratio ^a	N(H ₂) ^b	Mass in M _⊙	
						100 pc ^c	200 pc ^c
0.00-0.05	5055071	11.93323	54.31	0	0.073	0	0
0.05-0.10	1223827	2.889022	39.75	0.0012	0.218	211.80	847.20
0.10-0.15	207874	0.490717	37.08	0.0265	0.363	1381.3	5525.4
0.15-0.20	54706	0.129141	35.60	0.0648	0.508	1337.0	5347.9
0.20-0.25	26978	0.063686	33.94	0.1164	0.653	1654.7	6618.9
0.25-0.30	11213	0.026470	33.20	0.1811	0.798	1359.9	5439.7
0.30-0.35	3800	0.008970	33.86	0.2591	0.943	752.51	3010.0
0.35-0.40	1502	0.003546	34.13	0.3502	1.088	457.36	1829.4
0.40-0.45	1084	0.002559	33.96	0.4545	1.233	489.72	1958.9
0.45-0.50	767	0.001811	34.41	0.5720	1.378	476.45	1905.8
0.50-0.55	495	0.001169	34.81	0.7026	1.523	409.11	1636.4
0.55-0.60	378	0.000892	34.75	0.8465	1.668	413.31	1653.2
0.60-0.65	256	0.000604	35.20	1	1.813	352.70	1410.8
0.65-0.70	133	0.000314	35.69	1	1.958	192.55	770.20
0.70-0.75	90	0.000212	36.35	1	2.103	135.61	542.43
0.75-0.80	85	0.000201	36.43	1	2.248	136.33	545.33
0.80-0.85	35	0.000083	36.22	1	2.393	60.376	241.50
0.85-0.90	23	0.000054	36.30	1	2.538	41.919	167.68
0.90-0.95	25	0.000059	36.17	1	2.683	48.456	193.83
0.95-1.00	20	0.000047	36.13	1	2.828	40.953	163.81
1.00-1.05	7	0.000017	35.76	1	2.973	15.336	61.344
1.05-1.10	5	0.000012	35.56	1	3.118	11.600	46.400
1.10-1.15	1	0.000002	35.55	1	3.263	2.4290	9.7160
Total Mass						9981.48	39925.9

Table 3.1: Calculation of the total molecular mass in the northern Galactic hemisphere. E(B-V) data are from SFD.

^a Ratio of CO detections to observations for given E(B-V) range.

^b $\times 10^{21} \text{ cm}^{-2}$.

^c Scale height.

Table 3.2

Southern Galactic Hemisphere							
E(B-V) mag	Number of points	Area steradian	Average b deg	Ratio ^a	N(H ₂) ^b	Mass in M _⊙	
						100 pc ^c	200 pc ^c
0.00-0.05	4350803	10.2707	-56.24	0	0.073	0	0
0.05-0.10	1523719	3.59696	-41.12	0.0012	0.218	249.30	997.19
0.10-0.15	369572	0.87243	-39.23	0.0265	0.363	2231.9	8927.7
0.15-0.20	126199	0.29791	-37.58	0.0648	0.508	2810.8	11243
0.20-0.25	76879	0.18148	-36.39	0.1164	0.653	4175.7	16703
0.25-0.30	50333	0.11882	-35.99	0.1811	0.798	5300.2	21201
0.30-0.35	29179	0.06888	-35.62	0.2591	0.943	5287.6	21150
0.35-0.40	21483	0.05071	-35.08	0.3502	1.088	6233.9	24936
0.40-0.45	14253	0.03365	-35.10	0.4545	1.233	6079.5	24318
0.45-0.50	8539	0.02016	-35.63	0.5720	1.378	4990.1	19960
0.50-0.55	4561	0.01077	-35.98	0.7026	1.523	3559.0	14236
0.55-0.60	2870	0.00678	-35.97	0.8465	1.668	2956.5	11826
0.60-0.65	1886	0.00445	-35.76	1	1.8130	2528.7	10115
0.65-0.70	1421	0.00335	-35.55	1	1.958	2071.3	8285.2
0.70-0.75	1073	0.00253	-35.66	1	2.103	1671.2	6685.0
0.75-0.80	841	0.00199	-35.40	1	2.248	1418.1	5672.3
0.80-0.85	646	0.00153	-35.29	1	2.393	1165.6	4662.3
0.85-0.90	553	0.00131	-35.17	1	2.538	1064.6	4258.3
0.90-0.95	382	0.00090	-34.49	1	2.683	804.26	3217.0
0.95-1.00	372	0.00088	-34.56	1	2.828	822.84	3291.4
1.00-1.05	292	0.00069	-33.59	1	2.973	714.01	2856.1
1.05-1.10	247	0.00058	-33.44	1	3.118	638.29	2553.2
1.10-1.15	190	0.00045	-33.21	1	3.263	520.24	2081.0
Total Mass						57293.7	229175

Table 3.2: Calculation of the total molecular mass in the southern galactic hemisphere. E(B-V) data are from SFD

^a Ratio of CO detections to observations for given E(B-V) range.

^b $\times 10^{21} \text{ cm}^{-2}$.

^c Scale height.

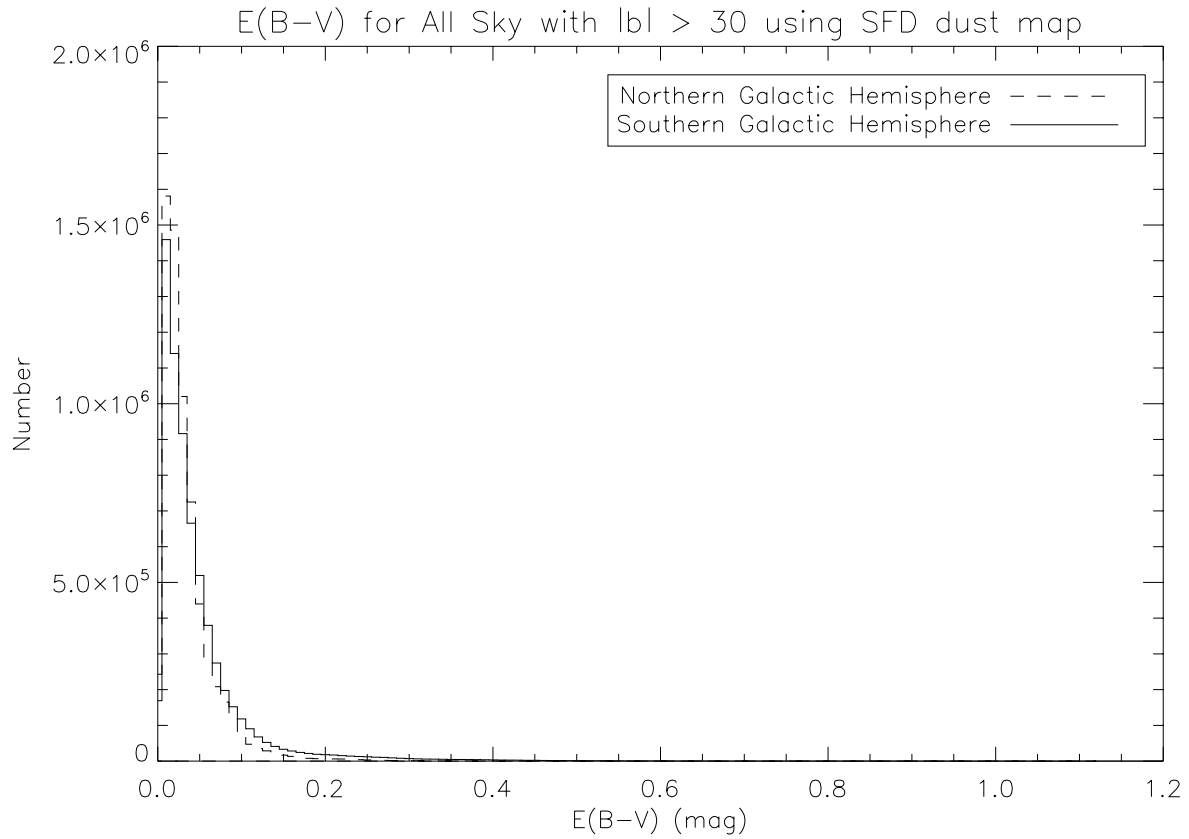


Figure 3.2: Histogram of $E(B-V)$ values from SFD for all positions with $|b| \geq 30^\circ$ up to $E(B-V)$ values of 1.20. Both the northern and southern Galactic hemispheres are shown, with the former designated by a dashed line and the latter by a solid line.

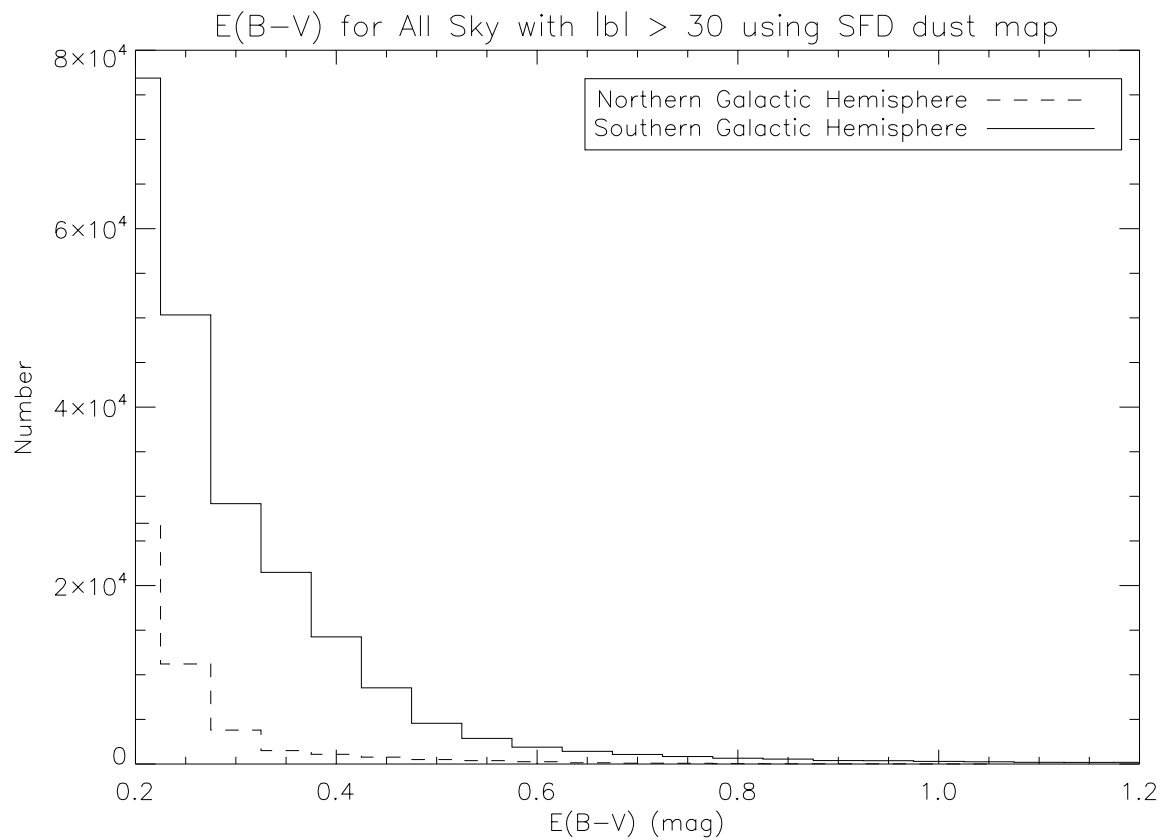


Figure 3.3: Histogram of E(B-V) values from SFD for all positions with $|b| \geq 30^\circ$, with E(B-V) values ranging from 0.20 to 1.20. Both the northern and southern Galactic hemispheres are shown, with the former designated by a dashed line and the latter by a solid line.

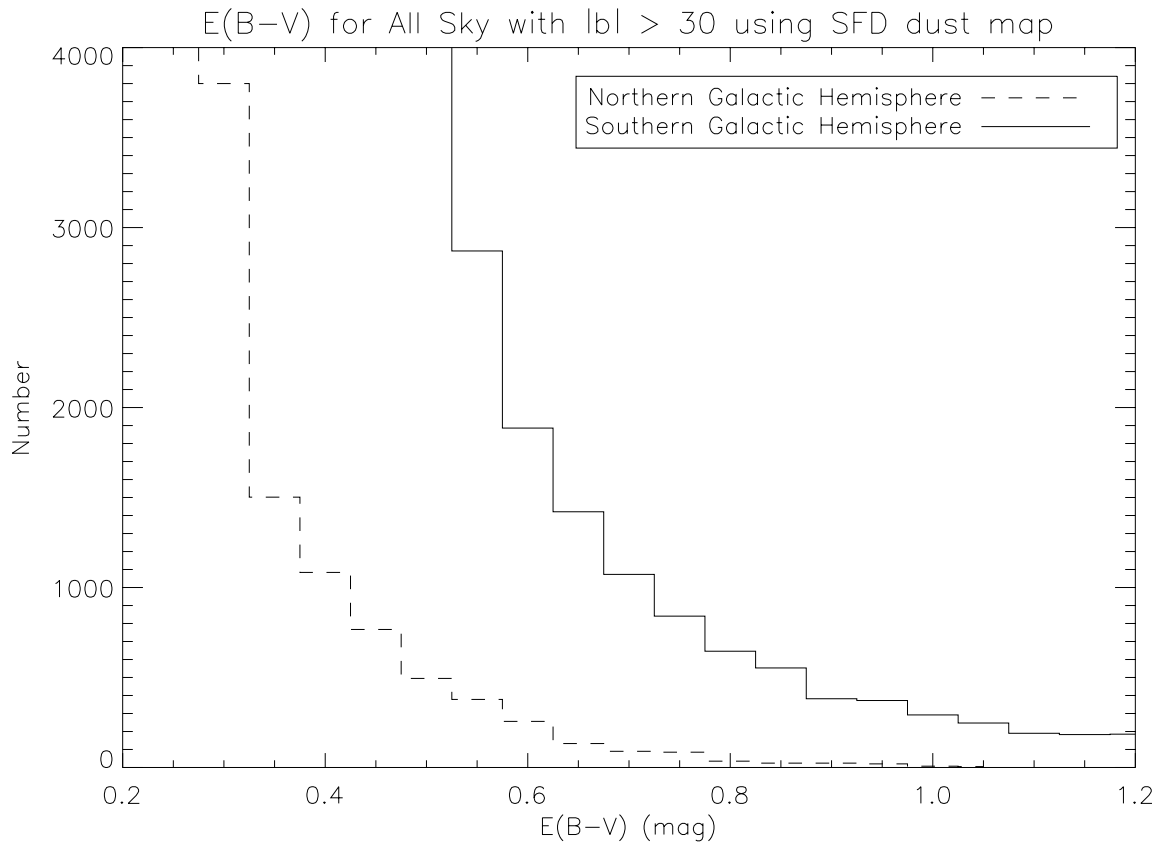


Figure 3.4: Histogram of $E(B-V)$ values from SFD for all positions with $|b| \geq 30^\circ$, with $E(B-V)$ values ranging from 0.20 to 1.20 but with magnified y-axis to show details of the distribution. Both the northern and southern Galactic hemispheres are shown, with the former designated by a dashed line and the latter by a solid line.

Magnani, and Thaddeus (1998) surveyed the northern Galactic hemisphere and Magnani et al. (2000) observed the southern Galactic hemisphere. The northern Galactic hemisphere survey at $|b| \geq 30^\circ$ consisted of 10562 points with only 26 CO detections (Hartmann et al. 1998), while the southern Galactic hemisphere survey consisted of 4982 points with 144 CO detections (Magnani et al. 2000). In total, 15555 observations were made, and the number of CO detections and non-detections versus $E(B-V)$ are shown in Figure 3.5. The resolution of the two datasets is nearly the same, $6.1'$ for SFD and $8.4'$ for the CO data. With this data we determined the ratio of CO detections to total observations for $E(B-V)$ values binned in increments of 0.05 mag, (see Figure 3.6). This ratio was also determined for $E(B-V)$ values binned in increments of 0.01 mag, and this more detailed, but noisier graph is shown in Figure 3.7. With this more detailed graph we were able to find a best-fit function (with an R squared value of 0.86) that related $E(B-V)$ to the number of CO detections:

$$\text{Ratio of Possible CO Detections} = 2.637(E(B - V))^2 + 0.108E(B - V) - 0.011 \quad (3.1)$$

The best fit curve that determined this equation is also shown in Figure 3.7. We multiplied this function by the total number of observations on the SFD map that lie in a specific bin of $E(B-V)$ values, in increments of 0.05 mag, giving us the total number of observations at high latitudes that could potentially, on average, contain CO detections for each $E(B-V)$ range.

We then used the gas to dust relation from Bohlin, Savage, and Drake (1978):

$$N(\text{HI} + \text{H}_2)/E(B - V) = 5.8 \times 10^{21} \text{ atoms cm}^{-2} \text{ mag}^{-1} \quad (3.2)$$

where, $N(\text{HI} + \text{H}_2) = N(\text{HI}) + 2N(\text{H}_2)$, to determine the total hydrogen column density. Since we are estimating the molecular content, for these lines of sight we will first assume all the gas is molecular by setting $N(\text{HI}) = 0 \text{ cm}^{-2}$ and dividing $N(\text{HI} + \text{H}_2)$ by 2. In this way, we obtain an upper value of the column density of molecular hydrogen, $N(\text{H}_2)$, for the

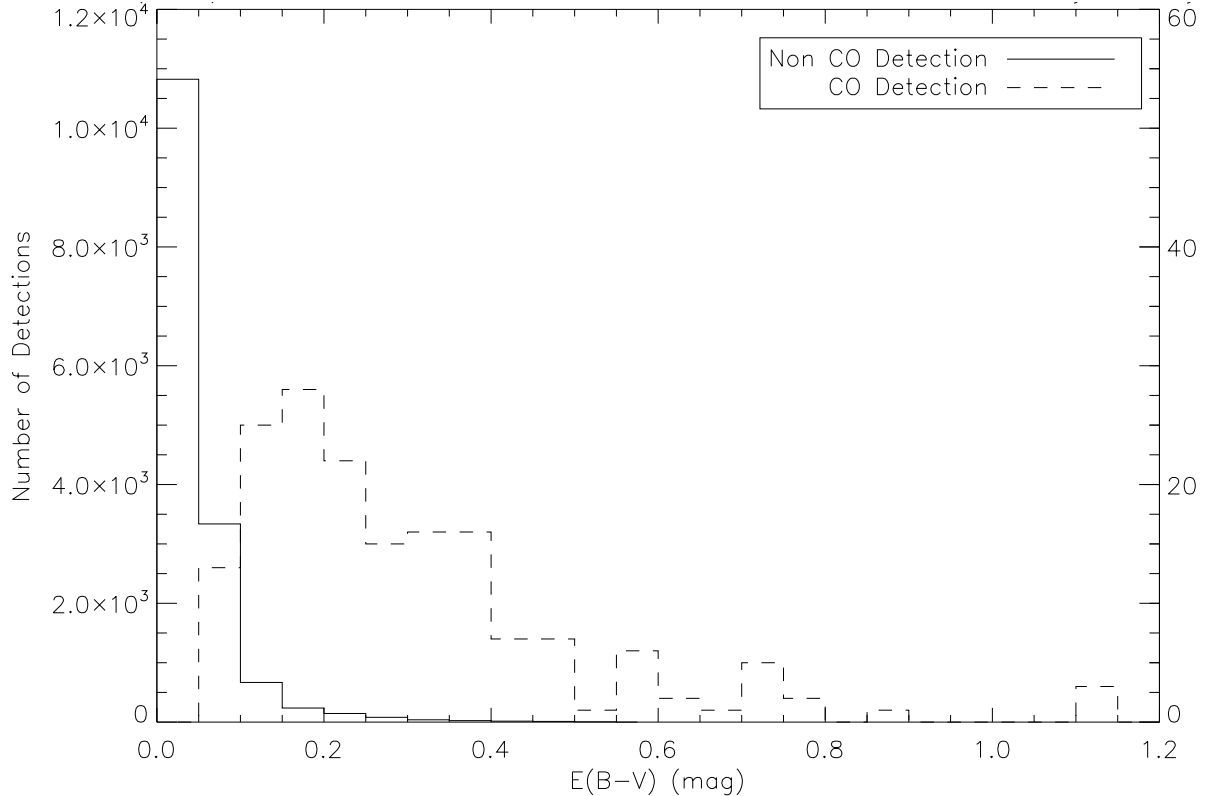


Figure 3.5: Histogram of non CO detections (left-hand y-axis) to detections (right-hand y-axis) versus $E(B-V)$, for all positions with $|b| \geq 30^\circ$, with $E(B-V)$ values contained in bins of 0.05 mag. The northern Galactic hemisphere is from Hartmann, Magnani, and Thaddeus (1998) and the southern Galactic hemisphere is from Magnani et al. (1998).

specific $E(B-V)$ range. This will give an upper limit to the amount of $N(H_2)$ because we are not accounting for the HI contribution.

We now have the upper limit value $N(H_2)$ associated with a given $E(B-V)$ range. This is displayed in column 6 of Tables 3.1 and 3.2. Equation 3.3 calculates the total area for each $E(B-V)$ bin, from which we are able to estimate the total mass at high latitudes, using the following elements: the number of observations that lie within a specific range of $E(B-V)$ values on the SFD map, $N(E(B-V))$, the solid angle, Ω , of each resolution element from the SFD data (0.0078 square degrees, or 2.361×10^{-6} steradians), and the distance to

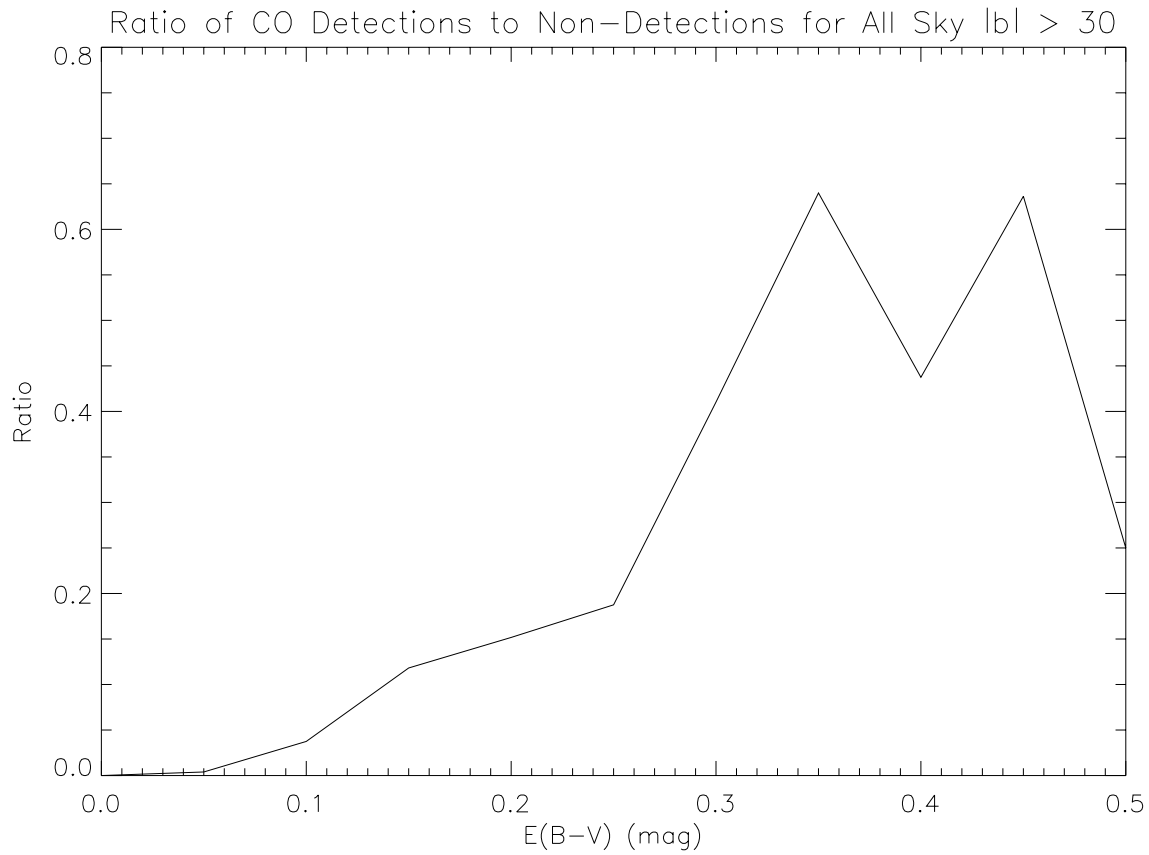


Figure 3.6: Ratio of CO detections to observations versus $E(B-V)$, for all positions with $|b| \geq 30^\circ$, plotted as a moving average of $E(B-V)$ bin values of 0.05 mag. The northern Galactic hemisphere is from Hartmann, Magnani, and Thaddeus (1998) and the southern Galactic hemisphere is from Magnani et al. (1998).

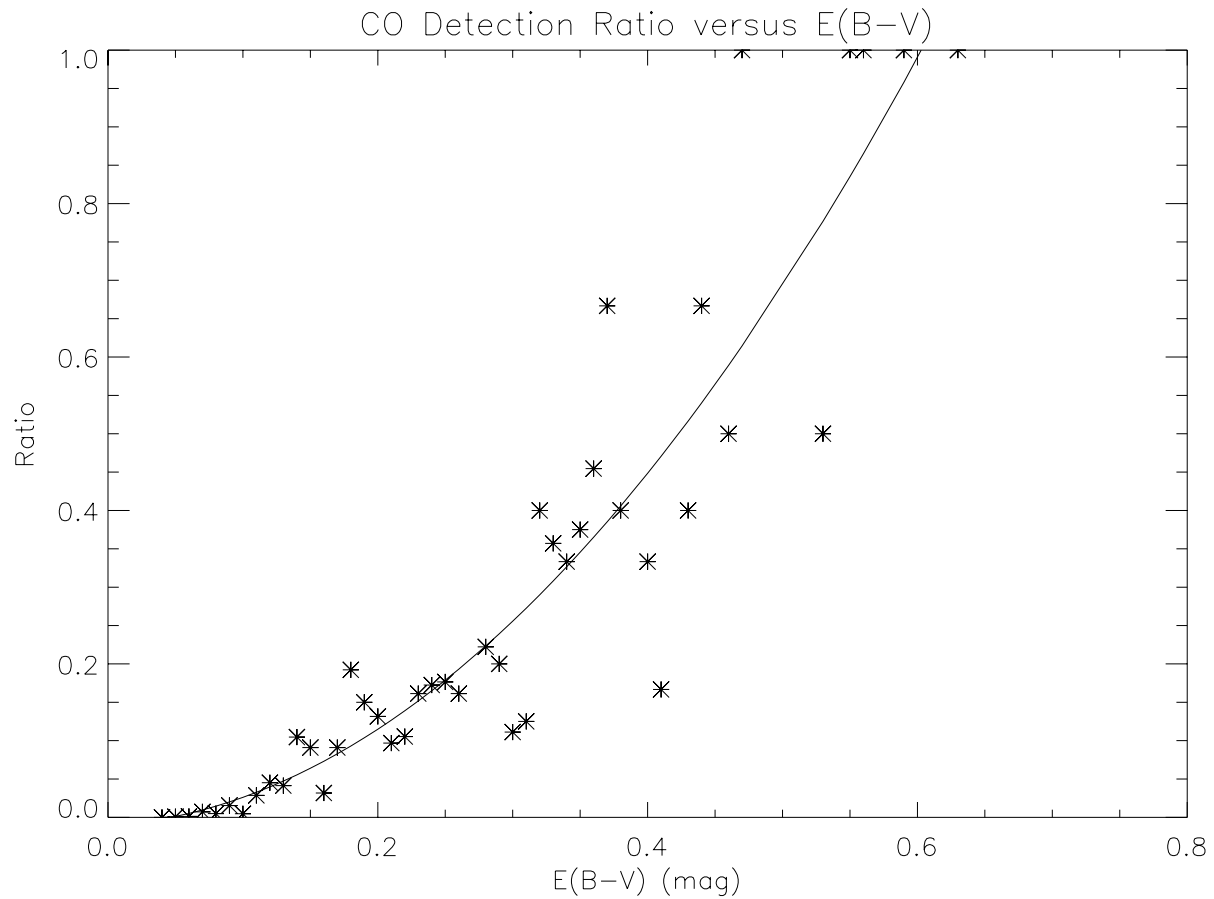


Figure 3.7: Ratio of CO detections to observations versus $E(B-V)$, for all positions with $|b| \geq 30^\circ$, with $E(B-V)$ values contained in bins of 0.01 mag. A best fit line is superimposed over the data (see Equation 3.1). The northern Galactic hemisphere is from Hartmann, Magnani, and Thaddeus (1998) and the southern Galactic hemisphere is from Magnani et al. (1998).

each element found by using the average Galactic angle, b , for each E(B-V) bin, and the two estimated scale heights, h , of 100 and 200 parsecs (Schlegel et al. 1998). The Galactic angle was averaged for each E(B-V) range, giving a more reasonable statistical estimate of the distance to each measurement. Thus the total area, $A_{E(B-V)}$, at high latitude for each E(B-V) range was estimated.

$$A_{E(B-V)} = N_{(E(B-V))} \cdot \Omega \cdot [(h/\sin(b))^2] \text{ steradian} \quad (3.3)$$

Once the total area is known for each E(B-V) bin, that value is multiplied by the calculated function, Equation 3.1, that relates the percentage of potential CO detections to each E(B-V) value. This in turn gives the upper limit total area, at high latitudes, that could potentially contain CO. We will call this quantity A_{H_2} .

The relationship between mass, area, and $N(H_2)$ is given by Equation 3.4. To calculate the mass for a given E(B-V) range, we multiply the total area which contains possible CO detections with the derived $N(H_2)$ for that bin of E(B-V) values and the molecular mass function, $\mu = 1.33$ (which accounts for the helium fraction), to obtain a value for the total molecular mass for a specific E(B-V),

$$\text{Total Molecular Mass} = A_{H_2} \cdot N(H_2) \cdot \mu \cdot m_{H_2} M_{\odot} \quad (3.4)$$

here, m_{H_2} is the mass of a hydrogen molecule. Two values of A_{H_2} were used, one corresponding to 100 pc and one to 200 pc scale height. The results are tabulated in columns 7 and 8 of Table 3.1 and Table 3.2.

3.3 Discussion

Upon inspection of Table 3.1 and Table 3.2 it can be seen that the vast majority of the high latitude sky is in a low E(B-V) range, and that most of the high extinction observations are located at $|b| \leq 35^\circ$. Over 98% of the northern Galactic hemisphere is at an E(B-V) value lower than 0.15 mag and more than 99.9% has E(B-V) values lower than 0.30 mag, which is clearly in the diffuse cloud realm. The southern Galactic hemisphere differs somewhat from its northern counterpart with over 94% of the southern Galactic hemisphere containing E(B-V) values lower than 0.15 mag and over 98% with E(B-V) values in the diffuse cloud realm. Another major difference is that in the northern hemisphere the number of observations with E(B-V) values greater than 1.00 mag is only 13, while the southern hemisphere has 729 points greater than that value. This difference is partially due to the Large and Small Magellanic clouds which lie in the southern hemisphere where most of the high E(B-V) values can be found. This asymmetry is also thought to be caused by our northern displacement of ~ 30 pc above the Galactic plane and our location in the local bubble. Where the northern hemisphere of the local bubble is more diffuse than the southern hemisphere of the local bubble. Finally, in both hemispheres, only the observations with very low E(B-V) values, less than 0.1 mag, have an average galactic latitude greater than 40° . The high average galactic latitude places most of the extremely diffuse gas ($E(B-V) < 0.20$ mag) in the very high latitudes, relatively far from the galactic plane, while observations with higher E(B-V) values have average positions close to $|b| \sim 35^\circ$.

The E(B-V) value is directly proportional to the column density of molecular hydrogen and, therefore, directly proportional to the mass of molecular hydrogen. Using this fact we were able to calculate the total mass of molecular hydrogen to be $1.0 \times 10^4 M_\odot$ in the northern Galactic hemisphere, if a scale height of the Galaxy is assumed to be 100 pc. When using a scale height of 200 pc the mass becomes $4.0 \times 10^4 M_\odot$, which is a factor of four

more than when the 100 pc scale height is used because of the d^2 factor in Equation 3.3. Now using the same initial scale height of 100 pc, the southern Galactic hemisphere was calculated to be near an order of magnitude greater than its northern counter part with a total molecular mass of $5.7 \times 10^4 M_\odot$, and at a scale height of 200 pc a value of $23 \times 10^4 M_\odot$ was calculated for the mass of H_2 . The northern/southern asymmetry is consistent with the results of the northern and southern CO surveys described by Magnani et al. (2000).

In an attempt to achieve a more complete survey of the total molecular mass at high latitudes we estimate an upper limit for $N(HI)$, we estimate that the maximum possible contribution from HI in the high latitudes could be 90% of the total H column density, therefore we obtained N_{TOTAL} from $E(B-V)$ using Equation 3.2 and we set $N(H_2)$ equal to 10% of this value. The lower limit mass contribution of H_2 from this estimate yields, in the northern Galactic hemisphere $2.0 \times 10^3 M_\odot$, and in the southern Galactic hemisphere, $11.5 \times 10^3 M_\odot$ (see Table 3.3). These estimates are important when compared to the results of Magnani et al. (2000) for the southern Galactic hemisphere. Those researchers estimated that the southern hemisphere contained $1.4 \times 10^3 M_\odot$ of molecular gas based on estimating the number of molecular clouds and assuming a distance of 140 pc for them. If we scale our results for the south to a distance of 140 pc, we get limits on the mass between $1.1 \times 10^5 M_\odot$ and $2.2 \times 10^4 M_\odot$ for all the hydrogen in molecular form and 10% of H in molecular form, respectively. This significant discrepancy implies that the assumptions underlying the work presented here and in Magnani et al. (2000) are very different (because the data set used is identical). If the estimate presented in this thesis is based on more reliable assumptions, there might be no need to assume a “dark” molecular component to the high-latitude molecular gas inventory.

Table 3.3

Lower Limit of H ₂ Mass			
E(B-V)	N(H ₂) ^a	Mass in M _⊙ ^b	
mag	cm ⁻²	NGH	SGH
0.00-0.05	0.145	0	0
0.05-0.10	0.435	42.360	49.860
0.10-0.15	0.725	276.27	446.39
0.15-0.20	1.015	267.39	562.17
0.20-0.25	1.305	330.95	835.13
0.25-0.30	1.595	271.99	1060.0
0.30-0.35	1.885	150.50	1057.5
0.35-0.40	2.175	91.471	1246.8
0.40-0.45	2.465	97.944	1215.9
0.45-0.50	2.755	95.290	998.02
0.50-0.55	3.045	81.822	711.80
0.55-0.60	3.335	82.662	591.31
0.60-0.65	3.625	70.539	505.74
0.65-0.70	3.915	38.510	414.26
0.70-0.75	4.205	27.121	334.25
0.75-0.80	4.495	27.267	283.62
0.80-0.85	4.785	12.075	233.11
0.85-0.90	5.075	8.3838	212.92
0.90-0.95	5.365	9.6913	160.85
0.95-1.00	5.655	8.1906	164.57
1.00-1.05	5.945	3.0672	142.80
1.05-1.10	6.235	2.3200	127.66
1.10-1.15	6.525	0.4858	104.05
Total Mass		1996.30	11458.7

Table 3.3: Estimate for the lower limit of molecular hydrogen in the high latitudes, with E(B-V) data from SFD. NGH and SGH are the northern Galactic hemispheres and the southern Galactic hemispheres, respectively.

^a $\times 10^{20}$.

^bCalculated using a scale height of 100 pc.

3.4 Conclusion

Using both the northern and southern Galactic hemispheres, $E(B-V)$, and CO data we were able to get an estimate for the total amount of molecular mass located in the high Galactic latitudes. Using the 100 pc scale height we obtained upper limits of the molecular mass in the northern and southern Galactic hemisphere of $1.0 \times 10^4 M_{\odot}$ and $57.2 \times 10^3 M_{\odot}$, respectively, with an upper limit on the total molecular mass of $67.3 \times 10^3 M_{\odot}$ for both hemispheres combined. If we include a lower limit calculation we made using a 9:1 ratio of HI:H₂ the total molecular mass component for the high latitudes is $13.4 \times 10^3 M_{\odot}$. This is considered a lower limit because we pick a relatively high value of $N(\text{HI})$. These values are a reasonable estimate considering the amount of mass made up of molecular hydrogen is estimated to be $\sim 10^9 M_{\odot}$ (Lequeux 2005) for the entire Galaxy. Using these estimates there is roughly 10,000 times more molecular mass contained in the lower latitudes, the plane of the Galaxy, than in the high latitudes.

However, there may be more molecular gas at high-latitudes than previously estimated. This would have significant repercussions on the question of dark molecular gas at least at high-latitudes. If the analysis of this chapter is valid, the results should be reproducible by in-depth observations in specific clouds. We now turn to this question for the translucent cloud MBM40. We will first need to calculate the CO-H₂ conversion factor for this cloud. This task is undertaken in Chapters 4 and 5.

Chapter 4

A Brief Review of the X-Factor Calibration

4.1 Introduction

One of the most important properties of molecular clouds is the amount of H_2 in the cloud which, if known, can give an accurate measure of the cloud's mass, if the distance to the cloud is known. Knowing the amount of mass contained in the molecular portion of the ISM is critical to understanding the structure and evolution of galaxies given that the mass in galaxies cycle between star formation, evolution, death, and the atomic and molecular ISM, see Section 1.1. The empirical conversion factor between the molecular hydrogen column density $N(\text{H}_2)$ and the observed CO(1-0) line intensity, $\int T_{\text{mb}} dv$, where T_{mb} is the main beam antenna temperature or the brightness temperature of the spectral line integrated over velocity, is known as the X-factor, or X_{CO} ¹. An accurate estimate of this quantity is important for deriving the molecular mass of a cloud directly from CO observations. If we use an X_{CO} value that is significantly different from the correct value, then we are

¹The X-factor is formally defined as $N(\text{H}_2)/W(\text{CO})$ where $W(\text{CO})$ is the velocity-integrated antenna temperature. The units of the X-factor, or X_{CO} , are $\text{cm}^{-2} [\text{K km s}^{-1}]^{-1}$.

incorrectly estimating the cloud masses and, consequently, their role in the inventory of Galactic molecular gas.

The molecular mass of a cloud can be obtained through direct observation of hydrogen. From an astronomical perspective, molecular hydrogen can be seen in the far ultraviolet regime, where H_2 is in absorption, or at infrared wavelengths where excited H_2 appears in emission. From an observational point of view, these two regimes have their particular problems, as discussed in Chapter 2. Because of that, the best tool to determine the amount of H_2 in a cloud is to use the second most abundant molecule found in the ISM, carbon monoxide or CO, and then convert from the integrated main beam antenna temperature of CO to the column density of H_2 . The rotational transitions of this molecule occur in the millimeter portion of the spectrum and have served as a proxy for $N(\text{H}_2)$ for nearly four decades. However, the line strength of the CO rotational transition, in particular the CO(1-0) rotational transition at 2.6 mm, must be calibrated with $N(\text{H}_2)$. The intensity of the CO(1-0) emission line, or $W(\text{CO})$, is an easily observed quantity and has produced most of our knowledge about molecular clouds over the years.

Paradoxically, CO is a good tracer of $N(\text{H}_2)$ even though the line is optically thick. This surprising relation can be explained by characteristic turbulence within a molecular cloud. Photons from deep in the cloud can be observed if the portions of the cloud between the detector and the photons do not shadow each other in phase space. For that reason, if two regions of the cloud in the same line of sight are traveling at different velocities, then both of the regions can be observed because of the different Doppler shifts (Tauber et al. 1991). If this way of lifting the optical thickness of the material were the only mechanism, then the transition would effectively be optically thin and not thick. In real clouds, there is still Doppler shadowing of material along the line of sight, so the key to using this transition as a mass tracer is subtler. An optically thick transition, produced in a turbulent velocity field that lifts only some of the Doppler shadowing, can trace mass via the virial theorem and

the size-line width relation for molecular clouds. These are empirically derived relationships believed to hold in most molecular clouds (Solomon et al. 1987). The virial theorem connects the line widths averaged over the cloud to the mass (Tauber et al. 1991), and a size-line width relationship for molecular clouds relates the cloud linear size to the line width averaged over the cloud (Myers and Goodman 1988). Both empirically-determined relationships produce the desired effect: as the path length through the clouds increases, so does the line width; as the line width increases, so does the mass. In this way the integrated CO line strength, which increases proportionally with the line width, can be linked to the cloud mass.

The above argument is well-established for GMCs which are believed to be in virial equilibrium (Solomon et al. 1987). However, not all molecular clouds are virialized. In particular, most high-latitude molecular clouds, and perhaps most translucent molecular clouds, are not in virial equilibrium (Magnani et al. 1985). Thus, X_{CO} is not likely to be constant in these objects. Magnani and Onello (1995) confirmed this hypothesis by determining X_{CO} for high latitude clouds using the CH technique which will be described in Section 4.7.

4.2 Techniques for Calibrating X_{CO}

Because X_{CO} may vary with respect to $W(\text{CO})$ in translucent clouds (Magnani and Onello 1995; Magnani et al. 1998), it is imperative to determine what is the range of this factor in the clouds under study. We begin by reviewing examples of the X_{CO} values, in units of $10^{20} \text{ cm}^{-2} [\text{K km s}^{-1}]^{-1}$ for both Giant Molecular Clouds (GMC's) and the smaller clouds, and the methods by which the factor was originally calibrated. Calibration requires a surrogate tracer for $N(\text{H}_2)$ and a map of $W(\text{CO})$ for the region. Simple division of $N(\text{H}_2)$ as derived from the surrogate by $W(\text{CO})$ for the appropriate lines of sight then yields X_{CO} . The basic results for the various methods are listed in Table 4.1

Ways to Calibrate X_{CO} in Molecular Clouds

Authors	Surrogate for $N(\text{H}_2)$	$X_{\text{CO}} \times 10^{20}$	Type of Cloud
Sanders et al. (1984)	A_V	$X_{\text{CO}} \approx 3.6$	GMC's, dark clouds
Scoville et al. (1987)	virial theorem	$X_{\text{CO}} \approx 3.0$	GMC's, dark clouds
de Vries et al. (1987)	far IR	$X_{\text{CO}} \approx 0.5$	translucent clouds
Strong et al. (1988)	cosmic gamma rays	$X_{\text{CO}} \approx 2.3$	GMC's
Magnani and Onello (1995)	CH	$0.3 < X_{\text{CO}} < 9$	translucent clouds

Table 4.1: X_{CO} calibration methods and typical values. Units of X_{CO} are $\text{cm}^{-2} [\text{K km s}^{-1}]^{-1}$.

4.3 Extinction Method

The oldest technique in determining the amount of molecular hydrogen employs extinction measurements to determine $N(\text{H}_2)$, using the traditional assumption of a constant gas-to-dust ratio (Spitzer 1978). The visual extinction is empirically calibrated to the total H column density by the relation $A_V = 5.3 \times 10^{-22} [2N(\text{H}_2) + N(\text{HI})]$ (Bohlin et al. 1978). This relationship is obtained first by assuming that the color excess, $E(\text{B-V})$, is roughly equal to $A_V/3.1$ and then by using the empirically determined relationship between $E(\text{B-V})$ and $N(\text{H}_{\text{TOTAL}})$;² $N(\text{H}_{\text{TOTAL}}) = E(\text{B-V}) 5.8 \times 10^{21} \text{ atoms cm}^{-2} \text{ mag}^{-1}$. The Color Excess being the difference in the observed color index of a star and the known color index based on spectral type of that star (Bohlin et al. 1978). This method works well for dark clouds and dense molecular cores in GMC's with $A_V > 5 \text{ mag}$, because determining the extinction in dark clouds and dense molecular cores is relatively straightforward using star counts. In

² $N(\text{H}_{\text{TOTAL}})$ is $2N(\text{H}_2) + N(\text{HI})$.

addition, in these objects, most of the hydrogen is in its molecular state due to the higher densities associated with these clouds, so no correction for $N(\text{HI})$ is needed. In translucent clouds this method is flawed because HI is often as prevalent as H_2 along a given line of sight, and determining accurate values of $N(\text{HI})$ is difficult in translucent clouds because of the large HI beam sizes compared to the resolution of the $W(\text{CO})$ maps. In addition, associating a given velocity range of HI with the molecular cloud is often based solely on guesswork. Thus an accurate estimate of $N(\text{H}_2)$ is precluded. A final problem with this technique is that most translucent clouds are at high galactic latitudes where there are fewer stars per unit area, and leading to greater uncertainties in A_V .

4.4 Virial Theorem Method

Another traditional method uses virial equilibrium to derive the mass of a cloud and therefore the amount of H_2 . Virial equilibrium assumes that the forces causing the cloud to collapse, gravitational and external pressure, balance the forces that are causing the cloud to expand, such as thermal pressure and turbulent pressure (McKee and Zweibel 1992). Under the assumption of virial equilibrium the velocity dispersion of the line, σ_ν , is used to calculate the mass of the cloud using $M = kR\sigma_\nu^2$, with k being a function of the density distribution and R the radius of the cloud (Wolfendale 1991). This method is used for GMC's but problems arise, such as determining the radius of the cloud, inevitably leading to uncertainties in the mass. The assumption that all GMC's are virialized, has been confirmed empirically by Solomon et al. (1987), but is not universally accepted (see, e.g., Maloney 1990). For high-latitude clouds, this is a moot point as most of these objects are, for the most part, not in virial equilibrium (Magnani et al. 1985). Even when calculating the mass of translucent high latitude clouds using the largest values reported for X_{CO} from the virial method many of the clouds have at least an order of magnitude less mass than what would be required

for virial equilibrium. If virial equilibrium cannot be established because the kinetic energy of the cloud is too great by 1-2 orders of magnitude, then, the cloud is not static but is breaking up on the sound-crossing timescale $\approx 10^6$ yrs (Magnani et al. 1985).

4.5 Far Infrared Method

The above methods are used to calibrate X_{CO} in GMCs, and dark clouds; however a newer technique for determining X_{CO} for translucent clouds uses infrared dust emission in the high-latitude clouds as a tracer, via the gas to dust ratio, of the hydrogen nucleons. This technique was used by deVries, Heithausen, and Thaddeus (1987) for translucent clouds and Bloemen, Deul, and Thaddeus (1990) on the Galactic scale, which results in a lower limit of X_{CO} . These investigators use the IRAS 100 μm band alone instead of in tandem with the 60 μm band because of the significant amount of emission from small grains and HII regions in the 60 μm band, thus causing unwanted contamination. It is assumed that the IRAS 100 μm radiance is proportional to the neutral atomic gas, due to heating from the Interstellar Radiation Field (ISRF). Thus, the total neutral atomic hydrogen column density along the line of sight and $W(\text{CO})$ is proportional to the infrared radiance at 100 μm , (I_{100}):

$$I_{100} = a_1 N(\text{HI}) + b W(\text{CO}) + I_{100}(\text{OFF}) \quad (4.1)$$

In this equation, a_1 is the infrared emissivity per atomic hydrogen nucleon, $b = 2a_2 X_{\text{CO}}$, where a_2 is the infrared emissivity per molecular hydrogen nucleon, and the last term is all the other infrared emission not associated with the cloud. All the quantities in Equation 4.1 can be derived from observations, and, if we assume $a_1 = a_2$ (i.e., the properties of the dust associated with the atomic gas are the same as those of the dust associated with the molecular gas), a value for X_{CO} can be derived (Magnani and Onello 1995). One problem that can occur with this method is that when radiation is absorbed by the molecular parts of the

cloud, grain heating is reduced and thus temperature gradients across the atomic-molecular transition region can form leading to an exaggerated X_{CO} value (Wolfendale 1991).

4.6 Gamma Ray Method

A fourth method described by Strong et al. (1988) and Bloemen (1991), uses large-scale surveys of HI, CO, and diffuse gamma ray emission to calculate X_{CO} . When cosmic rays interact with hydrogen nucleons, gamma rays are emitted, and the relationship between the cosmic ray flux and the column density of hydrogen nucleons is linear. This linear combination of $N(\text{HI})$ and $N(\text{H}_2)$, with $N(\text{H}_2)$ written as $W(\text{CO}) * X_{\text{CO}}$, can be best fit to the gamma ray distribution, thus giving a value for X_{CO} . A value of $2.3 \times 10^{20} \text{ cm}^{-2} [\text{K km s}^{-1}]^{-1}$ is given for X_{CO} in the inner Galaxy by Bloemen (1991). One of the major problems with this method is the relatively large angular resolution of the old gamma ray surveys; most are on the order of 1 degree, which is larger than many of the smaller translucent clouds. Unfortunately, the intensity of cosmic rays is only truly known near the Earth where it can be measured directly. In addition, many cosmic rays can travel through clouds without reacting with H_2 to form gamma rays, due to the relative low density in molecular clouds (Wolfendale 1991). There is the possibility that some clouds may be producing more gamma rays than others located in a less active cosmic ray region thus skewing results. The assumption that all clouds are bathed in the same cosmic ray flux density results in an overestimate of X_{CO} (Wolfendale 1991). Besides the overestimate of measured sources, there are currently no results for X_{CO} at high latitudes due to the lack of large-scale, detailed gamma ray surveys, though NASA's Fermi Gamma-ray Space Telescope will eventually produce an all-sky map.

4.7 CH Method

The CH method is a relatively new technique to determine X_{CO} . It is very useful because the hyperfine transitions of CH have been found in all types of molecular clouds (Magnani et al. 1989). This method assumes that the optically thin 3335 MHz CH hyperfine ground state transition is a linear tracer of $N(\text{H}_2)$, a good assumption for translucent clouds (Magnani and Onello 1995). The CH/ H_2 ratio is fairly constant over the range of translucent clouds (Liszt and Lucas 2002) so that once the column density of CH is obtained, $N(\text{H}_2)$ can be determined accurately to within a factor of a few. In particular, the column density of CH is determined from the main 3335 MHz line using the relation:

$$N(\text{CH}) = 2.82 \times 10^{11} T_{\text{ex}} / [\eta_f \eta_b (T_{\text{ex}} - T_{\text{BG}})] \int T_{\text{B}} d\nu \text{ cm}^{-2}$$

T_{ex} is the excitation temperature of the $^2\Pi_{1/2}$ $J = 1/2$ transition and T_{BG} is the background temperature (usually 2.7 K), with η_f representing the filling fraction of CH in the beam, η_b as the beam efficiency, and the integral is the integrated profile in units of T_{ex} (mK km s^{-1}). This can be converted to $N(\text{H}_2)$ by the empirical $N(\text{CH}) - N(\text{H}_2)$ relationship obtained by Mattila (1986)

$$N(\text{H}_2) = 2.1 \times 10^7 N(\text{CH}) + 2.2 \times 10^{20} \text{ cm}^{-2} \quad (4.2)$$

Therefore, CH observations of the 3335 MHz line lead directly to $N(\text{H}_2)$ and, at that point, all that is needed is a measurement of $W(\text{CO})$ along the lines of sight observed in CH to determine X_{CO} . We will use this technique coupled with our observations of CO in MBM40 to calibrate X_{CO} for various cloud regions, then determine the mass of the envelope of MBM40 (Magnani and Onello 1995).

4.8 Conclusion

We have just reviewed five different methods for calibrating X_{CO} , the CO-H₂ conversion factor. In the next chapter we will focus on just one of the previously discussed techniques, the CH method, to determine a value for X_{CO} for the translucent molecular cloud, MBM40. Upon deriving this estimate of X_{CO} we will obtain, in Chapter 6, an estimate of the amount of molecular hydrogen contained in MBM40.

Chapter 5

The X-Factor in MBM 40 at High Angular Resolution

5.1 Introduction

In 1982, Blitz, Fich, and Stark discovered interstellar CO(1-0) emission from a region located around $l = 37^\circ$ and $b = 44^\circ$. This region had been previously misidentified as an HII region by Sharpless (1959). The first CO mapping of the cloud at that location was done by Magnani, Blitz, and Mundy in 1985 during the survey in which they searched for high-latitude CO emission. Their rough mapping, which led to the first spatial and mass estimates of the cloud, laid the ground work for this thesis, from the mass to the shape of the cloud, and it was Magnani, Blitz, and Mundy who classified this cloud as MBM40. MBM40 is centered at $l = 37.6^\circ$ and $b = 44.7^\circ$ and is a translucent cloud, in addition to being one of a class of molecular clouds known as high-latitude molecular clouds, based on their location with respect to us.

The distance to MBM40 has been estimated by a few groups, such as Welty et al. (1989) and Penprase (1993), where Welty et al. (1989) used echelle spectra near the Na I D lines to

set an upper limit on MBM40's distance of $d \leq 140$ pc. . In 1993, Penprase constrained the distance to MBM40 to be between 60 and 290 pc using Na I absorption of stars behind the cloud, but he was able to narrow the distance down further to $90 < d < 150$ pc by using CH observations. This was an improved distance over the work by Welty et al. (1989) due to the additional foreground stars used to obtain a lower limit of the distance to MBM40 (Penprase 1993). For this work we have adopted a distance of 140 pc which is near the upper limit of Welty et al. (1989).

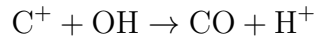
Past studies of CO by Magnani et al. (1995) used a 1' beam to probe CO in MBM40, and in this work we use the same size beam, but, in conjunction with more data points. A key difference between our data and previous data sets is that we use longer integration times which allows us to detect lower column densities of CO. With these longer integration times, we were able to probe the less dense envelope and outermost regions of MBM40 along with the traditionally studied core. Using these new CO data together with CH data collected by Chastain (2010) we obtain a value for X_{CO} which will help us determine, in the next chapter, the mass of H_2 in the cloud.

5.2 Astrochemistry of CO

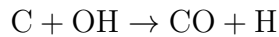
CO has $^1\Sigma^+$ symmetry in its electronic ground state, which means that transitions to states with $^1\Sigma^+$ or $^1\Pi$ symmetry are possible due to the strong electric dipole transitions that are allowed. Because there are no repulsive states that are $^1\Sigma^+$ or $^1\Pi$ symmetric and also accessible by photons with wavelengths greater than 912 \AA , most of the dissociation of CO by photons must occur through line absorptions into pre-dissociating states. These pre-dissociation states are excited states which are populated below their dissociation limit which then undergo radiation-less decay, which causes another state above CO's dissociation limit to be populated. The photo-destruction does not occur in the normal ISRF because

the threshold for ionization of CO is at 885 Å and the average ISRF is between 6 and 13 eV, equivalent to 2069 and 955 Å (Van Dishoeck and Black 1988).

Unlike OH, the translucent cloud models by van Dishoeck and Black (1986) estimate CO column densities that are lower by an order of magnitude than observed values. At low temperatures, the reaction



is enhanced and is the main formation route of CO in diffuse clouds. The main destruction process of CO is by photodissociation, and with a dissociation energy of 11.09 eV only photons with wavelengths $911.75 < \lambda < 1111.7$ Å can dissociate CO. The optical depth at which CO is strongly affected by the ISRF is not straight forward, since the dissociating lines can become optically thick and, at these wavelengths, H₂ can also be photodissociated or excited, therefore shielding the CO molecule. It is because of this shielding that the CO photodissociating rate decreases with cloud depth, but the decrease is not as large as with H₂ (van Dishoeck 1990). Other ways in which CO can form are from neutral-neutral reactions such as,



and this type of reaction plays a role in the production of many molecules with heterogeneous bond formation (Millar 1990).

Dense cores in dark clouds are difficult to see in the integrated ¹²CO intensity due to large optical depths of CO. However, ¹²CO linewidths are a good probe of large molecular clouds in virial equilibrium, because the cloud's mass is directly proportional to its velocity dispersion, as discussed in Chapter 4:

$$M_{\text{vir}} \approx R\Delta v^2/G$$

In this equation, R is the cloud radius, Δv is the FWHM of the line, and G is the gravitational constant (Friberg and Hjalmarson 1990). To determine the mass in denser clouds, species that are optically thin must be used, such as $C^{18}O$, ^{13}CO , and $^{13}C^{18}O$, but these techniques will not be discussed here because our study focuses only on translucent clouds and their envelopes which are difficult enough to probe with the lower ^{12}CO rotational transitions.

5.3 Observations

Observations of the $CO(1-0)$ rotational transition were made at the Arizona Radio Observatory (ARO) 12 m telescope at Kitt Peak National Observatory in December of 2008¹. The transition frequency of $^{12}CO(J = 1-0)$ is at 115 GHz and has an angular resolution of 1 arc minute using this telescope. The observations were made in position-switching mode with the off-source taken to be one degree east or west of the target in azimuth. The off positions were checked to be relatively free of dust emission using the Schlegel, Finkbeiner, and Davis (1998) dust maps. The spectrometer consisted of the 100 kHz and 250 kHz filterbanks that were chosen to provide velocity coverages of 62 and 167 $km\ s^{-1}$, respectively, with velocity resolutions of 0.26 and 0.65 $km\ s^{-1}$.

At the 12 m telescope, the $CO(J = 1-0)$ line antenna temperature (T_A^* - see Kutner and Ulich 1981) is corrected for the spillover and scattering efficiency of the antenna, so that the resulting quantity is T_R^* , the radiation temperature uncorrected for the antenna-beam coupling efficiency, η_{mb} . For the 12m telescope at 115 GHz, η_{mb} is approximately 0.85². Thus the main beam antenna temperature, T_{mb} , is equal to T_R^*/η_{mb} . Another correction factor is the beam dilution that we assume to be equal to 1 (in other words, the source fills the beam).

The observations consisted of 103 data points scattered throughout the cloud with the

¹The 12 m is part of the Arizona Radio Observatory and is operated by the University of Arizona with additional funding by the Mt. Cuba Astronomical Foundation.

²ARO 12 Users Manual: http://aro.as.arizona.edu/12_obs_manual/12m_user_manual.html.

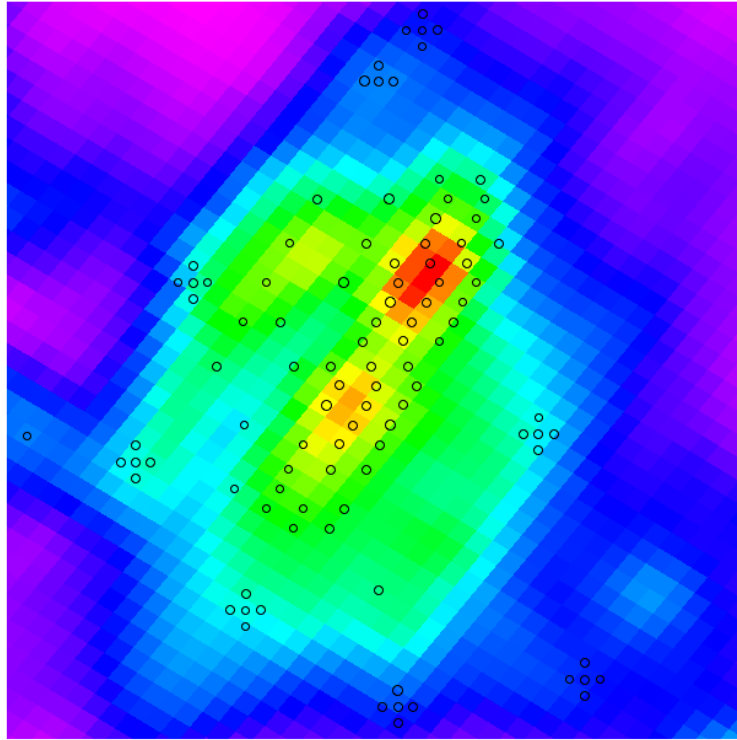


Figure 5.1: Positions of the CO(1-0) observations of MBM40 where the y axis is declination, increasing traveling up the page and the x axis is right ascension, decreasing traveling to the right. The coordinates are listed in Table 5.1 and the colors represent the Color Excess from the Schlegel, Finkbeiner, & Davis (1998) dust maps.

highest concentration of points within the core, see Figure 5.1. Typical integration times ranged from 5 to 10 minutes resulting in rms noise values from 0.06 to 0.11 K. In table 5.1 we list the observed lines of sight, the antenna temperature T_R^* , the line width (Δv), the LSR velocity v_{LSR} , and the integrated CO(1-0) main beam temperature ($W(\text{CO})$).

Table 5.1: Coordinates for the observed CO positions in MBM40.

Position	RA(2000) (deg)	Dec(2000) (deg)	T_R^* (K)	Δv (km s ⁻¹)	v_{LSR} (km s ⁻¹)	$W(\text{CO})^a$ (K km s ⁻¹)
CO_1	242.9500	21.5800	1.931 +/- 0.126	0.808	3.189	1.987 +/- 0.129
CO_2	242.8500	21.5800	2.062 +/- 0.110	0.810	3.288	2.128 +/- 0.114
CO_3	242.7400	21.6200	2.300 +/- 0.110	0.910	3.446	2.665 +/- 0.128
CO_4	242.8300	21.6200	3.852 +/- 0.121	0.830	3.278	4.073 +/- 0.128
CO_5	242.6300	21.6700	1.704 +/- 0.103	1.202	3.511	2.610 +/- 0.157
CO_6	242.7200	21.6700	3.520 +/- 0.110	0.999	3.411	4.478 +/- 0.140
CO_7	242.8000	21.6700	7.266 +/- 0.103	0.837	3.233	7.742 +/- 0.110
CO_8	242.6900	21.7100	6.404 +/- 0.102	0.757	3.317	6.175 +/- 0.098
CO_9	242.9283	21.7100	0.987 +/- 0.099	1.022	3.316	1.285 +/- 0.129
CO_10	242.7400	21.5000	0.245 +/- 0.098	0.781	-0.062	0.244 +/- 0.097
CO_11	242.8200	21.5000	0.488 +/- 0.107	0.167	-0.129	0.104 +/- 0.023
CO_12	242.7100	21.5400	0.820 +/- 0.093	0.535	3.072	0.559 +/- 0.063
CO_13	242.8000	21.5400	0.955 +/- 0.098	1.448	3.434	1.762 +/- 0.180
CO_14	242.8800	21.5400	1.123 +/- 0.088	0.988	3.395	1.412 +/- 0.111
CO_15	242.6600	21.6200	0.844 +/- 0.076	0.894	3.465	0.962 +/- 0.087
CO_16	242.6100	21.7100	1.494 +/- 0.088	1.029	3.595	1.959 +/- 0.116
CO_17	242.5800	21.7500	1.331 +/- 0.094	1.095	3.491	1.856 +/- 0.131
CO_18	242.6600	21.7500	5.755 +/- 0.102	0.974	3.398	7.141 +/- 0.127
CO_19	242.7500	21.7500	9.840 +/- 0.089	0.818	3.189	10.25 +/- 0.092
CO_20	242.5500	21.7900	0.906 +/- 0.109	1.557	3.546	1.797 +/- 0.216
CO_21	242.6400	21.7900	7.061 +/- 0.096	0.958	3.327	8.616 +/- 0.118
CO_22	242.7200	21.7900	9.112 +/- 0.085	0.809	3.315	9.389 +/- 0.087
CO_23	242.5700	21.8246	2.040 +/- 0.093	0.865	3.457	2.247 +/- 0.103
CO_24	242.6500	21.8246	5.616 +/- 0.085	0.905	3.476	6.472 +/- 0.098
CO_25	242.7400	21.8246	5.847 +/- 0.096	0.806	3.407	6.004 +/- 0.099
CO_26	242.5000	21.8800	1.669 +/- 0.103	0.709	3.542	1.508 +/- 0.093

continued on next page

Table 5.1 – continued from previous page

Position	RA(2000) (deg)	Dec(2000) (deg)	T_R^* (K)	Δv (km s ⁻¹)	v_{LSR} (km s ⁻¹)	$W(CO)^a$ (K km s ⁻¹)
CO_27	242.5800	21.8800	5.919 +/- 0.160	0.761	3.203	5.734 +/- 0.155
CO_28	242.6700	21.8800	8.104 +/- 0.136	0.586	3.151	6.053 +/- 0.101
CO_29	242.4700	21.9200	2.002 +/- 0.137	0.720	3.556	1.836 +/- 0.125
CO_30	242.5600	21.9200	7.215 +/- 0.150	0.850	3.239	7.809 +/- 0.162
CO_31	242.6400	21.9200	6.798 +/- 0.128	0.663	3.112	5.739 +/- 0.108
CO_32	242.4500	21.9600	2.584 +/- 0.104	0.691	3.342	2.274 +/- 0.092
CO_33	242.5300	21.9600	6.321 +/- 0.084	1.033	3.100	8.316 +/- 0.110
CO_34	242.6100	21.9600	7.765 +/- 0.078	0.657	3.105	6.496 +/- 0.065
CO_35	242.4200	22.0000	2.273 +/- 0.071	1.119	2.862	3.238 +/- 0.100
CO_36	242.5000	22.0000	5.137 +/- 0.073	1.137	3.023	7.442 +/- 0.105
CO_37	242.5900	22.0000	5.900 +/- 0.078	1.040	2.990	7.814 +/- 0.103
CO_38	242.4400	22.0400	4.514 +/- 0.074	0.811	2.840	4.665 +/- 0.076
CO_39	242.5200	22.0400	6.242 +/- 0.085	1.133	2.920	9.008 +/- 0.123
CO_40	242.6000	22.0400	6.057 +/- 0.093	0.803	2.851	6.193 +/- 0.095
CO_41	242.3700	22.0800	0.708 +/- 0.084	1.004	2.719	0.905 +/- 0.108
CO_42	242.4500	22.0800	6.468 +/- 0.086	0.931	2.997	7.671 +/- 0.102
CO_43	242.5300	22.0800	5.315 +/- 0.081	1.012	2.766	6.853 +/- 0.105
CO_44	242.4200	22.1300	3.919 +/- 0.091	0.695	2.839	3.471 +/- 0.081
CO_45	242.5100	22.1300	5.326 +/- 0.083	0.997	2.824	6.766 +/- 0.106
CO_46	242.4000	22.1700	1.472 +/- 0.083	0.819	2.647	1.536 +/- 0.086
CO_47	242.4800	22.1700	3.825 +/- 0.084	0.921	2.849	4.489 +/- 0.099
CO_48	242.8500	21.9200	2.188 +/- 0.075	0.848	3.044	2.362 +/- 0.081
CO_49	242.9300	21.9200	3.162 +/- 0.103	0.732	3.012	2.949 +/- 0.096
CO_50	242.7100	22.0000	1.851 +/- 0.082	0.827	3.123	1.949 +/- 0.086
CO_51	242.8800	22.0000	4.458 +/- 0.081	0.829	3.100	4.706 +/- 0.086
CO_52	242.6600	22.0800	6.670 +/- 0.077	0.705	2.840	5.988 +/- 0.069
CO_53	242.8300	22.0800	3.682 +/- 0.086	0.778	3.234	3.650 +/- 0.085
CO_54	242.6100	22.1700	6.700 +/- 0.099	0.681	2.970	5.813 +/- 0.086
CO_55	242.7700	22.1700	2.485 +/- 0.092	0.886	3.371	2.804 +/- 0.103
CO_56	242.8200	21.8300	1.494 +/- 0.077	0.721	3.321	1.372 +/- 0.071
CO_57	242.9900	21.8300	1.353 +/- 0.083	0.787	3.162	1.356 +/- 0.083
CO_58	242.4100	22.2100	1.543 +/- 0.096	0.841	2.825	1.652 +/- 0.102

continued on next page

Table 5.1 – continued from previous page

Position	RA(2000) (deg)	Dec(2000) (deg)	T_R^* (K)	Δv (km s ⁻¹)	v_{LSR} (km s ⁻¹)	$W(CO)^a$ (K km s ⁻¹)
CO_59	242.5000	22.2100	5.220 +/- 0.108	0.947	2.996	6.296 +/- 0.130
CO_60	243.0416	22.0000	0.640 +/- 0.088	0.580	3.062	0.473 +/- 0.065
CO_61	243.0416	22.0333	0.500 +/- 0.103	0.880	3.084	0.560 +/- 0.115
CO_62	243.0416	21.9666	0.715 +/- 0.098	0.821	2.999	0.748 +/- 0.103
CO_63	243.0750	22.0000				104 mK
CO_64	243.0083	22.0000	1.092 +/- 0.110	0.536	3.319	0.745 +/- 0.075
CO_65	243.1666	21.6333	0.372 +/- 0.103	0.454	0.116	0.215 +/- 0.059
CO_66	243.1666	21.6666	0.461 +/- 0.109	0.416	-0.036	0.244 +/- 0.058
CO_67	243.1666	21.6000	0.329 +/- 0.106	0.943	-0.056	0.395 +/- 0.127
CO_68	243.2000	21.6333				104 mK
CO_69	243.1333	21.6333	0.431 +/- 0.075	0.255	0.251	0.140 +/- 0.024
CO_70	242.9250	21.3333	0.685 +/- 0.091	0.427	3.000	0.373 +/- 0.049
CO_71	242.9250	21.3666				88 mK
CO_72	242.9250	21.3000				90 mK
CO_73	242.9583	21.3333				81 mK
CO_74	242.8916	21.3333	0.409 +/- 0.090	0.381	3.069	0.198 +/- 0.043
CO_75	242.2833	21.6916				63 mK
CO_76	242.2833	21.7250	0.312 +/- 0.070	1.200	3.252	0.476 +/- 0.107
CO_77	242.2833	21.6583				68 mK
CO_78	242.2500	21.6916	0.189 +/- 0.061	0.683	3.568	0.164 +/- 0.053
CO_79	242.3166	21.6916	0.270 +/- 0.069	0.340	4.169	0.117 +/- 0.030
CO_80	242.5916	21.1366	0.205 +/- 0.065	1.198	0.025	0.313 +/- 0.099
CO_81	242.5916	21.1700				64 mK
CO_82	242.5916	21.1033	0.321 +/- 0.071		0.001	0.364 +/- 0.0477
CO_83	242.5583	21.1366				66 mK
CO_84	242.6250	21.1366	0.115 +/- 0.063	0.918	4.347	0.134 +/- 0.073
CO_85	242.1833	21.1927				68 mK
CO_86	242.1833	21.2261				69 mK
CO_87	242.1833	21.1594	0.392 +/- 0.069	0.798	2.947	0.398 +/- 0.070
CO_88	242.1500	21.1927	0.166 +/- 0.054	1.010	4.504	0.213 +/- 0.069
CO_89	242.2166	21.1927				69 mK
CO_90	241.5791	20.8733	2.901 +/- 0.107	0.510	3.489	1.883 +/- 0.069

continued on next page

Table 5.1 – continued from previous page

Position	RA(2000) (deg)	Dec(2000) (deg)	T_R^* (K)	Δv (km s ⁻¹)	v_{LSR} (km s ⁻¹)	W(CO) ^a (K km s ⁻¹)
CO_91	241.5791	20.9066	2.844 +/- 0.113	0.599	3.446	2.172 +/- 0.086
CO_92	242.6333	22.4100	1.367 +/- 0.071	0.685	3.488	1.192 +/- 0.062
CO_93	242.6333	22.4433	0.931 +/- 0.067	0.627	3.524	0.744 +/- 0.053
CO_94	242.6333	21.3750				75 mK
CO_95	242.6000	22.4100	1.847 +/- 0.062	0.764	3.430	1.798 +/- 0.060
CO_96	242.6666	22.4100	0.878 +/- 0.089	0.713	3.488	0.797 +/- 0.081
CO_97	242.5375	22.5133	0.250 +/- 0.077	0.810	3.677	0.258 +/- 0.080
CO_98	242.5375	22.5466				66 mK
CO_99	242.5375	22.4800	2.294 +/- 0.073	0.642	3.699	1.877 +/- 0.060
CO_100	242.5041	22.5133	0.274 +/- 0.074	0.576	3.635	0.201 +/- 0.054
CO_101	242.5708	22.5133	0.417 +/- 0.076	0.661	4.027	0.351 +/- 0.064
CO_102	243.6916	22.3000	0.184 +/- 0.041	1.979	-2.170	0.463 +/- 0.103
CO_103	243.4041	21.6850	0.606 +/- 0.048	1.099	1.886	0.848 +/- 0.068

^a W(CO) is $\int T_{mb} dv$.

5.4 Results

Although the purpose of this observing run was not to map MBM40, the well-known structures of the cloud (a principle ridge running north-west to south-east) a smaller ridge to the west and an extended CO-intensity envelope surrounding the cloud are evident from our data. Quantitatively, our results are similar to the CO map of the main two ridges made with the FCRAO 14 m telescope and described by Shore et al. (2003) and Chastain (2005). In addition to mapping along the ridges, eight 5-point crosses were made in the envelope region of MBM40 (see Figure 5.2). Although the resolution of the CO observations (1') is a factor of six smaller than that of the Schegel, Finkbeiner, and Davis (1998) color-excess maps, the 5-point crosses have 2' spacing and thus, when averaged to produce one spectrum can be

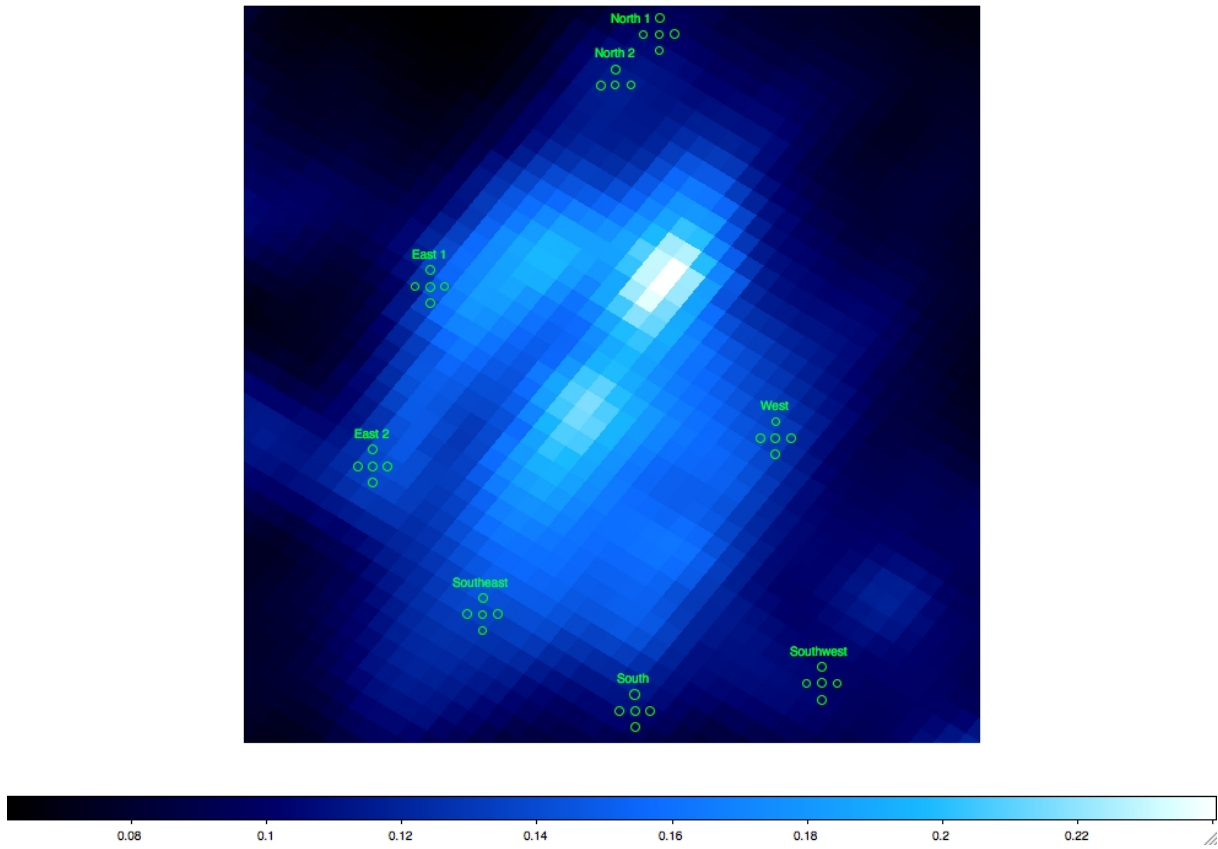


Figure 5.2: Positions of the eight 5-point crosses in the envelope of MBM40, where the y axis is declination, increasing traveling up the page and the x axis is right ascension, decreasing traveling to the right. These crosses lie in the envelope and outer regions of the cloud. The color represents $E(B-V)$ in magnitudes from the SFD dust maps.

Label (position on Table 5.1)	W(CO) (K km s ⁻¹)	E(B-V) (mag)
North 1 (97, 98, 99, 100, 101)	0.551 +/- 0.030	0.101
North 2 (92, 93, 95, 96)	1.133 +/- 0.047	0.115
East 1 (60, 61, 62, 63, 64)	0.526 +/- 0.071	0.137
East 2 (65, 66, 67, 68, 69)	0.220 +/- 0.055	0.136
Southeast (70, 71, 72, 73, 74)	0.166 +/- 0.047	0.136
South (80, 81, 82, 83, 84)	0.188 +/- 0.038	0.104
Southwest (85, 86, 87, 88, 89)	0.164 +/- 0.054	0.102
West (75, 76, 77, 78, 79)	0.178 +/- 0.052	0.133

Table 5.2: Averaged values of W(CO) and E(B-V) for the eight 5-point crosses in the envelope of MBM40.

reasonably compared to the E(B-V) values. This is done in Table 5.2 and a plot of the data is shown in Figure 5.3. A correlation between W(CO) and E(B-V) is often assumed, but Figure 5.3 shows that, at lower values of E(B-V), this relationship can break down because the CO line intensity fluctuates strongly at low N(H₂) levels. This type of behavior was also noted for MBM16 by Magnani et al. (2003).

5.5 X_{CO} in MBM40

To obtain values for X_{CO}, the CH method as described in Chapter 4 was implemented, where N(H₂) was calculated from N(CH). Using the CO(1-0) data from this work in tandem with CH data from Chastain et al. (2010), we calculated X_{CO}. Table 5.1 shows the positions observed in CO along with the W(CO) data obtained. Many of the data points chosen for this work coincide with data points from the CH observations made by Chastain et al.(2010), therefore N(H₂) and W(CO) can be computed for these positions. These results are shown in Table 5.3 along with the derived values for X_{CO}. A linear relationship between N(CH)

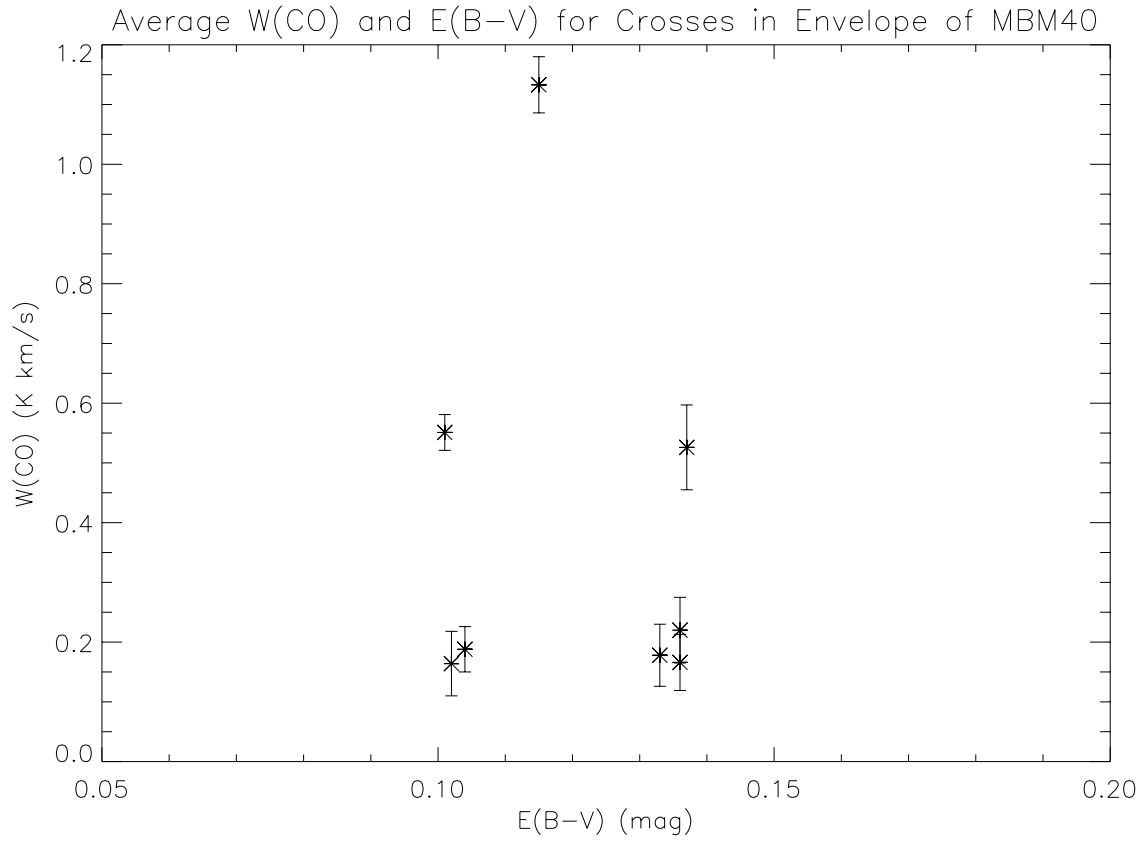


Figure 5.3: $W(\text{CO})$ versus $E(\text{B-V})$ for the eight 5-point crosses in the envelope of MBM40 (see Table 5.2).

and $N(\text{H}_2)$ has been found empirically by Federman (1982), Danks, Federman, & Lambert (1984), Mattila (1986), and Liszt & Lucas (2002). As described in Section 4.2, we use the relationship obtained by Mattila (1986).

We divided MBM40 into three regions based on $E(\text{B-V})$. The three regions are defined as: the “core” region where $E(\text{B-V}) > 0.17$, the “envelope” region where $0.12 \leq E(\text{B-V}) \leq 0.17$, and the “outermost” region where $E(\text{B-V}) < 0.12$ mag. 44 data points from the CO data are located within the core, and for 32 of these CO data points we have CH data. After obtaining $N(\text{H}_2)$ from $N(\text{CH})$, we divided the former quantities by $W(\text{CO})$ to get X_{CO} . Our values of X_{CO} range from 0.8 to $3.6 \times 10^{20} \text{ cm}^{-2}(\text{K km s}^{-1})^{-1}$ (the units of X_{CO} will be with held for the rest of the chapter) with an average value of $1.5 \pm 0.32 \times 10^{20}$ within the core. 38 of the CO data points, four of which are correlated with CH data, are located within the envelope. These X_{CO} values range from 0.9 to 3.5×10^{20} with an average value of $1.9 \pm 0.58 \times 10^{20}$. The other CO positions lie in the outer regions and have no CH data taken by Chastain (2005); therefore, X_{CO} could not be calculated for those positions. The values for X_{CO} are consistent with the median value of 1.2×10^{20} found by Magnani & Onello (1995) for twelve different translucent clouds (Magnani and Onello 1995). Chastain (2005) obtained a median value of $X_{\text{CO}} = 2.9 \times 10^{20}$ using the FCRAO 14 m telescope, primarily observing CO within the core for MBM40.

Table 5.3: Determination of X_{CO} from CH in MBM40.

Position	$N(\text{CH})^a$ $\times 10^{13} \text{ cm}^{-2}$	$N(\text{H}_2)^b$ $\times 10^{20} \text{ cm}^{-2}$	X_{CO} $\times 10^{20} \text{ cm}^{-2}(\text{K km s}^{-1})^{-1}$
MBM40_2	2.6 +/- 0.77	0.76 +/- 0.22	3.57 +/- 1.08
MBM40_3	3.5 +/- 0.79	0.95 +/- 0.21	3.56 +/- 0.82
MBM40_4	2.9 +/- 0.45	0.84 +/- 0.13	2.06 +/- 0.33
MBM40_5	1.6 +/- 0.54	0.56 +/- 0.19	2.15 +/- 0.74
MBM40_6	2.9 +/- 0.68	0.84 +/- 0.20	1.88 +/- 0.45
MBM40_7	3.5 +/- 0.45	0.95 +/- 0.12	1.23 +/- 0.16
MBM40_8	3.7 +/- 0.73	0.99 +/- 0.19	1.60 +/- 0.32

continued on next page

Table 5.3 – continued from previous page

Position	N(CH) ^a x10 ¹³ cm ⁻²	N(H ₂) ^b x10 ²⁰ cm ⁻²	X _{CO} x10 ²⁰ cm ⁻² (K km s ⁻¹) ⁻¹
MBM40_18	4.1 +/- 0.57	1.08 +/- 0.15	1.51 +/- 0.21
MBM40_19	3.9 +/- 0.45	1.04 +/- 0.12	1.01 +/- 0.12
MBM40_21	2.9 +/- 0.52	0.83 +/- 0.15	0.96 +/- 0.17
MBM40_22	3.5 +/- 0.21	0.95 +/- 0.06	1.01 +/- 0.06
MBM40_24	2.3 +/- 0.52	0.71 +/- 0.16	1.10 +/- 0.25
MBM40_25	1.6 +/- 0.47	0.56 +/- 0.16	0.93 +/- 0.27
MBM40_27	2.4 +/- 0.46	0.72 +/- 0.14	1.26 +/- 0.24
MBM40_28	1.7 +/- 0.51	0.59 +/- 0.18	0.97 +/- 0.29
MBM40_30	3.8 +/- 0.39	1.01 +/- 0.10	1.29 +/- 0.13
MBM40_31	1.9 +/- 0.44	0.61 +/- 0.14	1.06 +/- 0.25
MBM40_33	4.2 +/- 0.58	1.10 +/- 0.15	1.32 +/- 0.18
MBM40_34	2.1 +/- 0.53	0.66 +/- 0.17	1.02 +/- 0.26
MBM40_36	3.4 +/- 0.48	0.93 +/- 0.13	1.25 +/- 0.18
MBM40_37	3.1 +/- 0.53	0.86 +/- 0.15	1.10 +/- 0.19
MBM40_38	3.2 +/- 0.73	0.88 +/- 0.20	1.89 +/- 0.43
MBM40_39	2.9 +/- 0.48	0.82 +/- 0.14	0.91 +/- 0.15
MBM40_40	2.0 +/- 0.47	0.65 +/- 0.15	1.05 +/- 0.25
MBM40_42	2.8 +/- 0.47	0.82 +/- 0.14	1.07 +/- 0.18
MBM40_43	1.7 +/- 0.44	0.57 +/- 0.15	0.83 +/- 0.21
MBM40_44	2.7 +/- 0.58	0.78 +/- 0.17	2.25 +/- 0.48
MBM40_45	1.9 +/- 0.42	0.63 +/- 0.14	0.93 +/- 0.21
MBM40_47	2.7 +/- 0.70	0.78 +/- 0.20	1.74 +/- 0.46
MBM40_48	1.2 +/- 0.37	0.48 +/- 0.15	2.03 +/- 0.63
MBM40_49	2.0 +/- 0.48	0.64 +/- 0.15	2.17 +/- 0.52
MBM40_51	2.4 +/- 0.61	0.73 +/- 0.19	1.55 +/- 0.40
MBM40_52	1.7 +/- 0.34	0.58 +/- 0.11	0.97 +/- 0.19
MBM40_54	1.9 +/- 0.56	0.63 +/- 0.19	1.08 +/- 0.32
MBM40_57	1.2 +/- 0.39	0.47 +/- 0.15	3.47 +/- 1.15
MBM40_59	1.7 +/- 0.43	0.58 +/- 0.15	0.92 +/- 0.23

^a Data from Chastain 2005.^b Calculated from Equation 4.2.

5.5.1 Comparison to previous results

Previously, Magnani et al. (1998) found that X_{CO} and $W(\text{CO})$ may follow an inverse relationship in translucent clouds. This can be interpreted as a change in the CO - H₂ ratio at the lowest column densities of H₂ (Magnani et al. 1998). In Figure 4 of Magnani et al. (1998) the possible inverse power law relation of $X_{\text{CO}} = W(\text{CO})^{-1}$ was first noted. They were able to show that for 19 translucent clouds, which included MBM40, that X_{CO} and $W(\text{CO})$ seemed to behave in this inverse manner. Although there are only four points for the envelope, a curve was fit to those data revealing that both the core and envelope may obey this inverse relation, but with different fit coefficients (see Figure 5.4).

5.5.2 Analysis

From Figure 5.4 it can be seen that in areas with high $W(\text{CO})$ ($\approx 10 \text{ K km s}^{-1}$ or greater), X_{CO} remains constant even as $W(\text{CO})$ increases. This non varying nature of X_{CO} can be explained by the fact that at large extinction values the optical thickness of the CO(1-0) line causes a saturation of the line. At these large extinctions hydrogen is already primarily in molecular form but CO is just becoming the dominant carbon containing species (Sonnentrucker et al. 2007), therefore more CO emission is occurring while the amount of N(H₂) remains fairly constant. The other extreme of the graph, the low $W(\text{CO})$ section, is the section that most resembles the envelope and outer regions of MBM40. The curve fit in this section shows that X_{CO} increases asymptotically towards low $W(\text{CO})$ values near 1 K km/s. Lower values of $W(\text{CO})$ are characteristic of diffuse regions, $A_V \leq 1$, where photo processes play a dominant role. In this region, CO is being photodissociated more strongly than H₂. Since most carbon is in the form of C⁺ and C in the diffuse region, and most of the hydrogen is in molecular form, the X_{CO} value increases as $W(\text{CO})$ decreases (Van Dishoeck and Black 1988).

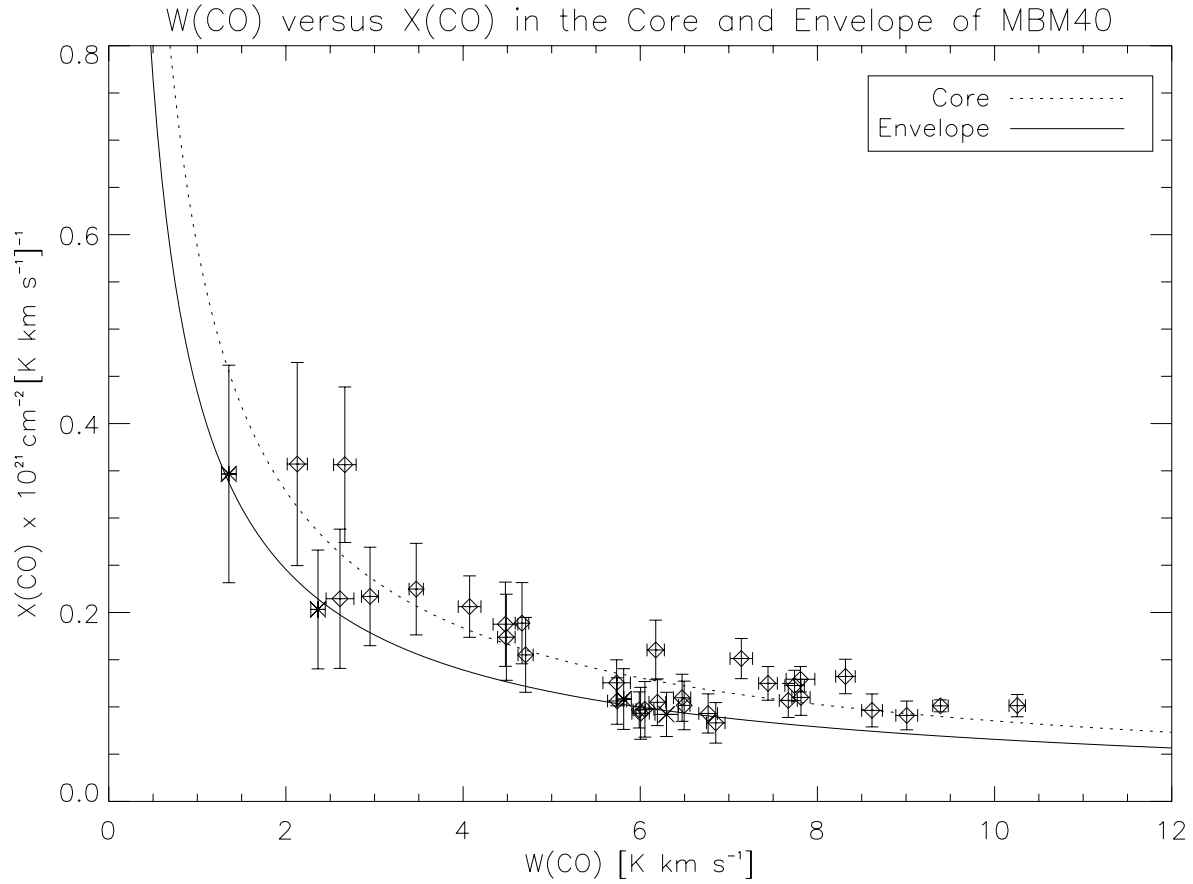


Figure 5.4: X_{CO} versus $W(\text{CO})$ for the envelope and the core of MBM40. The envelope consists of four points and are labeled with *. The curve fit for the core is of the form $X_{\text{CO}} = 5.9 \times 10^{20} [W(\text{CO})^{-0.838}]$ (with an R squared value of 0.74) and for the envelope it is of the form $X_{\text{CO}} = 4.3 \times 10^{20} [W(\text{CO})^{-0.819}]$ (with an R squared value of 0.99)

5.6 Conclusion

The combination of the new CO data that we obtained from the ARO 12 m telescope with previous CH observations allowed us to derive values of X_{CO} in the envelope of MBM40. Figure 5.4 shows how the relationship between $W(\text{CO})$ and X_{CO} varies as a function of $W(\text{CO})$ and that there is a transition region from low to high values of $W(\text{CO})$. Based on these data, a value of $1.5 \pm 0.32 \times 10^{20} [\text{K km s}^{-1}]^{-1}$ for X_{CO} will be used to calculate H_2 in the core regions, while in the envelope region, an average X_{CO} value of $1.9 \pm 0.58 \times 10^{20} [\text{K km s}^{-1}]^{-1}$ is used to determine H_2 , and a value of $2.0 \times 10^{20} [\text{K km s}^{-1}]^{-1}$ is used in the outermost regions of MBM40. We were also able to confirm that X_{CO} varies inversely with $W(\text{CO})$ as had been seen in earlier studies.

Chapter 6

The Outer Envelope of MBM 40; CO Data

6.1 Introduction

The interior core region of MBM40 has been studied before by Chastain et al. (2010) using CH and CO observations. That survey also covered the envelope region of MBM40 but the integration times used for the observations of this cloud did not yield many detections. In this work we observed the envelope regions of MBM40 at longer integrations times, up to 20 minutes, using the CO(1-0) transition (normal CO integrations are typically a few minutes each). Observations were also made in eight cross regions within the envelope of MBM40 (see Figure 5.1).

Traditionally, observations of the CO(1-0) line have been used to determine the physical properties of molecular clouds. The conversion from CO observations to the mass in molecular hydrogen is not straightforward for translucent molecular clouds. Recently, the ability of the CO(1-0) transition to trace H₂ in all types of clouds has been called into question by Grenier, Casandjian, and Terrier (2005). They suggest that the amount of molecular gas

that has been detected by the CO Galactic surveys is equal to the amount present in dark form, i.e., not detectable by conventional radio spectroscopy. Because of the destruction mechanisms for CO, it is possible that a regime of molecular gas exists where the CO does not effectively trace the molecular hydrogen content of clouds (e.g., van Dishoeck and Black 1988). Moreover, if the molecular gas is very cold, CO(1-0) detection would be difficult. In an effort to explore this issue, we conducted high-sensitivity observations of OH (see Chapter 7) and CO in the envelope region of the translucent molecular cloud, MBM 40. The main lines at 1665 and 1667 MHz of OH and the CO(1-0) line are well-known tracers of low-density molecular gas (Wouterloot 1981). By using these observations to estimate the mass in the envelope and outermost environs of MBM 40 (as traced by dust emission), we can compare how much mass is tied up in regions that are normally not well-traced by traditional, short integration time CO(1-0) observations.

6.2 Past Studies

As is clear from figure taken from Chastain (2005) (Figure 6.1), there is significant dust emission beyond the lowest CO contour in MBM40. Deeper CO integrations reveal CO(1-0) emission in the envelope region immediately surrounding the core that Chastain mapped in CO(1-0). However, to detect CO emission in regions where $E(B-V) \leq 0.12$ mag, integration times of more than 15 minutes are required.

Chastain's (2005) CO observations covered a 0.78 degree by 0.98 degree grid covering the core region of MBM40. Using a ratio of detections to non detections from the entire 0.76 square degree region of the cloud where observations were made, he obtained a value for the molecular mass contained within a 0.3 square degree area of MBM40. Using a distance estimate of 80 pc, and an X_{CO} value of $2.2 \times 10^{20} \text{ cm}^{-2} [\text{K km s}^{-1}]^{-1}$ he determined the molecular mass of MBM40's core to be $\sim 15 M_{\odot}$.

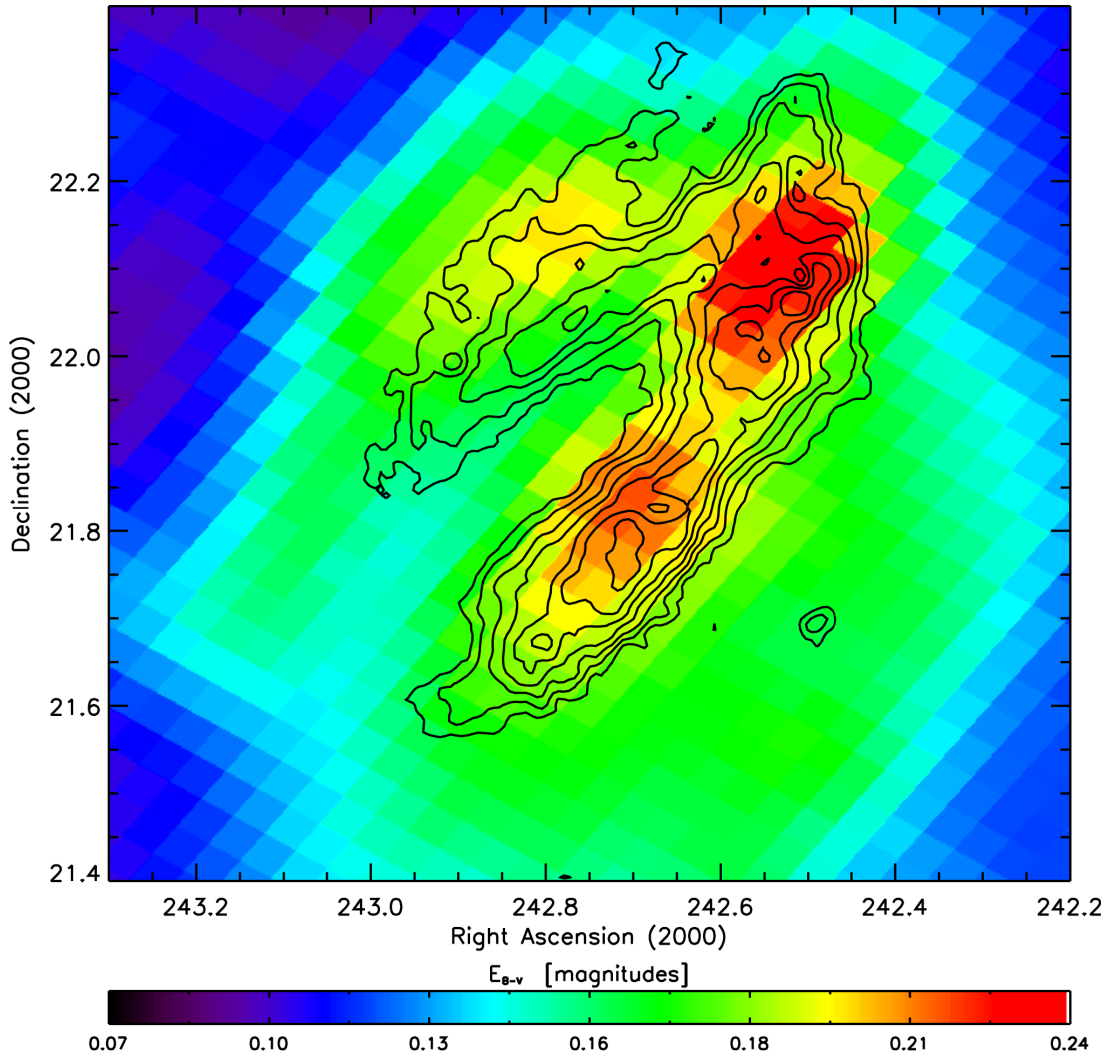


Figure 6.1: Contours obtained from Chastain (2005) of the velocity-integrated CO(1-0) map overplotted on the dust map of MBM40 from the SFD dataset. The $W(\text{CO})$ contour levels are 0.88, 1.75, 2.63, 3.51, 4.38, 5.26, and 6.14 K km/s.

6.3 Comparison of Our CO Observations with those of Chastain (2005)

Using Chastain’s CO and CH observations as a guide we observed the core regions of MBM40 in CO but we also extended our observations (described in Chapter 5) to the envelope region and even further out to the “outermost” regions of MBM40 where E(B-V) values are less than 0.12 mag (see Figure 6.2). In this study all 44 observations within the core region yielded detections, with an average W(CO) value of 5.02 ± 0.11 [K km s⁻¹] and an average E(B-V) of 0.19 mag. Chastain reports CH data for 32 of these 44 locations, allowing us to obtain X_{CO} values for these 32 locations. The X_{CO} values allow us to check our extrapolation method where only W(CO) and E(B-V) are used to determine N(H₂). Looking to regions of lower E(B-V), we detected CO in 31 of 38 locations in the envelope and 14 of 21 in the outermost regions resulting in average W(CO) values of 1.26 ± 0.083 and 0.678 ± 0.067 [K km s⁻¹], respectively. Chastain only had 4 detections in the envelope region and none in the outermost region.

6.3.1 Determining CO Mass from CO(1-0) Emission

In Table 5.1 all 103 data points are tabulated along with their measured W(CO) values, or upper limits, but we also need the column density, N(CO). To calculate the column density in terms of observables, we must first find the absorption coefficient, κ_ν in terms of the full width at half max, $\Delta\nu_L$. The absorption coefficient is derived from basic radiative transfer equations and can be written as:

$$\kappa_\nu = \frac{c^2 A_{ul} n_l}{8\pi^{\frac{1}{2}} \nu^2} \frac{g_u}{g_l} [1 - e^{\frac{-h\nu}{kT_{\text{ex}}}}] (2\ln 2)^{1/2} \Delta\nu_L^{-1} \quad (6.1)$$

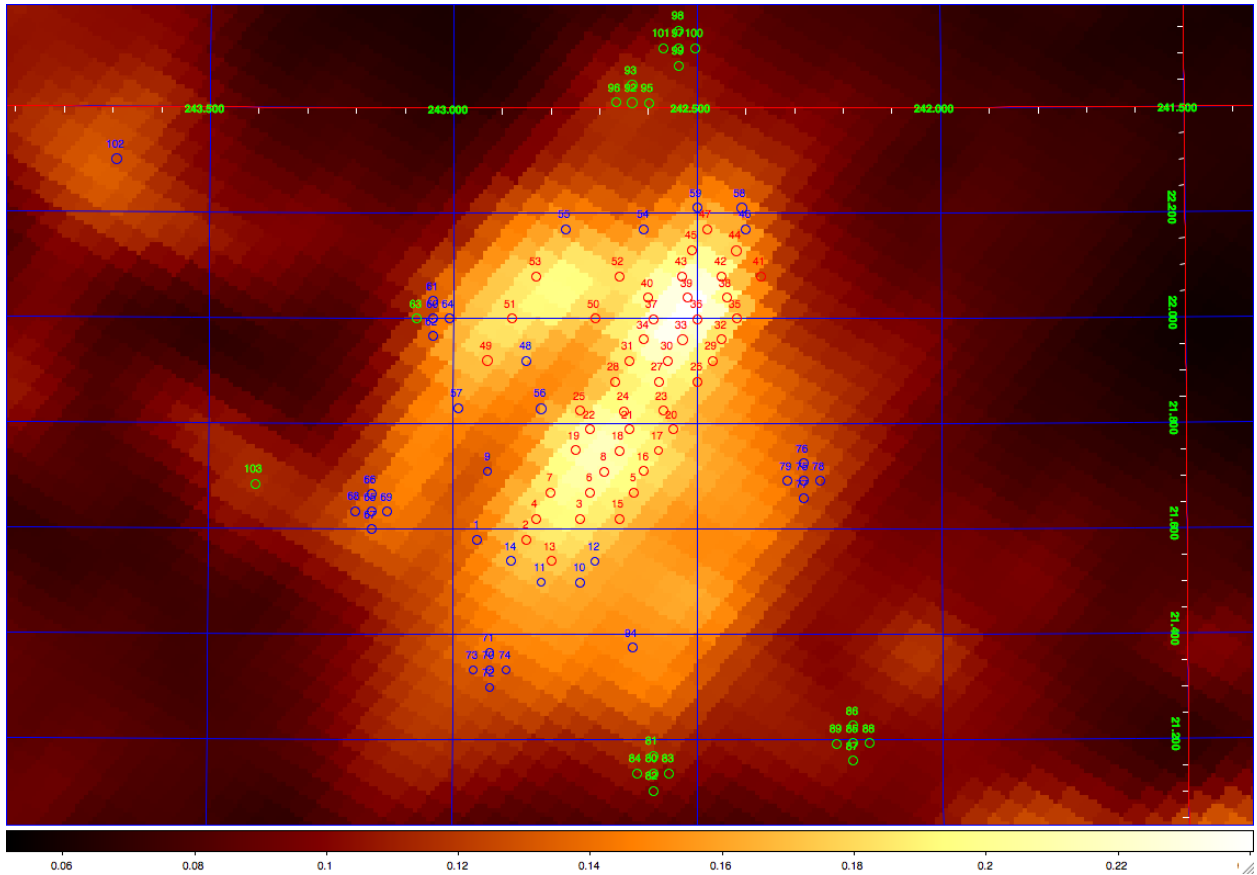


Figure 6.2: Positions of CO(1-0) observations for MBM40. Colors of the circles represent the region where each data point lies: red for the core region, blue for the envelope region, and green for the outermost region. Observations of MBM40 are over plotted on the dust map from the SFD dataset.

where u and l represent the upper and lower states of the given transition, A_{ul} is the Einstein A coefficient ($7.21 \times 10^{-8} \text{ s}^{-1}$ for the 115 GHz transition), and g is the statistical weight of the given state. Optical depth is related to the absorption coefficient by:

$$\tau_\nu = \kappa_\nu L \text{ (cm)} \quad (6.2)$$

where L is the path length through the cloud. By combining Equations 6.1 and 6.2 we can find the column density, $N=nL$. Relating the antenna temperature T_A with τ_ν :

$$T_A = (T_{\text{ex}} - T_{\text{BG}})\tau_\nu \text{ (K)} \quad (6.3)$$

where T_{BG} is the background temperature, 2.73 K, and T_{ex} is the excitation temperature of the transition, which we estimated to be 10, 20 and 40 K, (based on the average temperature range of MBM40, 10 - 40 K). Plugging Equation 6.3 into Equation 6.2 and recognizing that $T_A \Delta\nu$ is the integrated line width, $W(\text{CO})$, yields Equation 6.4 which will be used throughout this thesis to find column densities that depend on excitation temperature and integrated line widths.

$$N_u = (g_l/g_u)(1/A_{ul})(1/\lambda^3)(8\pi^{1/2}/(2\ln 2)^{1/2})[1 - e^{-h\nu/kT_{\text{ex}}}]^{-1}(T_{\text{ex}} - T_{\text{BG}})^{-1}W(\text{CO}) \text{ (cm}^{-2}\text{)} \quad (6.4)$$

Where g is the statistical weights for the upper (u) and lower (l) states. A is the associated Einstein A coefficients for the given transition with λ being the wavelength of the transition in question. Of course, the principal assumptions for this equation to give a reasonable values of $N(\text{CO})$ are that almost all the molecules are in the $J = 1$ rotational state and that the transition is optically thin. The first condition is reasonable in the sense that most of the CO molecules are likely to be in the 3 lowest rotational states so that the values of $N(\text{CO})$

obtained are likely to be within a factor of a few of the actual values. The second condition may only be valid in the envelope or outermost regions. Thus, in the core, we will only have a lower limit estimate to $N(\text{CO})$. Once $N(\text{CO})$ is calculated we can estimate the mass using

$$\text{Mass}(\text{CO}) = N(\text{CO})\Omega d^2 (M_{\odot}) \quad (6.5)$$

where Ω is the solid angle covered by the region in question and d is the distance to the cloud. Using the column densities, which are listed in Table 6.1, a cloud distance of 140 pc, and Equation 6.5, mass estimates for the different regions can be found for each excitation temperature, with the results listed in Table 6.2.

Table 6.1: $N(\text{CO}) \times 10^{14} \text{ cm}^{-2}$ for the observed CO positions in MBM40.

Position	RA(2000) (deg)	Dec(2000) (deg)	N(CO)		
			$T_{\text{ex}} = 10 \text{ K}$	$T_{\text{ex}} = 20 \text{ K}$	$T_{\text{ex}} = 40 \text{ K}$
CO_1	242.95	21.58	6.370 +/- 0.415	4.716 +/- 0.307	4.089 +/- 0.266
CO_2	242.85	21.58	6.819 +/- 0.365	5.049 +/- 0.270	4.378 +/- 0.234
CO_3	242.74	21.62	8.542 +/- 0.409	6.324 +/- 0.303	5.483 +/- 0.263
CO_4	242.83	21.62	13.05 +/- 0.411	9.666 +/- 0.304	8.381 +/- 0.264
CO_5	242.63	21.67	8.365 +/- 0.504	6.194 +/- 0.373	5.370 +/- 0.324
CO_6	242.72	21.67	14.35 +/- 0.448	10.62 +/- 0.332	9.214 +/- 0.288
CO_7	242.80	21.67	24.81 +/- 0.353	18.37 +/- 0.261	15.92 +/- 0.226
CO_8	242.69	21.71	19.78 +/- 0.314	14.65 +/- 0.232	12.70 +/- 0.201
CO_9	242.92	21.71	4.117 +/- 0.414	3.048 +/- 0.306	2.643 +/- 0.265
CO_10	242.74	21.50	0.781 +/- 0.312	0.578 +/- 0.231	0.501 +/- 0.200
CO_11	242.82	21.50	0.332 +/- 0.073	0.246 +/- 0.054	0.213 +/- 0.047
CO_12	242.71	21.54	1.790 +/- 0.202	1.325 +/- 0.150	1.149 +/- 0.130
CO_13	242.80	21.54	5.647 +/- 0.576	4.181 +/- 0.427	3.625 +/- 0.370
CO_14	242.88	21.54	4.526 +/- 0.354	3.351 +/- 0.262	2.906 +/- 0.227
CO_15	242.66	21.62	3.082 +/- 0.279	2.282 +/- 0.206	1.979 +/- 0.179
CO_16	242.61	21.71	6.277 +/- 0.370	4.648 +/- 0.274	4.030 +/- 0.238
CO_17	242.58	21.75	5.947 +/- 0.420	4.403 +/- 0.311	3.818 +/- 0.270
CO_18	242.66	21.75	22.88 +/- 0.407	16.94 +/- 0.301	14.69 +/- 0.261
CO_19	242.75	21.75	32.86 +/- 0.296	24.33 +/- 0.219	21.09 +/- 0.190
CO_20	242.55	21.79	5.760 +/- 0.693	4.265 +/- 0.513	3.698 +/- 0.445
CO_21	242.64	21.79	27.61 +/- 0.377	20.44 +/- 0.279	17.72 +/- 0.242

continued on next page

Table 6.1 – continued from previous page

Position	RA(2000)	Dec(2000)	N(CO)		N(CO)
	(deg)	(deg)	$T_{\text{ex}} = 10 \text{ K}$	$T_{\text{ex}} = 20 \text{ K}$	$T_{\text{ex}} = 40 \text{ K}$
CO_22	242.72	21.79	30.09 +/- 0.279	22.27 +/- 0.207	19.31 +/- 0.179
CO_23	242.57	21.82	7.201 +/- 0.330	5.332 +/- 0.244	4.623 +/- 0.212
CO_24	242.65	21.82	20.74 +/- 0.312	15.35 +/- 0.231	13.31 +/- 0.201
CO_25	242.74	21.82	19.24 +/- 0.316	14.24 +/- 0.234	12.35 +/- 0.203
CO_26	242.50	21.88	4.834 +/- 0.299	3.579 +/- 0.221	3.103 +/- 0.192
CO_27	242.58	21.88	18.37 +/- 0.498	13.60 +/- 0.369	11.79 +/- 0.320
CO_28	242.67	21.88	19.39 +/- 0.325	14.36 +/- 0.240	12.45 +/- 0.209
CO_29	242.47	21.92	5.885 +/- 0.401	4.357 +/- 0.297	3.778 +/- 0.258
CO_30	242.56	21.92	25.02 +/- 0.519	18.53 +/- 0.384	16.06 +/- 0.333
CO_31	242.64	21.92	18.39 +/- 0.347	13.61 +/- 0.257	11.80 +/- 0.223
CO_32	242.45	21.96	7.288 +/- 0.294	5.396 +/- 0.218	4.678 +/- 0.189
CO_33	242.53	21.96	26.65 +/- 0.353	19.73 +/- 0.262	17.11 +/- 0.227
CO_34	242.61	21.96	20.81 +/- 0.209	15.41 +/- 0.155	13.36 +/- 0.134
CO_35	242.42	22.00	10.37 +/- 0.322	7.684 +/- 0.238	6.662 +/- 0.207
CO_36	242.50	22.00	23.85 +/- 0.338	17.65 +/- 0.250	15.31 +/- 0.217
CO_37	242.59	22.00	25.04 +/- 0.330	18.54 +/- 0.244	16.07 +/- 0.212
CO_38	242.44	22.04	14.95 +/- 0.245	11.06 +/- 0.181	9.597 +/- 0.157
CO_39	242.52	22.04	28.87 +/- 0.395	21.37 +/- 0.292	18.53 +/- 0.253
CO_40	242.60	22.04	19.84 +/- 0.303	14.69 +/- 0.225	12.74 +/- 0.195
CO_41	242.37	22.08	2.901 +/- 0.346	2.148 +/- 0.256	1.862 +/- 0.222
CO_42	242.45	22.08	24.58 +/- 0.325	18.20 +/- 0.241	15.78 +/- 0.209
CO_43	242.53	22.08	21.96 +/- 0.335	16.26 +/- 0.248	14.09 +/- 0.215
CO_44	242.42	22.13	11.12 +/- 0.258	8.235 +/- 0.191	7.140 +/- 0.166
CO_45	242.51	22.13	21.68 +/- 0.339	16.05 +/- 0.251	13.92 +/- 0.218
CO_46	242.40	22.17	4.924 +/- 0.277	3.645 +/- 0.205	3.161 +/- 0.178
CO_47	242.48	22.17	14.38 +/- 0.317	10.65 +/- 0.234	9.235 +/- 0.203
CO_48	242.85	21.92	7.570 +/- 0.261	5.605 +/- 0.193	4.860 +/- 0.167
CO_49	242.93	21.92	9.452 +/- 0.308	6.998 +/- 0.228	6.068 +/- 0.197
CO_50	242.71	22.00	6.247 +/- 0.276	4.625 +/- 0.204	4.010 +/- 0.177
CO_51	242.88	22.00	15.08 +/- 0.274	11.16 +/- 0.203	9.681 +/- 0.176
CO_52	242.66	22.08	19.19 +/- 0.220	14.21 +/- 0.163	12.32 +/- 0.141
CO_53	242.83	22.08	11.69 +/- 0.274	8.661 +/- 0.203	7.509 +/- 0.176
CO_54	242.61	22.17	18.63 +/- 0.275	13.79 +/- 0.204	11.96 +/- 0.177
CO_55	242.77	22.17	8.987 +/- 0.331	6.654 +/- 0.245	5.769 +/- 0.212
CO_56	242.82	21.83	4.397 +/- 0.227	3.255 +/- 0.168	2.823 +/- 0.146
CO_57	242.99	21.83	4.345 +/- 0.267	3.217 +/- 0.197	2.790 +/- 0.171
CO_58	242.41	22.21	5.296 +/- 0.328	3.921 +/- 0.243	3.400 +/- 0.211
CO_59	242.50	22.21	20.17 +/- 0.418	14.94 +/- 0.309	12.95 +/- 0.268

continued on next page

Table 6.1 – continued from previous page

Position	RA(2000)	Dec(2000)	N(CO)		N(CO)
	(deg)	(deg)	$T_{\text{ex}} = 10 \text{ K}$	$T_{\text{ex}} = 20 \text{ K}$	$T_{\text{ex}} = 40 \text{ K}$
CO_60	243.04	22.00	1.516 +/- 0.207	1.122 +/- 0.153	0.973 +/- 0.133
CO_61	243.04	22.03	1.796 +/- 0.369	1.329 +/- 0.273	1.153 +/- 0.237
CO_62	243.04	21.96	2.397 +/- 0.329	1.775 +/- 0.243	1.539 +/- 0.211
CO_63	243.07	22.00	0	0	0
CO_64	243.00	22.00	2.387 +/- 0.240	1.768 +/- 0.178	1.533 +/- 0.154
CO_65	243.16	21.63	0.689 +/- 0.190	0.510 +/- 0.141	0.442 +/- 0.122
CO_66	243.16	21.66	0.783 +/- 0.185	0.579 +/- 0.137	0.502 +/- 0.119
CO_67	243.16	21.60	1.265 +/- 0.408	0.937 +/- 0.302	0.812 +/- 0.262
CO_68	243.20	21.63	0	0	0
CO_69	243.13	21.63	0.448 +/- 0.078	0.332 +/- 0.057	0.288 +/- 0.050
CO_70	242.92	21.33	1.194 +/- 0.158	0.884 +/- 0.117	0.767 +/- 0.101
CO_71	242.92	21.36	0	0	0
CO_72	242.92	21.30	0	0	0
CO_73	242.95	21.33	0	0	0
CO_74	242.89	21.33	0.635 +/- 0.139	0.470 +/- 0.103	0.407 +/- 0.089
CO_75	242.28	21.69	0	0	0
CO_76	242.28	21.72	1.527 +/- 0.344	1.130 +/- 0.255	0.980 +/- 0.221
CO_77	242.28	21.65	0	0	0
CO_78	242.25	21.69	0.527 +/- 0.169	0.390 +/- 0.125	0.338 +/- 0.108
CO_79	242.31	21.69	0.375 +/- 0.095	0.277 +/- 0.070	0.241 +/- 0.061
CO_80	242.59	21.13	1.004 +/- 0.317	0.743 +/- 0.235	0.644 +/- 0.204
CO_81	242.59	21.17	0	0	0
CO_82	242.59	21.10	1.167 +/- 0.151	0.864 +/- 0.112	0.749 +/- 0.097
CO_83	242.55	21.13	0	0	0
CO_84	242.62	21.13	0.429 +/- 0.235	0.318 +/- 0.174	0.276 +/- 0.151
CO_85	242.18	21.19	0	0	0
CO_86	242.18	21.22	0	0	0
CO_87	242.18	21.15	1.276 +/- 0.225	0.945 +/- 0.167	0.819 +/- 0.144
CO_88	242.15	21.19	0.682 +/- 0.222	0.505 +/- 0.164	0.438 +/- 0.143
CO_89	242.21	21.19	0	0	0
CO_90	241.57	20.87	6.034 +/- 0.222	4.468 +/- 0.164	3.874 +/- 0.142
CO_91	241.57	20.90	6.960 +/- 0.277	5.153 +/- 0.205	4.468 +/- 0.178
CO_92	242.63	22.41	3.820 +/- 0.198	2.829 +/- 0.146	2.453 +/- 0.127
CO_93	242.63	22.44	2.384 +/- 0.171	1.765 +/- 0.127	1.530 +/- 0.110
CO_94	242.63	21.37	0	0	0
CO_95	242.60	22.41	5.763 +/- 0.194	4.267 +/- 0.143	3.699 +/- 0.124
CO_96	242.66	22.41	2.555 +/- 0.260	1.891 +/- 0.192	1.640 +/- 0.167
CO_97	242.53	22.51	0.826 +/- 0.256	0.612 +/- 0.189	0.530 +/- 0.164

continued on next page

Table 6.1 – continued from previous page

Position	RA(2000)	Dec(2000)	N(CO)		N(CO)
	(deg)	(deg)	$T_{\text{ex}} = 10 \text{ K}$	$T_{\text{ex}} = 20 \text{ K}$	$T_{\text{ex}} = 40 \text{ K}$
CO_98	242.53	22.54	0	0	0
CO_99	242.53	22.48	6.015 +/- 0.191	4.454 +/- 0.141	3.861 +/- 0.123
CO_100	242.50	22.51	0.644 +/- 0.173	0.477 +/- 0.128	0.413 +/- 0.111
CO_101	242.57	22.51	1.125 +/- 0.205	0.833 +/- 0.152	0.722 +/- 0.132
CO_102	243.69	22.30	1.485 +/- 0.330	1.099 +/- 0.244	0.953 +/- 0.212
CO_103	243.40	21.68	2.717 +/- 0.217	2.012 +/- 0.161	1.744 +/- 0.139

Zeroes represent non-detections.

The 89 CO observations that yield detections were divided into three groups based on their E(B-V) values taken from the SFD dust map. Then, using the SFD dust map, a grid of 810 points, covering a total area of 2 square degrees, was made on top of MBM40. This grid was also divided into three regions based on the E(B-V) values. The knowledge of what fraction of the cloud is in each region (outermost, envelope, or core) allowed us to extrapolate our results to the entire area of MBM40.

6.3.2 Determining H₂ Mass Using W(CO) and X_{CO}

In the previous section we calculated the amount of CO contained in the different regions of MBM40, but one of the main objectives of this thesis is to find the total molecular mass in this cloud. To get the total molecular mass we must find the mass of H₂ in each region. To determine the mass of H₂ from CO measurements we use X_{CO}. In the core region of the cloud 32 of 44 observations had coinciding CH measurements from Chastain (2005) allowing for a more accurate determination of X_{CO}. The core region had an average X_{CO} value of $1.5 \pm 0.32 \times 10^{20} \text{ cm}^{-2} [\text{K km s}^{-1}]^{-1}$, the envelope's average value of $1.9 \pm 0.58 \times 10^{20} \text{ cm}^{-2} [\text{K km s}^{-1}]^{-1}$ was determined from 4 of 31 coinciding measurements. The outermost region had no corresponding CH measurements to determine X_{CO}, so a value of 2.0×10^{20}

Mass ($10^{-6}M_{\odot}$) of CO from observed lines of sight in MBM40 using CO(J=1-0) emission.

Region	$T_{ex} = 10$ K	$T_{ex} = 20$ K	$T_{ex} = 40$ K
Outermost (14)	0.882 ± 0.0875	0.653 ± 0.0647	0.566 ± 0.0561
Envelope (31)	3.63 ± 0.239	2.69 ± 0.177	2.33 ± 0.153
Core (44)	20.5 ± 0.452	15.2 ± 0.334	13.2 ± 0.290

Table 6.2: Mass of CO in 89 of the observed 103 lines of sight in MBM40 divided into three sections based on visual extinction, the number in parentheses represent the number of detections in each region. The beam area is $\approx 2.2 \times 10^{-4}$ square degrees. parentheses represent number of detections in each region.

Total mass ($10^{-4}M_{\odot}$) of CO in MBM40 extrapolated from Table 6.2 using the SFD dust map.

Region	$T_{ex} = 10$ K	$T_{ex} = 20$ K	$T_{ex} = 40$ K
Outermost	2.2 ± 0.22	1.6 ± 0.16	1.4 ± 0.14
Envelope	2.1 ± 0.14	1.5 ± 0.10	1.3 ± 0.087
Core	2.7 ± 0.058	2.0 ± 0.043	1.7 ± 0.038

Table 6.3: Total mass of CO extrapolated over the entire cloud, MBM40, divided into three sections based on visual extinction.

$\text{cm}^{-2} [\text{K km s}^{-1}]^{-1}$ was used to estimate $N(\text{H}_2)$, following our results from Chapter 5. These results are shown in Table 6.4.

6.3.3 Determining H_2 Mass Using $W(\text{CO})$ and $E(\text{B-V})$

Plotting the $W(\text{CO})$ values versus the $E(\text{B-V})$ values for the 89 CO detections in MBM40 gives us a relationship between the two quantities. The relationship of $W(\text{CO})$ with $E(\text{B-V})$ was found in each region independently. Figure 6.3 shows how each region has a slightly different behavior. In the core region $W(\text{CO}) = 120.23 * E(\text{B-V}) - 18.30$, in the envelope region $W(\text{CO}) = 50.69 * E(\text{B-V}) - 6.20$ and in the outermost region $W(\text{CO}) = 50.26 * E(\text{B-V}) - 4.68$ (the three regions had R squared values of 0.62, 0.17, and 0.37, respectively).

Region	N(H ₂) (10 ²⁰ cm ⁻²)	M(H ₂) (M _⊙)
Outermost	1.3 ± 0.20	9.7 ± 1.4
Envelope	2.4 ± 0.75	8.8 ± 2.7
Core	7.5 ± 1.6	9.0 ± 1.9

Table 6.4: Total N(H₂) and mass of H₂ in MBM40 determined by CO emission, using X_{CO} values of 2.0 x 10²⁰, 1.9 x 10²⁰, and 1.5 x 10²⁰ cm⁻² [K km s⁻¹]⁻¹ for the outermost, envelope, and core regions, respectively.

Region	E(B-V)	W(CO)
Outermost	0.0960	0.157 ± 0.0990
Envelope	0.144	1.10 ± 0.917
Core	0.192	4.73 ± 1.79

Table 6.5: Average E(B-V) (mag) values for MBM40 and W(CO) (K km s⁻¹) determined from these E(B-V) values, divided into three sections based on visual extinction. 483 grid points are located in the outermost portion of the cloud, 247 in the envelope, and 80 in the core.

Because there were detections from all three regions of the cloud a linear regression was done to each region to fit the data. Having a relationship for each region allowed for more accurate determination of W(CO) for each of the 3 regions. Using the 810 point grid, with 483 grid points located in the outermost portion of the cloud, 247 in the envelope, and 80 in the core we determined an average E(B-V) value for each region and, from this, an average W(CO) value was established for each region; see Table 6.5. Once W(CO) was calculated for each region it was multiplied by that regions X_{CO} value (determined in section 6.3.2) to obtain the mass of the molecular hydrogen in the cloud. The calculated N(H₂) and total H₂ mass are shown shown in Table 6.7.

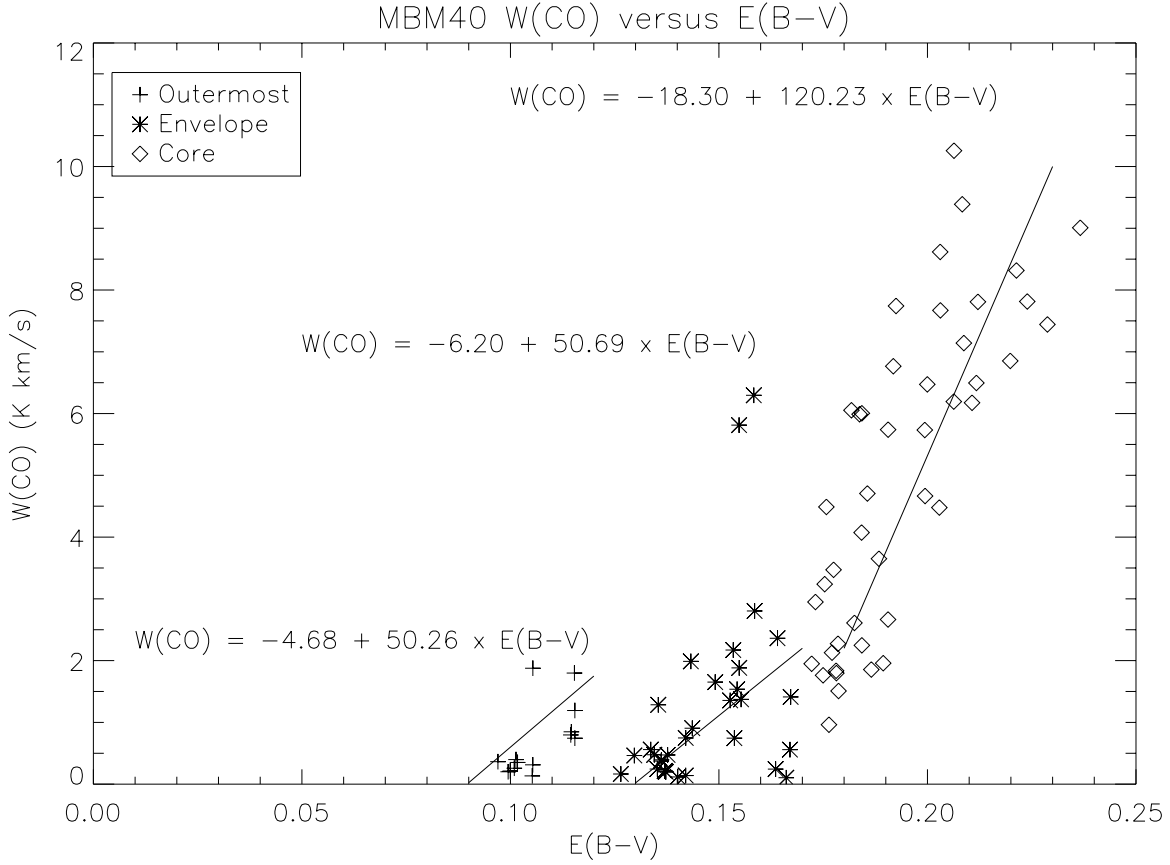


Figure 6.3: $W(\text{CO})$ (K km s^{-1}) versus $E(\text{B-V})$ (mag) for MBM40. Shown are data from all three regions (outermost (+), envelope (*), and core (\diamond)) from the positions shown in Figure 6.2. $W(\text{CO})$ values are from Table 5.1.

Total mass ($10^{-4}M_{\odot}$) of CO in MBM40 using $W(\text{CO})$ and $E(\text{B-V})$ relationship.

Region	$T_{ex} = 10 \text{ K}$	$T_{ex} = 20 \text{ K}$	$T_{ex} = 40 \text{ K}$
Outermost	0.50 ± 0.32	0.37 ± 0.23	0.32 ± 0.20
Envelope	1.8 ± 1.5	1.3 ± 1.1	1.2 ± 0.96
Core	2.5 ± 0.95	1.9 ± 0.70	1.6 ± 0.61

Table 6.6: Total mass of CO calculated from $W(\text{CO})$ versus $E(\text{B-V})$ relationship over the entire cloud, MBM40, divided into three sections based on visual extinction.

Total N(H₂) and H₂ mass in MBM40
from E(B-V) → W(CO) method.

Region	N(H ₂) (10 ²⁰ cm ⁻²)	M(H ₂) (M _⊙)
Outermost	0.31 ± 0.20	2.3 ± 1.4
Envelope	2.1 ± 1.8	7.7 ± 6.7
Core	7.1 ± 3.6	8.4 ± 4.3

Table 6.7: Total N(H₂) and mass of H₂ in MBM40 determined by the relationship between E(B-V) and W(CO) shown in Figure 6.3. X_{CO} values of 1.4 x 10²⁰, 1.2 x 10²⁰, and 1.0 x 10²⁰ cm⁻² [K km s⁻¹]⁻¹ were used for the outermost, envelope, and core regions, respectively, to calculate N(H₂).

6.4 Analysis and Conclusion

In this chapter we have discussed two different methods for determining the molecular mass in MBM40; (1) direct detection of W(CO) and determination of N(H₂) via X_{CO} and extrapolation over the entire cloud based on the SFD dust map, and (2) using a relationship between W(CO) and E(B-V). Method 1 yielded total molecular masses of 9.7 ± 1.4, 8.8 ± 2.7, and 9.0 ± 1.8 M_⊙ in the outermost, envelope, and core regions, respectively, while method 2 yielded corresponding total molecular masses of 2.3 ± 1.4, 7.7 ± 6.7, and 8.4 ± 4.3 M_⊙. These results will be discussed in more detail below and will be compared to the results from our OH observations in Chapter 7.

Chastain (2005) obtained the mass in the core and envelope region of MBM 40 from CO and CH observations. His value for the total mass of the cloud was 30 M_⊙. However, past studies did not focus on the envelope and outermost regions of MBM40, and deep CO(1-0) integrations in these regions do reveal the presence of CO emission. As seen here, the mass contained in the outermost regions of MBM40 can account for nearly a third of the entire cloud mass. Although this is not enough to account for the dark molecular gas hypothesized

by Grenier et al., (2005), the molecular content is significant enough to warrant further study.

Magnani and Onello (1995) surveyed 30 translucent clouds obtaining both $W(\text{CO})$ and X_{CO} values where both the CO(1-0) and CH 3335 MHz lines were detected. The relationship between $W(\text{CO})$ and X_{CO} in the core of MBM40 in the translucent clouds studied by Magnani and Onello have the same functional behavior: $X_{\text{CO}} = 0.59 \cdot [W(\text{CO})^{-0.84}]$.

Our results show that the bulk of the mass lies in the envelope and outermost regions, which contain more than 60 percent more mass than in the core. Surprisingly, a significant amount of mass is found in the outermost regions of the cloud, i.e., those regions with $E(B-V) < 0.12$ mag. This color excess is equivalent to a visual extinction of < 0.4 mag and constitutes a dust regime not normally detected in CO(1-0) surveys.

This work estimated that the outermost region has slightly more molecular mass than the core when using CO emission as the tracer of molecular gas, see Table 6.5. In contrast the $W(\text{CO})$ method yielded a much lower mass estimated for the outermost region of MBM40. It seems clear from these results that molecular envelopes and outer regions in other translucent clouds should be explored to determine if all clouds have substantial mass in their outermost and envelope regions. If it is, then a significant contribution to the so-called “dark” molecular gas of the Galaxy could be found in the envelope and outermost regions of known molecular clouds.

Chapter 7

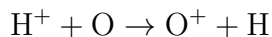
Hydroxyl in MBM 40

7.1 Introduction

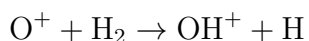
While the CO(1-0) line is the traditional transition for tracing low-density molecular gas, there are a few other candidates. The CH line at 3335 MHz has been successfully used as a surrogate for H₂ in low-density regions (Mattila 1986; Magnani and Onello 1995). Unfortunately, detection of the line in low-extinction regions requires many hours of integration, rendering mapping of cloud envelopes virtually impossible. CH observations of MBM40 were carried out by Chastain (2010) but the integration times were not sufficient to reveal emission from the envelope or outermost regions. The other traditional tracer for low-density molecular gas are the 18 cm lines of hydroxyl, OH. Wouterloot (1981) showed how effective OH could be in low-density regions and Anderson et al. (1993) even claim that the OH 18 cm main lines may trace molecular gas not seen by the CO(1-0) line. In this chapter we will explore the capacity for the OH 18 cm lines to trace molecular gas in the envelope and outermost regions of MBM40.

7.2 Astrochemistry of Hydroxyl

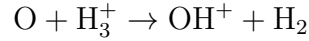
Past studies have shown that the main OH lines found in interstellar clouds are often in local thermodynamic equilibrium, LTE (Guibert et al. 1978). When a cloud is in LTE, the ratio of the different line transition intensities should be constant for a given cloud density, allowing for an accurate measure of the optical depth. In LTE, the ratio of the 1667 : 1665 : 1612 : 1720 lines is 9 : 5 : 1 : 1. If the cloud is in LTE the main lines (1667 and 1665 MHz) seldom show anomalous ratios but the satellite lines (1612 and 1720 MHz) are more likely to show anomalies (Wouterloot 1981). Guibert et al. (1978) presented a model to explain some observational anomalies by looking at collisions with neutral and charged particles in interstellar clouds. For $T < 40$ K, the 1720 MHz line can be inverted by collisions with neutral hydrogen while higher temperatures can invert either the 1720 or the 1612 MHz line, with main line inversions occurring at temperatures greater than 100 K; too high to be of importance in the clouds studied in this thesis. Diffuse molecular clouds contain primarily diatomic molecules and relatively few reactions are needed to determine their abundances from astrochemical models (van Dishoeck 1990). However, reactions will differ from the inner parts of the cloud to outer parts of the cloud due to density and temperature differences. At low temperatures the charge transfer reaction of O and H



is very efficient, and since the ionization potential of O and H are close to the same value, only a small amount of energy is needed to initiate the charge transfer reaction. The resulting oxygen ion reacts quickly with molecular hydrogen to form OH^+ (van Dishoeck 1990):

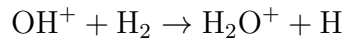


While the charge transfer reaction of O and H are efficient, another route in which OH^+ can form is through the fast exothermic reaction:

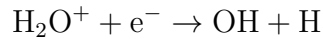


but this reaction is strongly dependent on the way in which H_3^+ dissociates.

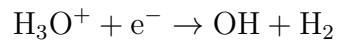
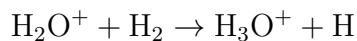
Multiple studies have shown that H_3^+ abundances are extremely high in translucent clouds because electrons do not react well with H_3^+ at the temperatures of translucent/diffuse molecular clouds (van Dishoeck 1990). Once OH^+ is available, the reaction



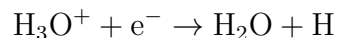
occurs forming a water ion and a hydrogen atom. The newly created H_2O^+ forms OH and H in a dissociative recombination reaction with a free electron:

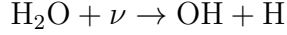


The final principal way that OH is produced in diffuse and translucent clouds, is similar to the previous reaction sequence in that it involves dissociative recombination and starts with H_2O^+ but takes a few more steps to form OH (Singh and de Almeida 1980):



or through a different dissociative reaction followed by a photodissociative reaction:





All these reactions are dependent on the interstellar radiation field (ISRF), initial elemental abundances, cosmic ray ionization rate, dust content and size distribution, and mechanical heating sources (e.g., shocks). Because the photodissociative properties of the ISRF control the destruction of molecular species, it is one of the main determinants of which reactions will dominate.

Chemical models of molecular clouds now include tens of thousands of reactions and some even include temporal evolution of molecular abundances. Molecular clouds are individual entities with each one subject to different initial conditions; thus, chemical models can be used to give general indications of the abundances in a particular type of cloud subject to particular initial conditions. It must be expected that variations occur from cloud to cloud and even within a particular cloud.

One of the earliest comprehensive models of translucent and diffuse molecular clouds was by Viala (1986). His steady-state model includes over 1000 reactions and 80 species formed from H, C, N, and O. The closest model to the conditions pertinent to MBM40 is what he calls a “molecular diffuse cloud”. This model uses an ISRF taken from Gondhalekar et al. (1975), an extinction value of $A_V = 1$ mag, $N(\text{H}_{\text{Total}}) = 2 \times 10^{21} \text{ cm}^{-2}$, the doppler width of the lines is 4 km s^{-1} , and kinetic temperature $T = 50 \text{ K}$. For n_{H} of 100 to 1000 cm^{-3} , the OH abundance with respect to H_2 varies from 9.4×10^{-9} to 3.8×10^{-9} (Viala 1986). Another model by Nercessian, Benayoun, and Viala (1988), for the translucent cloud along the line of sight towards HD 29647, has the initial conditions: $A_V = 3.7$ mag, $n_{\text{H}} = 800 \text{ cm}^{-3}$, $T = 10 \text{ K}$, and the ISRF from Mathis et al. (1983). In the Nercessian et al. (1988) models the OH abundance with respect to H_2 varies from 1.2×10^{-6} to 2.6×10^{-8} for different heavy element depletions and cosmic ray ionization rates (Nercessian et al. 1988).

Van Dishoeck and Black (1986) also calculated comprehensive models of diffuse and

translucent clouds. They calculate 19 models with n_{H} ranging from 250 to 1000 cm^{-3} and T ranging from 20 to 100 K, yielding OH abundances ranging from 1.7×10^{-7} to 2.72×10^{-9} (Van Dishoeck and Black 1986). Other OH abundances were obtained for translucent clouds by van Dishoeck (1990) with values in the range 1.1×10^{-7} to 2.3×10^{-7} . Empirically, Magnani, Blitz and Wouterloot (1988) established OH abundances with a small sample of translucent clouds to be in the range 4×10^{-6} to 2×10^{-7} .

7.3 Observations

Observations of the 18 cm ground state transitions of OH in MBM40 were made using the Robert C. Byrd 100 m radio telescope (hereafter GBT) in Green Bank, WV, during December of 2009 and January of 2010.¹ The data were collected with the GBT for a total of 36 hours implementing the position switching technique. This technique of data collection consists of observations “on” a source followed by observations in the “off” source position for the same amount of time. The “off” position, necessary to remove instrumental effects, ranged between 1 and 2 degrees away from the “on” position, with exact locations chosen based on the lack of emission in the SFD-dust map. Other criteria for determining the “off” positions were based on moving the telescope in azimuth only, thereby maintaining similar atmospheric attenuation for the “on” and “off” source positions.

The spectra collected from the 100 m GBT were produced using an autocorrelator spectrometer subdivided into four sections centered on: 1720.5300, 1667.3590, 1665.4018, and 1612.2310 MHz, the rest frequencies of the four ground state transition of OH. For each scan two polarizations were taken, left circularly polarized, LL, and right circularly polarized, RR. The bandwidth of each spectrum is 12.5 MHz, which corresponds to a velocity range of 2249.07 km/s for the 1667 MHz line, and 2251.71 km/s for the 1665 MHz line. The velocity

¹The GBT is part of The National Radio Astronomy Observatory and is a facility of the National Science Foundation operated under cooperative agreement by Associated Universities, Inc. (www.gb.nrao.edu).

resolution of each channel was 0.059 km/s. With the 100 m GBT, the 1667 MHz line corresponds to an angular resolution of 6.2 arc minutes. The beam efficiency of the GBT is given by 1.32 times the aperture efficiency; where the aperture efficiency is defined as the ratio of effective collecting area to physical collecting area, depending on the telescope geometry and on the frequency being observed. The beam efficiency of a telescope is based on the amount of energy lost to the side lobes versus the main beam. For the observation of the transition lines of hydroxyl the aperture efficiency is approximately 0.71, which corresponds to a beam efficiency of 0.94 at 18 cm (Maddelena 2009).

7.4 Results

Most studies of molecular clouds have focused on the dense core regions which are often the site of star formation, or potential star formation. The surrounding envelope region is less often studied because of the significantly weaker lines and lack of star forming activity. However, it is key for understanding the atomic-molecular interface. In light of the results of Grenier, Casandjian, and Terrier (2005), i.e., that regions of substantial molecular column density not detectable in CO exist surrounding the traditional CO-defined molecular clouds, tracers like the 18 cm OH main lines might be able to detect an outermost molecular region surrounding the core and envelope regions of all clouds. We thus made OH observations of these three regions in the translucent molecular cloud, MBM40. Since we only had 21 detections for 35 total observations we combined our data with data from Wennerstrom (2007). Her data was taken from the same telescope and consisted of 11 detections for 17 observations. The positions of both sets of data are shown in Figure 7.1, where the observations taken by Wennerstrom (2007) are represented by squares and observations from this work are represented by circles. Red observations represent positions with no signal, yellow observations indicate a detection but with intensities less than 0.05 K km s^{-1} , black

observations represent intensities between 0.05 and 0.1 K km s⁻¹, and green observations indicate detections with intensities stronger than 0.1 K km s⁻¹. For the rest of this dissertation the observations from this work will be combined with the observations from Wennerstrom (2007) unless indicated.

To analyze the data, the cloud and its environment were divided into a grid with 810 equal squares, each side of length 0.05°, or 3'. Using the Schlegel, Finkbeiner, and Davis (SFD) dust maps (Schlegel et al. 1998), E(B-V) values were then found for each grid point. These grid points were then divided into three regions determined by their E(B-V) values: 1) E(B-V) < 0.12 mag, 2) 0.12 ≤ E(B-V) ≤ 0.17, and 3) E(B-V) > 0.17, where the three sections have been referred to as the “outermost”, the “envelope”, and the “core” regions, respectively. The distribution of visual extinction throughout the cloud reveals that 483 grid points are located in the outermost portion of the cloud, 247 in the envelope, and 80 in the core. Using this information and two different analysis techniques, we now determine the mass of H₂ in MBM40 and its three sub-regions.

7.4.1 Determining H₂ Mass: Past Studies

Chastain (2010), using ¹²CO emission, estimated the molecular mass of MBM40 to be 15 M_⊙, with a total mass (including helium and atomic hydrogen) of ~ 30 M_⊙. Magnani et al. (1996) also obtained a total cloud mass of ~ 15 M_⊙ in MBM40 using W(CO) observations.. But Chastain (2010) recalculated the mass using a larger cloud area, based on the weak CO emission found in the envelope regions, and a more refined X_{CO} value than used by Magnani et al. (1996) to get a total cloud mass ~ 40 M_⊙ for MBM40. Much of the disparity of the two studies comes from the unknown distance to MBM40, with Magnani et al. (1996) using a distance of 100 pc and Chastain (2005) using a distance of 80 pc. Chastain also used CH emission to estimate the molecular mass of the cloud to be ~ 7 M_⊙ and a total cloud mass of ~ 21 M_⊙, which agrees with his estimate derived from ¹²CO emission. Finally using the

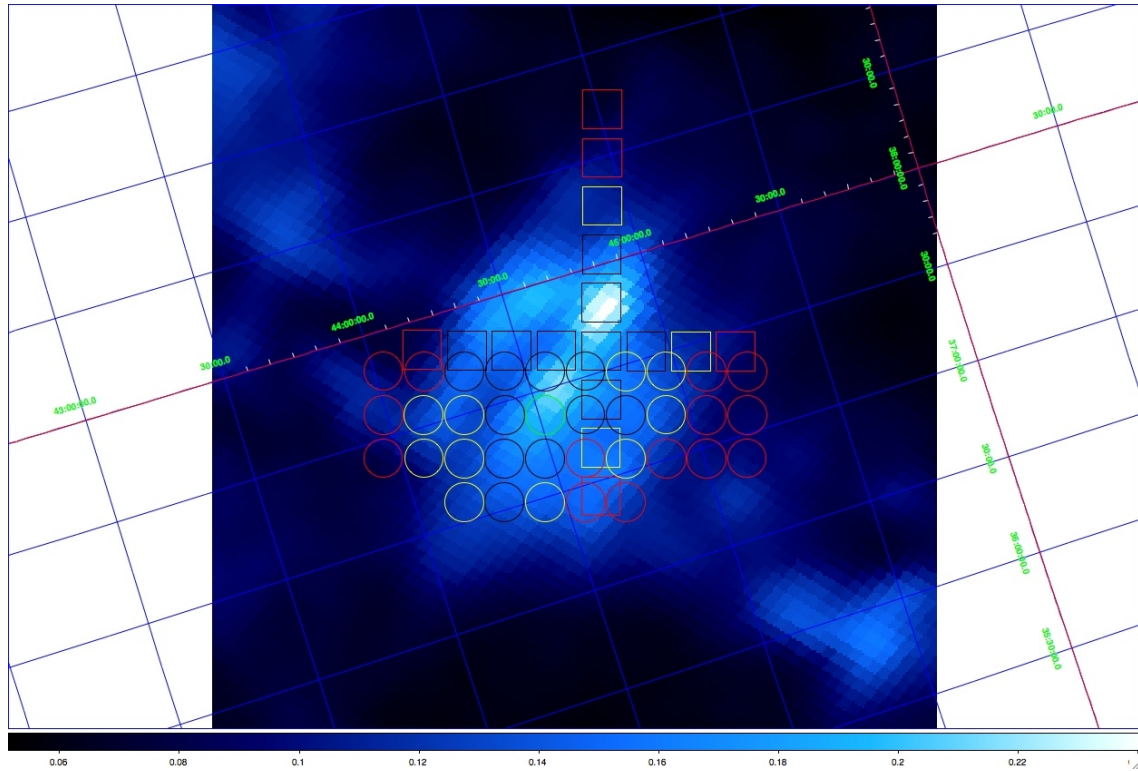


Figure 7.1: The dust map of MBM40 obtained from the SFD data set. The positions of OH observations represented as circles are from this work, and the observations represented by squares are from Wennerstrom (2007). The color of the circles corresponding to $W(\text{OH})$ intensity, in units of (K km s^{-1}) .

SFD dust map Chastain calculated the total cloud mass of MBM40, using E(B-V) values and gas to dust conversion of Bohlin, Savage, and Drake (1978), to be $\sim 26 M_{\odot}$. Chastain's three techniques thus found total molecular masses for MBM40 ranging from 21 to $40 M_{\odot}$.

7.4.2 Determining H_2 Mass From OH 1667 MHz emission

In order to obtain spectra that are normalized for each position, all the scans collected for a given position are averaged, and a baseline is subtracted. A Gaussian curve is fit to the signal where a full width half maximum, centroid velocity, and peak temperature at line center are obtained from the fit. These results are shown in Table 7.2. Using the peak temperature at line center (T_A), and the full width half maximum (Δv) we can derive a value for $W(OH_{1667})$, where $W(OH_{1667}) = T_A \times \Delta v \times (1.07/0.94)$, with 1.07 coming from the area under a gaussian and 0.94 is from converting the measured T_R to the commonly used T_A . $W(OH)$ and other observed values for MBM40 are shown in Table 7.1. Using the 1667 MHz OH spectra, we can estimate the mass of OH in the outermost, envelope, and core regions. We can estimate the OH mass of the cloud by first obtaining the OH column density ($N(OH)$) from our observations of $W(OH_{1667})$ using Equation 7.1.

$$N_u = (g_l/g_u)(1/A_{ul})(1/\lambda^3)(8\pi^{1/2}/(2\ln 2)^{1/2})[1 - e^{-h\nu/kT_{ex}}]^{-1}(T_{ex} - T_{BG})^{-1}W(OH) \text{ (cm}^{-2}\text{)} \quad (7.1)$$

where A_{ul} , the Einstein A coefficient, is $7.78 \times 10^{-11} \text{ s}^{-1}$ for the 1667.359 MHz transition. Unlike the CO case, the OH 18 cm lines are optically thin and most of the molecules are in the ground state, so our estimate of $N(OH)$ is likely to be quite accurate.

Table 7.1: Coordinates and observed OH values in MBM40, data from this work and Wennerstrom (2007).

Position	RA(2000) (deg)	Dec(2000) (deg)	T_R (K)	v_{LSR} (km s ⁻¹)	Δv (km s ⁻¹)	W(OH) (K km s ⁻¹)
OH_01	243.35	21.80				10 mK
OH_02	243.20	21.80				11 mK
OH_03	243.05	21.80	0.075	2.943	0.646	0.055 + 0.012
OH_04	242.90	21.80	0.070	3.250	0.718	0.057 + 0.013
OH_05	242.75	21.80	0.155	3.313	0.514	0.091 + 0.011
OH_06	242.60	21.80	0.103	3.345	0.583	0.068 + 0.011
OH_07	242.45	21.80	0.052	3.730	0.394	0.023 + 0.006
OH_08	242.30	21.80	0.057	3.665	0.694	0.045 + 0.011
OH_09	242.15	21.80				13 mK
OH_10	242.00	21.80				13 mK
OH_11	243.35	21.65				15 mK
OH_12	243.20	21.65	0.041	2.592	0.811	0.038 +/- 0.012
OH_13	243.05	21.65	0.032	3.088	0.849	0.031 +/- 0.014
OH_14	242.90	21.65	0.081	3.316	0.790	0.073 +/- 0.018
OH_15	242.75	21.65	0.129	3.317	0.849	0.124 +/- 0.021
OH_16	242.60	21.65	0.043	3.484	1.576	0.077 +/- 0.026
OH_17	242.45	21.65	0.041	3.242	1.403	0.065 +/- 0.023
OH_18	242.30	21.65	0.042	3.295	0.900	0.043 +/- 0.014
OH_19	242.15	21.65				14 mK
OH_20	242.00	21.65				14 mK
OH_21	243.35	21.50				19 mK
OH_22	243.20	21.50	0.033	2.595	0.461	0.017 +/- 0.007
OH_23	243.05	21.50	0.049	3.327	0.698	0.039 +/- 0.013
OH_24	242.90	21.50	0.083	3.324	0.632	0.060 +/- 0.012
OH_25	242.75	21.50	0.075	3.556	0.779	0.067 +/- 0.015
OH_26	242.60	21.50				14 mK
OH_27	242.45	21.50	0.037	3.205	0.803	0.034 +/- 0.013
OH_28	242.30	21.50				20 mK
OH_29	242.15	21.50				20 mK
OH_30	242.00	21.50				21 mK
OH_33	243.05	21.35	0.061	3.021	0.340	0.023 +/- 0.008

continued on next page

Table 7.1 – continued from previous page

Position	RA(2000) (deg)	Dec(2000) (deg)	T _R (K)	v _{LSR} (km s ⁻¹)	Δv (km s ⁻¹)	W(OH) (K km s ⁻¹)
OH_34	242.90	21.35	0.036	3.420	1.303	0.053 +/- 0.028
OH_35	242.75	21.35	0.051	3.193	0.758	0.044 +/- 0.015
OH_36	242.60	21.35				14 mK
OH_37	242.45	21.35				16 mK
Wennerstrom (2007) data						
OH_C	242.54	21.87	0.050	3.251	0.712	0.041 +/- 0.013
OH_N1	242.54	22.03	0.123	2.960	0.857	0.120 +/- 0.018
OH_N2	242.53	22.20	0.107	3.060	0.693	0.085 +/- 0.014
OH_N3	242.53	22.37	0.044	3.473	0.887	0.045 +/- 0.017
OH_N4	242.53	22.53				10 mK
OH_N5	242.53	22.70				14 mK
OH_S1	242.54	21.70	0.055	3.494	1.346	0.084 +/- 0.025
OH_S2	242.54	21.53	0.040	3.110	1.031	0.047 +/- 0.013
OH_S3	242.54	21.37				10 mK
OH_W1	242.37	21.86	0.056	3.658	0.939	0.060 +/- 0.018
OH_W2	242.20	21.86	0.030	3.625	0.499	0.017 +/- 0.006
OH_W3	242.04	21.86				9 mK
OH_E1	242.70	21.87	0.087	3.304	0.643	0.064 +/- 0.012
OH_E2	242.87	21.87	0.072	3.032	0.820	0.068 +/- 0.017
OH_E3	243.04	21.87	0.048	3.129	1.290	0.070 +/- 0.025
OH_E4	243.20	21.87				10 mK

This approach requires knowing the excitation temperature of the transition. We determined N(OH) for three reasonable guesses of the excitation temperature (10 K, 20 K, and 40 K). From N(OH), we can get the mass of OH from the following equation:

$$\text{Mass(OH)} = \text{N(OH)}\Omega d^2 \text{ (M}_\odot\text{)} \quad (7.2)$$

where Ω is the solid angle covered by the region in question and d is the distance to the cloud. Using the column densities, which are listed in Table 7.2, a cloud distance of 140 pc, and Equation 7.2, OH mass estimates for the different regions can be found for each excitation temperature, with the results shown in Table 7.3.

Table 7.2: Coordinates and column densities for observed OH positions in MBM40

Position	RA(2000)	Dec(2000)	N(OH) ¹		N(OH) ¹
	(deg)	(deg)	T _{ex} = 10 K	T _{ex} = 20 K	T _{ex} = 40 K
OH_01	243.35	21.80	0	0	0
OH_02	243.20	21.80	0	0	0
OH_03	243.05	21.80	7.986 +/- 1.724	6.710 +/- 1.449	6.212 +/- 1.342
OH_04	242.90	21.80	8.285 +/- 1.873	6.961 +/- 1.574	6.445 +/- 1.457
OH_05	242.75	21.80	13.12 +/- 1.546	11.03 +/- 1.299	10.21 +/- 1.203
OH_06	242.60	21.80	9.873 +/- 1.610	8.296 +/- 1.353	7.681 +/- 1.253
OH_07	242.45	21.80	3.373 +/- 0.801	2.834 +/- 0.673	2.624 +/- 0.623
OH_08	242.30	21.80	6.479 +/- 1.587	5.444 +/- 1.331	5.040 +/- 1.234
OH_09	242.15	21.80	0	0	0
OH_10	242.00	21.80	0	0	0
OH_11	243.35	21.65	0	0	0
OH_12	243.20	21.65	5.488 +/- 1.779	4.611 +/- 1.495	4.269 +/- 1.384
OH_13	243.05	21.65	4.425 +/- 1.972	3.718 +/- 1.657	3.442 +/- 1.534
OH_14	242.90	21.65	10.55 +/- 2.632	8.864 +/- 2.211	8.206 +/- 2.047
OH_15	242.75	21.65	17.95 +/- 3.055	15.08 +/- 2.567	13.97 +/- 2.376
OH_16	242.60	21.65	11.11 +/- 3.721	9.337 +/- 3.126	8.645 +/- 2.895
OH_17	242.45	21.65	9.468 +/- 3.384	7.955 +/- 2.843	7.365 +/- 2.632
OH_18	242.30	21.65	6.211 +/- 2.004	5.219 +/- 1.684	4.832 +/- 1.559
OH_19	242.15	21.65	0	0	0
OH_20	242.00	21.65	0	0	0
OH_21	243.35	21.50	0	0	0
OH_22	243.20	21.50	2.507 +/- 1.037	2.106 +/- 0.872	1.950 +/- 0.807
OH_23	243.05	21.50	5.614 +/- 1.849	4.717 +/- 1.553	4.367 +/- 1.438
OH_24	242.90	21.50	8.606 +/- 1.696	7.231 +/- 1.425	6.695 +/- 1.320
OH_25	242.75	21.50	9.636 +/- 2.104	8.096 +/- 1.768	7.496 +/- 1.637
OH_26	242.60	21.50	0	0	0

continued on next page

Table 7.2 – continued from previous page

Position	RA(2000)	Dec(2000)	N(OH) ¹		N(OH) ¹
	(deg)	(deg)	T _{ex} = 10 K	T _{ex} = 20 K	T _{ex} = 40 K
OH_27	242.45	21.50	4.902 +/- 1.880	4.119 +/- 1.580	3.813 +/- 1.463
OH_28	242.30	21.50	0	0	0
OH_29	242.15	21.50	0	0	0
OH_30	242.00	21.50	0	0	0
OH_33	243.05	21.35	3.397 +/- 1.100	2.854 +/- 0.925	2.643 +/- 0.856
OH_34	242.90	21.35	7.734 +/- 4.005	6.498 +/- 3.365	6.016 +/- 3.116
OH_35	242.75	21.35	6.389 +/- 2.111	5.368 +/- 1.777	4.970 +/- 1.642
OH_36	242.60	21.35	0	0	0
OH_37	242.45	21.35	0	0	0
Wennerstrom (2007) data					
OH_C	242.54	21.87	5.878 +/- 1.887	4.939 +/- 1.585	4.572 +/- 1.468
OH_N1	242.54	22.03	17.30 +/- 2.545	14.53 +/- 2.138	13.45 +/- 1.980
OH_N2	242.53	22.20	12.22 +/- 2.034	10.27 +/- 1.709	9.507 +/- 1.582
OH_N3	242.53	22.37	6.471 +/- 2.479	5.437 +/- 2.083	5.034 +/- 1.929
OH_N4	242.53	22.53	0	0	0
OH_N5	242.53	22.70	0	0	0
OH_S1	242.54	21.70	12.08 +/- 3.664	10.15 +/- 3.079	9.394 +/- 2.851
OH_S2	242.54	21.53	6.798 +/- 1.940	5.712 +/- 1.630	5.288 +/- 1.509
OH_S3	242.54	21.37	0	0	0
OH_W1	242.37	21.86	8.700 +/- 2.552	7.310 +/- 2.144	6.768 +/- 1.985
OH_W2	242.20	21.86	2.444 +/- 0.829	2.054 +/- 0.697	1.901 +/- 0.645
OH_W3	242.04	21.86	0	0	0
OH_E1	242.70	21.87	9.185 +/- 1.698	7.718 +/- 1.427	7.145 +/- 1.321
OH_E2	242.87	21.87	9.760 +/- 2.438	8.201 +/- 2.049	7.593 +/- 1.897
OH_E3	243.04	21.87	10.10 +/- 3.622	8.490 +/- 3.043	7.860 +/- 2.818
OH_E4	243.20	21.87	0	0	0

continued on next page

Upon estimating the mass of OH in each line of sight for each region, ratios of the observed to non-observed area were determined for each region. These ratios were found so

Mass ($10^{-7}M_{\odot}$) of OH from observed lines of sight in
MBM40 using OH 1667 MHz emission.

Region	$T_{ex} = 10$ K	$T_{ex} = 20$ K	$T_{ex} = 40$ K
Outermost	0.773 ± 0.294	0.650 ± 0.247	0.601 ± 0.229
Envelope	10.6 ± 3.05	8.88 ± 2.56	8.22 ± 2.37
Core	6.53 ± 1.34	5.49 ± 1.12	5.08 ± 1.04

Table 7.3: Mass of OH in 32 of the observed 51 lines of sight toward MBM40 from this work and Wennerstrom (2007) in MBM40 divided into three sections based on visual extinction. The beam area is $\approx 1.4 \times 10^{-2}$ square degrees.

Total mass ($10^{-7}M_{\odot}$) of OH in MBM40
using OH 1667 MHz emission.

Region	$T_{ex} = 10$ K	$T_{ex} = 20$ K	$T_{ex} = 40$ K
Outermost	23.0 ± 8.76	19.4 ± 7.36	17.9 ± 6.82
Envelope	23.0 ± 6.64	19.3 ± 5.58	17.9 ± 5.17
Core	12.1 ± 2.47	10.2 ± 2.08	9.40 ± 1.92

Table 7.4: Total mass of OH extrapolated over the entire MBM40 cloud (from this work and Wennerstrom (2007)) divided into three sections based on visual extinction.

that we could extrapolate the estimated mass of OH where data were taken to areas we had not observed. Using this technique we can estimate the mass of each of the three regions of the cloud. These results are shown in Table 7.4, with the total estimated mass of OH for the outermost region removed due to such a small observable sample relative to the total size of the outermost region.

To go from the OH mass to the H_2 mass, the ratio of OH/ H_2 must be known. We established earlier in Section 7.2 that the OH abundance in translucent clouds can range from 4×10^{-9} to 1×10^{-6} .

To get an accurate measure of the molecular mass in the envelope of MBM40 we will use the mass estimate from Chastain (2010). Since 80% of his total molecular mass was found

Total H ₂ (M _⊙) mass in MBM40.			
Region	T _{ex} = 10 K	T _{ex} = 20 K	T _{ex} = 40 K
Outermost	38.4 ± 14.6	32.3 ± 12.3	29.9 ± 11.4
Envelope	38.3 ± 11.1	32.2 ± 9.30	29.8 ± 8.61
Core	20.1 ± 4.12	16.9 ± 3.46	15.7 ± 3.20

Table 7.5: Total mass of H₂ in MBM40 determined by OH 1667 MHz emission, and an OH/H₂ abundance ratio of 6×10^{-8} ; divided into three sections based on visual extinction. Data are from this work and Wennerstrom (2007).

in the core he estimated his core molecular mass to be $\sim 12 M_{\odot}$. Using our data in Table 7.4 we found that an OH/H₂ abundance ratio for the core in the range of previous studies ($\sim 6.8 \times 10^{-8}$ - 5.3×10^{-8}) produces an H₂ mass of $\sim 12 M_{\odot}$ in the core for the range of excitation temperature we use. Therefore for the rest of this work we will use an OH/H₂ ratio of 6.0×10^{-8} for all three regions of MBM40. This agrees with the OH/H₂ abundance used by Wennerstrom (2007). In a similar way we determined the mass of H₂ in MBM40 to be 17.2 to 32.8 M_⊙. Results for the total H₂ in MBM40 for the core and envelope can be found in Table 7.5.

7.4.3 Determining H₂ Mass Using W(OH) with E(B-V)

Using OH 1667 MHz data obtained from the GBT, values of W(OH) were determined. In conjunction with W(OH), E(B-V) values were determined for each W(OH) line of sight using the (SFD) dust map. In Figure 7.2, we plot W(OH) versus E(B-V) where data from this work and Wennerstrom (2007) are shown in the same graph, and the best fit line applies only to the nonzero data for both works and has an R squared value of 0.60. Using this best fit line, an estimated value of W(OH) can be determined if E(B-V) is known for each region.

Using the 810 point grid, we determined an average E(B-V) value for each section and,

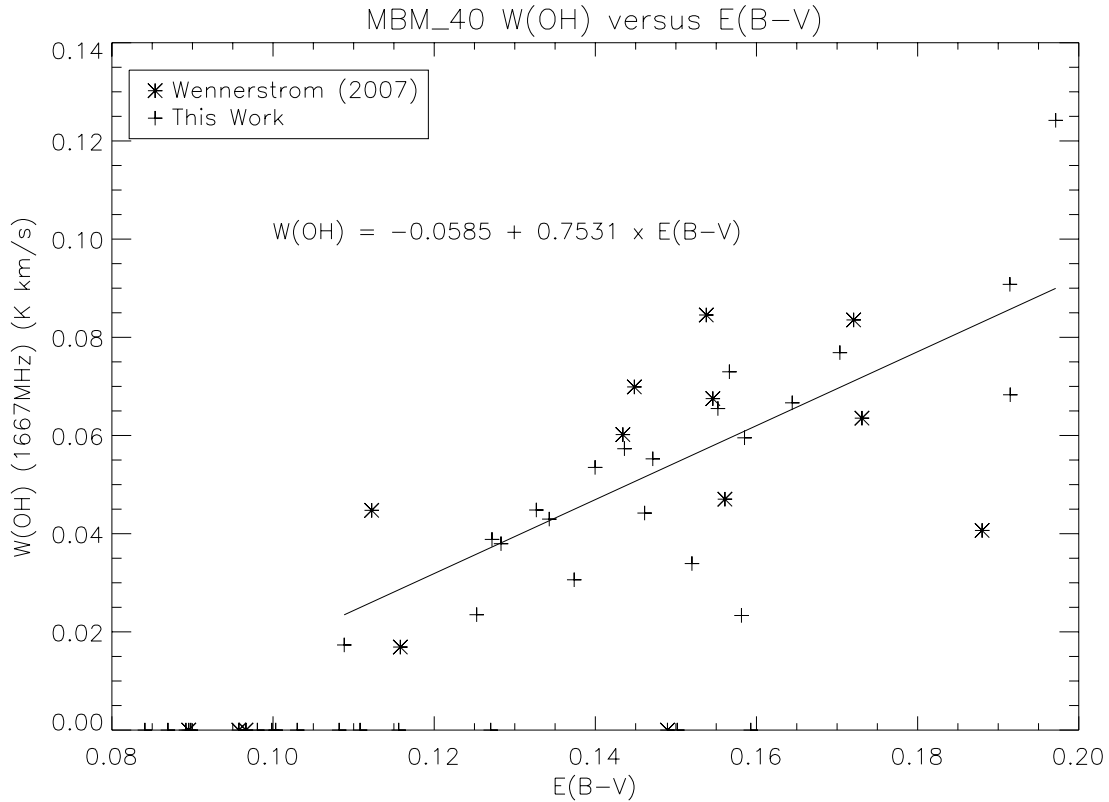


Figure 7.2: $W(\text{OH})$ (K km s^{-1}) versus $E(\text{B-V})$ (mag) for MBM40. Shown are data from Wennerstrom 2007 (*) and data from the positions shown in Table 7.2 (+). The best fit line is fit only to non zero data.

Average values for MBM40		
Region	$E(\text{B-V})$	$W(\text{OH})$
Outermost	0.0959	0.0138 ± 0.00548
Envelope	0.144	0.0501 ± 0.0199
Core	0.192	0.0857 ± 0.0341

Table 7.6: Average $E(\text{B-V})$ (mag) values for MBM40 and the $W(\text{OH})$ (K km s^{-1}) determined from these $E(\text{B-V})$ values, divided into three sections based on visual extinction. 483 grid points are located in the outermost portion of the cloud, 247 in the envelope, and 80 in the core.

Average values of N(OH) (cm^{-2}) $\times 10^{12}$ for MBM40			
Region	$T_{ex} = 10 \text{ K}$	$T_{ex} = 20 \text{ K}$	$T_{ex} = 40 \text{ K}$
Outermost	1.99 ± 0.792	1.67 ± 0.666	1.55 ± 0.616
Envelope	7.24 ± 2.88	6.08 ± 2.42	5.63 ± 2.24
Core	12.4 ± 4.93	10.4 ± 4.14	9.64 ± 3.83

Table 7.7: Average N(OH) (cm^{-2}) $\times 10^{12}$ values for MBM40 determined from the values in Table 7.6, divided into three sections based on visual extinction. Three plausible estimates for the excitation temperature are given for each section.

Total M(OH) $\times 10^{-6} M_{\odot}$ for MBM40			
Region	$T_{ex} = 10 \text{ K}$	$T_{ex} = 20 \text{ K}$	$T_{ex} = 40 \text{ K}$
Outermost	1.21 ± 0.479	1.01 ± 0.403	0.938 ± 0.373
Envelope	2.24 ± 0.889	1.88 ± 0.747	1.74 ± 0.692
Core	1.24 ± 0.494	1.04 ± 0.416	0.966 ± 0.384

Table 7.8: Total M(OH) ($10^{-6} M_{\odot}$) for MBM40 determined from the values in Table 7.7, divided into three sections based on visual extinction. Three plausible estimates for the excitation temperature are given for each section.

Total M(H_2) (M_{\odot}) from E(B-V) \rightarrow W(OH) method.			
Region	$T_{ex} = 10 \text{ K}$	$T_{ex} = 20 \text{ K}$	$T_{ex} = 40 \text{ K}$
Outermost	20.1 ± 7.98	16.9 ± 6.71	15.6 ± 6.21
Envelope	37.3 ± 14.8	31.3 ± 12.5	29.0 ± 11.5
Core	20.7 ± 8.23	17.4 ± 6.91	16.1 ± 6.40

Table 7.9: Total M(H_2) (M_{\odot}) for MBM40 determined from the values in Table 7.6, and using a OH/ H_2 abundance ratio of 6×10^{-8} divided into three sections based on visual extinction. 483 grid points are located in the outermost portion of the cloud, 247 in the envelope, and 80 in the core. Three plausible estimates for the excitation temperature are given for each section.

from this, an average $W(\text{OH})$ value is established for each section (see Table 7.6). An average value of $N(\text{OH})$ is now calculated from Equation 7.1. Those values for all three sections of MBM40 are shown in Table 7.7. We now use the average $N(\text{OH})$ values from each section, the area of each section, and Equation 7.2 to determine the total OH mass contained in MBM40, with the results displayed in Table 7.8. Finally, using the total OH mass of the cloud and the previously discussed OH/H₂ abundance ratio of 6×10^{-8} , we compute the total molecular mass of MBM40 for each section (see Table 7.9). This total molecular mass calculation for MBM40 was done using the relationship between the observed OH 1667 MHz emission and $E(\text{B-V})$, and it gave us the opportunity to get a measure of the molecular mass, not only in the core and envelope regions of MBM40, but also the outermost region.

7.4.4 Determining H₂ Mass Using $E(\text{B-V})$

The previous section employed the relationship between $W(\text{OH})$ and $E(\text{B-V})$, to obtain $M(\text{OH})$ and then $M(\text{H}_2)$ of MBM40, using the abundance ratio. However, Bohlin, Savage, and Drake (1978) showed that total hydrogen column density can be computed directly from $E(\text{B-V})$.

$$\langle N(\text{HI} + \text{H}_2)/E(\text{B} - \text{V}) \rangle = 5.8 \times 10^{21} \text{ atoms cm}^{-2} \text{ mag}^{-1} \quad (7.3)$$

In Equation 7.3, $N(\text{HI} + \text{H}_2) = N(\text{HI}) + 2N(\text{H}_2)$, and $N(\text{HI})$ represents the column density of atomic hydrogen (Bohlin et al. 1978). Because atomic hydrogen can contribute about 50% of the mass in translucent clouds, the mass contribution from HI needs to be determined in order to obtain an accurate H₂ mass (Gir et al. 1994). Chastian (2005) showed that $N(\text{HI})$ values did not deviate much from the average value of $2.03 \pm 0.11 \times 10^{20} \text{ cm}^{-2}$ in different locations of MBM40, but that $N(\text{H}_2)$ could vary by more than a factor of three. Using this information, the total atomic and molecular masses of hy-

Hydrogen Data from E(B-V)				
Region	E(B-V) (mag)	N(HI + H ₂) (x 10 ²⁰)(cm ⁻²)	M(HI) (M _⊙)	M(H ₂) (M _⊙)
Outermost	0.0959	5.57	7.28 ± 0.39	12.7 ± 0.79
Envelope	0.144	8.36	3.72 ± 0.20	11.6 ± 0.40
Core	0.192	11.1	1.21 ± 0.065	5.39 ± 0.13

Table 7.10: Average E(B-V), total column density of hydrogen determined from Equation 7.3, and total atomic and molecular hydrogen mass for MBM40, divided into three sections based on visual extinction.

drogen were calculated. The N(H₂) values were calculated from the given N(HI) value and $N(\text{HI} + \text{H}_2) = N(\text{HI}) + 2N(\text{H}_2)$. Equation 7.2 was then for all three regions of the cloud and these data are shown in Table 7.10.

7.5 Analysis

In this chapter we have discussed three methods for determining the amount of molecular mass in MBM40; (1) direct detection of W(OH) and using an OH/H₂ abundance ratio of 6×10^{-8} , (2) using the relationship between W(OH) and E(B-V) then the abundance ratio, and (3) using E(B-V) to directly get the total hydrogen column density.

Method 1 yielded total molecular hydrogen masses averaging 17.2 M_⊙ in the core and 32.7 M_⊙ in the envelope and 32.8 M_⊙ in the outermost region of MBM40 (Table 7.5), while method 2 produced masses of molecular hydrogen averaging 17.7 M_⊙ in the core, 31.2 M_⊙ in the envelope, and 17.2 M_⊙ in the outermost regions of MBM40 (Table 7.9). The last method, using the Bohlin, Savage, and Drake (1978) technique, resulted in molecular hydrogen masses for MBM40 of $\approx 5, 12,$ and 13 M_\odot for the core, the envelope, and outermost regions, respectively (Table 7.10). Once again, as was the case from the CO data, both OH

methods and the E(B-V) method show that the envelope and outermost regions contain significant molecular mass.

7.6 Conclusion

If we average the two OH methods, we get the following values for the core, envelope, and outermost regions: 17.3, 32.4, and 20.8 M_{\odot} . These results compare favorably with those described from our CO observations. Since our estimates are based directly on the OH/H₂ ratio, slight changes in the ratio can bring our OH estimates more in line with the CO results.

Chapter 8

Summary and Future Work

Throughout this thesis we have focused on the importance of including the diffuse component of molecular clouds into the calculation of total molecular mass. We found that the mass of molecular hydrogen in the diffuse regions can play a significant role in the total mass content of a translucent cloud (MBM40) and, if this is true for all molecular clouds, this concept would extend to all the molecular clouds in the Galaxy. Grenier et al. (2005) have proposed that about half the molecular mass of the Galaxy may be in a form not detectable by conventional radio spectroscopic techniques. However, this assessment was based on comparing other tracers of H_2 to typical CO(1-0) observations. Their observations are made with a relatively high rms noise level to allow short integrations and compilation of tens (or hundreds) of spectra. If longer than normal integrations are made, then some of this “dark” molecular gas might be observable. We showed that using longer integration times can result in detections of at least some of this “dark” molecular gas. We were able to show that two different techniques using the CO(1-0) transition, two techniques using the OH main line rotational transitions, and one technique using only the E(B-V) values from Schlegel, Finkbeiner and Davis (1998) all yielded significant masses of gas in the outermost regions of the translucent cloud MBM40. In addition, the seldom explored envelope region

of the cloud yielded more molecular mass than the gas in the core region. Whether this result applies in general to other clouds is discussed below. This unknown molecular gas in MBM40 could effect calculations on whether the cloud is bound or unbound and this extra mass could yield possible consequences such as star formation.

We began by trying to determine the amount of molecular gas contained in the high Galactic latitudes since translucent clouds were the focus of our study and most are found at high-latitudes. We used the SFD survey to find $E(B-V)$ values for the entire high latitude region defined to be $|b| \geq 30^\circ$. There were over 6.5×10^6 data points in each of the Galactic hemispheres and we binned these data points by $E(B-V)$ values into 0.05 mag increments. Using previous surveys, Hartmann, Magnani, and Thaddeus (1998) for the northern Galactic hemisphere and Magnani et al. (2000) for the southern Galactic hemisphere, we determined the ratio of CO detections to non-detections for each $E(B-V)$ bin, and found $N(\text{HI} + \text{H}_2)$ for each $E(B-V)$ bin. The mass of H_2 was estimated by using the calculated ratio in conjunction with the CO- H_2 conversion factor, X_{CO} . We wanted to calculate a lower limit of molecular mass so we chose $N(\text{H}_2)$ to only make up 10% of the total column density. This limitation yielded a total molecular mass of $2.0 \times 10^3 M_\odot$ for the northern Galactic hemisphere and $1.1 \times 10^4 M_\odot$ for the southern Galactic hemisphere, substantially higher values than what was detected in the Georgia/Harvard-Smithsonian CO surveys. These calculations showed that there could be substantially more molecular gas at the high Galactic latitudes than was previously thought. In addition to the CO(1-0) molecule, we also decided to use the 18 cm OH main line transitions as tracers of diffuse molecular gas. Deep integrations were made throughout MBM40 utilizing both CO and OH methods.

The CO methods consisted of using the 89 observations of the CO(1-0) transition in MBM40, then dividing these measurements into three sections depending on their positions in MBM40. We had 44 detections in the core region, 31 detections in the envelope region, and 14 detections in the outermost region of MBM40. The average measured $W(\text{CO})$ for each

region was then converted to $N(\text{H}_2)$ using the average X_{CO} for each region, $1.5 \pm 0.32 \times 10^{20}$, $1.9 \pm 0.58 \times 10^{20}$, and $2.0 \times 10^{20} \text{ cm}^{-2} [\text{K km s}^{-1}]^{-1}$, for the core, envelope, and outermost regions, respectively. This $N(\text{H}_2)$ value was then extrapolated over its entire respective region, thus allowing us to find the total mass of H_2 for each region (labeled CO-1 in Table 8.1). The second method used a function that related $E(\text{B-V})$ and observed $W(\text{CO})$. This function used the average $E(\text{B-V})$ for each region to find a corresponding $W(\text{CO})$ (section 6.3.3), which was then converted to the mass of molecular hydrogen as described in detail in Chapter 6. These results are labeled as CO-2 in Table 8.1.

The OH methods consisted of using the 35 observations of the OH main line rotational transition at 1667 MHz, then dividing these measurements into three sections depending on their positions in MBM40. There were 8 detections in the core region, 21 detections in the envelope region, and 3 in the outermost region of MBM40. $N(\text{OH})$ was calculated for each region then extrapolated over the extent of each region. After the total $N(\text{OH})$ was calculated for each region it was converted into an estimate of the mass of OH. Then using the OH/H_2 conversion factor of 6×10^{-8} from Wennerstrom (2007) the mass of H_2 was found. These results are labeled OH-1 in Table 8.1. The second OH method used a function that related $E(\text{B-V})$ and observed $W(\text{OH})$. This function used the average $E(\text{B-V})$ for each region to find a corresponding $W(\text{OH})$, which was then converted to the mass of molecular hydrogen in the same way described above, these results are labeled as OH-2 in Table 8.1.

The technique using only $E(\text{B-V})$ values uses the well known conversion factor from Bohlin Savage and Drake (1978) that converts $E(\text{B-V})$ into the total column density of hydrogen (see Equation 7.3). In order to use this equation we used the average $E(\text{B-V})$ values from the same three regions above, with a total of 810 data points over MBM40. There were 80 points in the core region, 247 in the envelope region, and 483 in the outermost region. Using the average $E(\text{B-V})$ value from each region we found the total hydrogen column density, then using the total area of each region we found the total H_2 mass of each region,

Summary of Molecular Mass in MBM40

Method	Molecular Hydrogen Mass (M_{\odot})		
	Core	Envelope	Outermost
CO-1	8.95 ± 1.92	8.78 ± 2.74	9.72 ± 1.42
CO-2	8.43 ± 3.67	7.69 ± 6.80	2.25 ± 1.42
OH-1	17.2	32.7	32.8
OH-2	17.7	31.9	17.2
E(B-V)	5.39 ± 0.13	11.6 ± 0.40	12.7 ± 0.79
Weighted Average	5.47	11.7	10.5

Table 8.1: Total calculated molecular hydrogen mass in MBM40 for all five techniques used through this thesis. The OH methods mass shown is from the weighted averages of each region based on estimates of T_{ex} , which are 10, 20 and 40K.

these are labeled as E(B-V) in Table 8.1. The five techniques yielded weighted averages for the mass contained in the core region of $5.47 M_{\odot}$, the envelope region of $11.7 M_{\odot}$, and the outermost region of $10.5 M_{\odot}$. This weighted average takes into account the errors in each technique and clearly shows that the envelope contains more than twice the mass of the core and the outermost region contains almost twice as much mass as the core. This additional mass located away from the core regions increases the total mass of the cloud and could yield previously unknown information about MBM40 and possibly other translucent clouds

Future work in this field would ideally involve larger, more detailed surveys similar to the Georgia-Harvard CO surveys, but a factor of at least two deeper in sensitivity. Unfortunately, this would require a factor of four more integration time. Since the Georgia-Harvard high-latitude CO surveys took over two years to complete, this is currently not a feasible plan. More plausible future endeavors that could be done with a reasonable amount of telescope time involve deep observations of the envelope and outer regions of other translucent molecular clouds. Ideal candidates include MBM16 and MBM3, for which much observational data of the envelope regions already exists (Magnani et al. 2011, in preparation).

These clouds could be used to get even more accurate X_{CO} values for each region, and a more accurate conversion factor between OH and H_2 following our work in Chapter 7. The sharpening of the empirical fraction of molecular gas contained in low-extinction regions would allow for a more precise knowledge about the outer regions of molecular clouds, and the clouds as a whole. Better knowledge about the non core regions of clouds could yield information that effects whether the cloud is unbound or bound. This new knowlege could show that previously known unbound clouds may actually be bound clouds, and if these clouds are bound, they could be sites of future star formation. Broadening our knowledge about these difficult to detect regions in translucent molecular clouds would allow us to better estimate the contribution to the mysterious dark molecular gas whose role in the ISM is poorly constrained.

Bibliography

- J. Bennett, M. Donahue, N. Schneider, and M. Voit. *The Cosmic Perspective Sixth ed.* Pearson Addison-Wesley, 2010.
- L. Blitz, M. Fich, and A. A. Stark. Catalog of CO Radial Velocities Toward Galactic HII Regions. *The Astrophysical Journal Supplement Series*, 49:183–206, 1982.
- L. Blitz, L. Magnani, and L. Mundy. High Latitude Molecular Clouds. *The Astrophysical Journal*, 282:L9–L12, 1984.
- H. Bloemen. Gamma-Ray and Far-Infrared Constraints on the $N(H_2)/W(CO)$ Conversion Factor of Molecular Clouds. In *Molecular Clouds*, New York, NY, 1991. Cambridge University Press. ISBN 0-521-39543-7.
- J. B. G. M. Bloemen, E. R. Deul, and P. Thaddeus. Decomposition of the FIR Milky Way Observed by IRAS. *Astronomy & Astrophysics*, 233:437–455, 1990.
- R.C. Bohlin, B.D. Savage, and J.F. Drake. A Survey of Interstellar HI From La Absorption Measurements. II. *The Astrophysical Journal*, 224:132–142, 1978.
- B. W. Carroll and D. A. Ostlie. *An Introduction to Modern Astrophysics*. Addison-Wesley Publishing Company, Inc., 1996.
- G. R. Carruthers. Rocket Observation of Interstellar Molecular Hydrogen. *The Astrophysical Journal*, 161:L81–L85, 1970.

- R. J. Chastain. *A Study of Three Molecular Structures at High Galactic Latitude*. PhD thesis, 2005, The University of Georgia.
- R. J. Chastain, D. L. Cotten, and L. Magnani. High-Resolution CH observations of Two Translucent Molecular Clouds. *The Astrophysical Journal*, 139:267–278, 2010.
- M. N. Cleary, C. G. T. Haslam, and C. Heiles. A Synoptic View of the Galaxy in HI. *Astronomy & Astrophysics Supplement Series*, 36:95–127, 1979.
- T. M. Dame, D. Hartmann, and P. Thaddeus. The Milky Way in Molecular Clouds: A New Complete CO Survey. *The Astrophysical Journal*, 547:792–813, 2001.
- J. L. Destombes, C. Marliere, A. Baudry, and J. Brillet. The Exact Hyperfine Structure and Einstein A-Coefficients of OH: Consequences in Simple Astrophysical Models. *Astronomy & Astrophysics*, 60:55–60, 1977.
- H. W. deVries, A. Heithausen, and P. Thaddeus. Molecular and Atomic Clouds Associated with Infrared Cirrus in URSA Major. . *The Astrophysical Journal*, 434:162–183, 1984.
- B. T. Draine. *Physics of the Interstellar and Intergalactic Medium*. Princeton University Press, 2011.
- B. G. Elmegreen. Cloud Formation and Destruction. In *Interstellar Processes*, P.O. Box 17, 3300 AA Dordrecht, Holland, 1987. D. Reidel Publishing Company. ISBN 90-277-2485-7.
- B. G. Elmegreen. The H to H₂ Transition in Galaxies: Totally Molecular Galaxies. *The Astrophysical Journal*, 411:170–177, 1993a.
- B. G. Elmegreen. Star Formation at Compressed Interfaces in Turbulent Self-Gravitating Clouds. *The Astrophysical Journal*, 419:L29–L32, 1993b.

- P. Friberg and Å. Hjalmarsen. Molecular Clouds in the Milky Way. In *Molecular Astrophysics A Volume Honouring Alexander Dalgarno*, New York, NY, 1990. Cambridge University Press. ISBN 0-521-36331-4.
- B. Y. Gir, B. Blitz, and L. Magnani. The Association of High-Latitude Molecular Clouds with HI Gas. *The Astrophysical Journal*, 399:551–562, 1994.
- P. F. Goldsmith. Molecular Clouds: An Overview. In *Interstellar Processes*, P.O. Box 17, 3300 AA Dordrecht, Holland, 1987. D. Reidel Publishing Company. ISBN 90-277-2485-7.
- P. M. Gondhalekar and R. Wilson. The Interstellar Radiation Field Between 912 Å and 2740 Å. *Astronomy & Astrophysics*, 38:329–333, 1975.
- I. A. Grenier, J. M. Casandjian, and R. Terrier. Unveiling Extensive Clouds of Dark Gas in the Solar Neighborhood. *Science*, 307:1292–1295, 2005.
- J. Guibert, M. Elitzur, and Nguyen-Q-Rieu. OH excitation in Interstellar Clouds. *Astronomy & Astrophysics*, 66:395–405, 1978.
- D. Hartmann, L. Magnani, and P. Thaddeus. A Survey of High-Latitude Molecular Gas in the Northern Galactic Hemisphere. *The Astrophysical Journal*, 492:205–212, 1998.
- I. Hawkins and M. Jura. The $^{12}\text{C}/^{13}\text{C}$ Isotope Ratio of the Interstellar Medium in the Neighborhood of the Sun. *The Astrophysical Journal*, 317:926–950, 1987.
- C.E. Heiles. The Interstellar Magnetic Field. *Annual Review Astronomy & Astrophysics*, 14: 1–22, 1976.
- J. G. Ingalls, W. T. Reach, and T. M. Bania. Photoelectric Heating and [CII] Cooling of High Galactic Latitude Translucent Clouds. *The Astrophysical Journal*, 579:289–303, 2002.

- M. Jura. The Milky Way as a Galaxy. In *Interstellar Processes*, P.O. Box 17, 3300 AA Dordrecht, Holland, 1987. D. Reidel Publishing Company. ISBN 90-277-2485-7.
- G. R. Knapp and M. Morris. Mass Loss From Evolved Stars. III. Mass Loss Rates for Fifty Stars from CO J = 1-0 Observations. *The Astrophysical Journal*, 292:640–669, 1985.
- M. L. Kutner and B. L. Ulich. Recommendations for Calibration of Millimeter-Wavelength Spectral Line Data. *The Astrophysical Journal*, 250:341–348, 1981.
- M. L. Kutner, K. D. Tucker, G. Chin, and P. Thaddeus. The Molecular Complexes in Orion. *The Astrophysical Journal*, 215:521–528, 1977.
- J. Lequeux. *The Interstellar Medium*. Springer, 2005.
- H. Liszt and R. Lucas. Comparative Chemistry of Diffuse Clouds. IV: CH. *Astronomy & Astrophysics*, 391:693–704, 2002.
- H. S. Liszt, J. Pety, and R. Lucas. The CO Luminosity and CO-H₂ Conversion Factor of Diffuse ISM: Does CO Emission Trace Dense Molecular Gas? *Astronomy & Astrophysics*, 518:A45–A55, 2010.
- R.J. Maddelena. *The Performance of the GBT A Guide for Planning Observations*, 2009.
- L. Magnani and J. Onello. A New Method for Determining the CO to H₂ Conversion Factor for Translucent Clouds. *The Astrophysical Journal*, 443:169–180, 1995.
- L. Magnani and L. Siskind. Hydroxyl Emission in Translucent Molecular Clouds. *The Astrophysical Journal*, 359:355–362, 1990.
- L. Magnani, L. Blitz, and L. Mundy. Molecular Gas at High Galactic Latitudes. *The Astrophysical Journal*, 295:402–421, 1985.

- L. Magnani, E. A. Lada, and L. Blitz. High-Latitude Molecular Clouds: Completeness of the Local Sample and Implications from Molecular Surveys. *The Astrophysical Journal*, 301: 395–397, 1986.
- L. Magnani, E. A. Lada, G. Sandell, and L. Blitz. CH Observations of Diffuse Molecular Clouds. *The Astrophysical Journal*, 339:244–257, 1989.
- L. Magnani, J. P. Caillault, T. Herty, J. Stauffer, J. H. M. M. Schmitt, and R. Neuhaüuser. A Search for Star Formation in the Translucent Cloud MBM40. *The Astrophysical Journal*, 465:825–839, 1996a.
- L. Magnani, D. Hartmann, and B. G. Speck. A Catalog of Molecular Gas at High Galactic Latitudes. *The Astrophysical Journal Supplement Series*, 106:447–461, 1996b.
- L. Magnani, J. S. Onello, N. G. Adams, D. Hartmann, and P. Thaddeus. The Variation of the CO to H₂ Conversion Factor in Two Translucent Clouds. *The Astrophysical Journal*, 504:290–299, 1998.
- L. Magnani, D. Hartmann, S. L. Holcomb, L. E. Smith, and P. Thaddeus. High-Latitude Molecular Gas in the Southern Galactic Hemisphere. *The Astrophysical Journal*, 535: 167–175, 2000.
- L. Magnani, R. Chastain, H. C. Kim, D. Hartmann, A. Truong, and P. Thaddeus. CH, CO, and E(B – V) as Molecular Gas Tracers in a Translucent Clouds. *The Astrophysical Journal*, 586:1111–1119, 2003.
- P. Maloney. Are Molecular Clouds in Virial Equilibrium? *The Astrophysical Journal*, 348: L9–L12, 1990.
- J. P. Mathis, P. G. Metzger, and N. Panagia. Interstellar Radiation Field and Dust Tem-

- peratures in the Diffuse Interstellar Matter and in Giant Molecular Clouds. *Astronomy & Astrophysics*, 128:212–229, 1983.
- K. Mattila. Radio Observations of CH in Three Dark Nebulae and the Correlation of CH with Optical Extinction and Molecular Hydrogen. *Astronomy & Astrophysics*, 160:157–170, 1986.
- C. F. McKee and E. G. Zweibel. On the Virial Theorem for Turbulent Molecular Clouds. *The Astrophysical Journal*, 399:551–562, 1992.
- T. J. Millar. Chemical Modelling of Quiescent Dense Interstellar Clouds. In *Molecular Astrophysics A Volume Honouring Alexander Dalgarno*, New York, NY, 1990. Cambridge University Press. ISBN 0-521-36331-4.
- P. C. Myers. Observations of Molecular Cloud Structure and Internal Motions. In *Interstellar Processes*, P.O. Box 17, 3300 AA Dordrecht, Holland, 1987. D. Reidel Publishing Company. ISBN 90-277-2485-7.
- P. C. Myers and A. A. Goodman. Evidence for Magnetic and Virial Equilibrium in Molecular Clouds. *The Astrophysical Journal*, 326:L27–L30, 1988.
- E. Nercessian, J. J. Benayoun, and Y. P. Viala. Steady-Star Chemical Model of the Molecular Cloud Towards the Star HD 29647. *Astronomy & Astrophysics*, 195:245–256, 1988.
- B. E. Penprase. Photometric and Spectroscopic Analysis of High Latitude Molecular Clouds. II. High Resolution Spectroscopic Observations of Na I, Ca II, Ca I, CH and CH⁺¹. *The Astrophysical Journal Supplement Series*, 88:433–475, 1993.
- K. S. Polk, G. R. Knapp, A. A. Stark, and R. W. Wilson. Molecules in Galaxies. VI. Diffuse and Dense Cloud Contributions to the Large-Scale CO Emission of the Galaxy. *The Astrophysical Journal*, 332:432–438, 1988.

- E. E. Salpeter. Planetary Nebulae, Supernova Remnants, and the Interstellar Medium. *The Astrophysical Journal*, 206:673–678, 1976.
- D. B. Sanders, P. M. Solomon, and N. Z. Scoville. Giant Molecular Clouds in the Galaxy I - The Axisymmetric Distribution of H₂. *The Astrophysical Journal*, 276:182–203, 1984.
- D. J. Schlegel, D. P. Finkbeiner, and M. Davis. Maps of Dust Infrared Emission For Use in Estimation of Redding and Cosmic Microwave Background Radiation Foregrounds. *The Astrophysical Journal*, 500:525–553, 1998.
- N. Z. Scoville, M. S. Yun, D. B. Sanders, D. P. Clemens, and W. H. Waller. Molecular Clouds and Cloud Cores in the Inner Galaxy. *The Astrophysical Journal Supplement Series*, 63: 821–915, 1987.
- S. Sharpless. A catalogue of HII regions. *The Astrophysical Journal Supplement Series*, 4: 257–279, 1959.
- S. N. Shore. *Astrophysical Hydrodynamics: An Introduction*. Wiley, 2007.
- S. N. Shore, L. Magnani, T. N. LaRosa, and M. N. McCarthy. Mechanisms for the Origin of Turbulence in Non-Star-forming Clouds: The Translucent Cloud MBM40. *The Astrophysical Journal*, pages 413–425, 2003.
- J. M. Shull and S. Beckwith. Interstellar Molecular Hydrogen. *Annual Review Astronomy & Astrophysics*, pages 163–190, 1982.
- P. D. Singh and A. A. de Almeida. The Hydroxyl Ion in Interstellar Clouds. *Astronomy & Astrophysics*, 84:177–180, 1980.
- P. M. Solomon, A. R. Rivolo, J. Barrett, and A. Yahil. Mass Luminosity and Line Width Relations of Galactic Molecular Clouds. *The Astrophysical Journal*, 319:730–741, 1987.

- P. Sonnentrucker, D. E. Welty, J. A. Thornburn, and D. G. York. Abundances and Behavior of ^{12}CO , ^{13}CO , and C_2 in Translucent Sight Lines. *The Astrophysical Journal Supplement Series*, 168:58–99, 2007.
- L. Spitzer. *Physical Processes in the Interstellar Medium*. John Wiley & Sons, Inc., 1978.
- T. A. Spoolstra. Galactic Loops as Supernova Remnants in the Local Galactic Magnetic Field. *Astronomy & Astrophysics*, 24:149–155, 1973.
- A. W. Strong, J. B. G. M. Bloemen, T. M. Dame, I. A. Grenier, W. Hermsen, W. Hermsen, F. Lebrun, L. A. Nyman, A. M. T. Pollock, and P. Thaddeus. The Radial Distribution of Galactic Gamma Rays IV - The Whole Galaxy. *Astronomical Society of the Pacific.*, 12: 207–226, 1990.
- J. A. Tauber, P. F. Goldsmith, and R.L. Dickman. The Smoothness of CO Line Profiles in Orion - Implications for Clumpiness. *The Astrophysical Journal*, 375:635–641, 1991.
- E.F. van Dishoeck. The Chemistry of the Diffuse Interstellar Gas. *Astronomical Society of the Pacific.*, 12:207–226, 1990.
- Ewine F. Van Dishoeck and John H. Black. Comprehensive Models of Diffuse Interstellar Clouds: Physical Conditions and Molecular Abundances. *The Astrophysical Journal Supplement Series*, 62:109–145, 1986.
- Ewine F. Van Dishoeck and John H. Black. The Photodissociation and Chemistry of Interstellar CO. *The Astrophysical Journal*, 334:771–802, 1988.
- Y. P. Viala. Chemical Equilibrium from Diffuse to Dense Interstellar Clouds. I. Galactic Molecular Clouds. *Astronomy & Astrophysics Supplement Series*, 64:391–437, 1986.
- J. L. Weiland, L. Blitz, E. Dwek, M. G. Hauser, L. Magnani, and L. J. Rickard. Infrared Cirrus and High-Latitude Molecular Clouds. *The Astrophysical Journal*, 301, 1986.

- S. Weinreb, A. H. Barrett, D. L. Meeks, and J. C. Henry. Radio Observations of OH in the Interstellar Medium. *Nature.*, 200:829–831, 1963.
- D. E. Welty, L. M. Hobbs, L. Blitz, and B. E. Penprase. On the Nearest Molecular Clouds. III. MBM 40, 53, 54, and 55. *The Astrophysical Journal*, 346:232–242, 1989.
- E. Wennerstrom. A Survey of Hydroxyl in Three Translucent Molecular Clouds. Master's thesis, 2007, The University of Georgia.
- R. W. Wilson, K. B. Jefferts, and A. A. Penzias. Carbon Monoxide in the Orion Nebula. *The Astrophysical Journal*, 161:L43–L44, 1970.
- A.W. Wolfendale. The Mass of Molecular Gas in the Galaxy. In *Molecular Clouds*, New York, NY, 1991. Cambridge University Press. ISBN 0-521-39543-7.
- J. Wouterloot. *The Large-Scale Structure of Molecular Clouds*. PhD thesis, The University of Leiden: Leiden., 1981.